FRACTURE MECHANICS ANALYSIS OF SHAPE MEMORY ALLOYS USING FINITE ELEMENTS

by

Miray Şimşek

B.S., Mechanical Engineering, Boğaziçi University, 2006

Submitted to the Institute for Graduate Studies in
Science and Engineering in partial fulfillment of
the requirements for the degree of
Master of Science

Graduate Program in Mechanical Engineering
Boğaziçi University

2009

FRACTURE MECHANICS ANALYSIS OF SHAPE MEMORY ALLOYS USING FINITE ELEMENTS

APPROVED BY:

Prof. Günay Anlaş .....
(Thesis Supervisor)

Assist. Prof. C. Can Aydıner .....

Assist. Prof. Hilmi Luş .....

DATE OF APPROVAL: 10.06.2009

To my mom and dad

ACKNOWLEDGEMENTS

I would like to express my sincere gratitude to my thesis supervisor, Professor Günay Anlaş for his guidance, advice, support and encouragement during this study. It has been an honor and a pleasure to work with him. I would like to thank Assist. Prof. C. Can Aydıner for his helpful comments and encouraging discussions and Assist. Prof. Hilmi Luş for his interest and review of the thesis.

I would like to thank my friends Nadir and Selçuk for their assistance and helpful discussions on the subject. I wish to thank my fellow research assistants Gülşad, Erhan, Yalın and Özgu for their emotional and academic supports during my graduate study. I also want to thank my friends for their endless motivation with whom I shared my dancing hobby, which was my getaway from the intense study. I am also fortunate to have the love and infinite support of my sweetheart, Güneş. He has always been my relief during the toughest times, thanks for the endless enthusiasm.

Finally, this study would not have been possible without the support of my family, especially my mom and dad who have always encouraged me to follow my dreams and happiness. I will be eternally grateful to them for all the sacrifices they made on my behalf.

ABSTRACT

FRACTURE MECHANICS ANALYSIS OF SHAPE MEMORY ALLOYS USING FINITE ELEMENTS

The objective of this work is to study phase transformation and its effects on macroscopic fracture behavior of superelastic shape memory alloy, Nitinol, using finite elements. For this purpose, A 2-D edge-cracked homogenous plate is modeled using ABAQUS, stress intensity factors under Mode-I loading are calculated and compared to results available in literature to verify the model and the technique used. Same analyses are performed for a 2-D edge-cracked SMA plate under plane stress conditions and UMAT/Nitinol subroutine is used to define material properties. Phase transformation zones around crack tip are investigated for different applied loads and for different crack lengths. J-integrals, energy release rates and stress intensity factors are calculated. To see the effects of material properties, a parametric study is carried out and four different cases are presented. Stress intensity factors are also calculated for a center-cracked specimen and the results are compared to the only closed-form solution available in literature. The effect of volumetric strain on fracture toughness and change in fracture toughness as a result of phase transformation are discussed in detail.

ÖZET

ŞEKİL HAFIZALI ALAŞIMLARIN KIRILMA MEKANİĞİNİN SONLU ELEMANLAR YÖNTEMİ İLE İNCELENMESİ

Bu çalışmanın amacı, süperelastik Şekil Hafızalı Alaşımlardan biri olan Nitinoldeki (NiTi) faz transformasyonunu ve bunun kırılma mekaniği açısından etkilerini sonlu elemanlar yöntemi ile incelemektir. Bu bağlamda öncelikle, 2 boyutlu kenar çatlaklı homojen plakalar ABAQUSte modellenmiştir. Oluşturulan modeli ve kullanılan tekniği doğrulamak amacı ile, Mod-I yükleme altında gerilim şiddet çarpanları hesaplanmış ve literatürdeki sonuçlarla karşılaştırılmıştır. Aynı analizler, düzlem gerilme altındaki 2 boyutlu kenar çatlaklı Nitinol plakalar için de gerçekleştirilmiştir. Malzeme özellikleri ABAQUS içerisinde yerleşik olarak bulunan UMAT/Nitinol isimli bir alt program ile tanımlanmıştır. Çatlak etrafındaki faz transformasyonu farklı çatlak uzunlukları için çeşitli yüklemeler altında incelenmiştir. J-integrali değerleri, enerji salınım oranları ve gerilim şiddet çarpanları hesaplanmıştır. Malzeme özelliklerinin etkisini görmek amacıyla analizler dört farklı koşulda yinelenerek parametrik bir çalışma gerçekleştirilmiştir. Ek olarak merkez çatlaklı nitinol plakalarda benzer analizler yinelenmiş, gerilim şiddet çarpanları hesaplanmıştır. Elde edilen sonuçlar, literatürdeki tek kapalı-form sonuçla karşılaştırılmıştır. Son olarak faz transformasyonunun ve bunun sonucunda çatlak ucunda olusan hacimsel gerinimin malzemenin kırılma tokluğu üzerine olan etkisi tartışılmıştır.

TABLE OF CONTENTS

ACKNOWLEDGEMENTS iv
ABSTRACT v
ÖZET vi
LIST OF FIGURES ix
LIST OF TABLES xii
LIST OF SYMBOLS/ABBREVIATIONS xiv
1. INTRODUCTION 1
1.1. Shape Memory Alloys (SMAs) 1
1.1.1. Phase Transformation 2
1.1.2. Shape Memory Effect 4
1.1.3. Superelasticity 6
1.1.4. Nitinol 9
1.1.5. Applications of Shape Memory Alloys 9
1.2. Constitutive Models 11
1.2.1. Auricchio-Taylor-Lubliner Method 13
1.2.1.1. Conversion of austenite into single-variant martensite: A to S 14
1.2.1.2. Conversion of single-variant martensite into austenite: S to A 16
1.2.1.3. Single-variant martensite reorientation process: S to S 18
1.3. Previous Studies on Fracture of SMAs 18
1.4. Objective of This Study 23
2. EDGE CRACKED HOMOGENEOUS PLATE 25
2.1. Modeling & Material Properties 25
2.2. Fracture Properties 27
3. EDGE CRACKED SMA PLATE 33
3.1. Modeling & Material Properties 33
3.2. Effect of a Crack on Phase Transformation 37
3.3. Fracture Properties 45

3.3.1. J-Integral 45
3.3.2. Energy Release Rate & Stress Intensity Factor 49
3.3.3. Discussion on Energy Stored 52
3.4. Parametric Study of the Effect of Material Properties 56
3.5. A Closed Form Solution of Mode-I Stress Intensity Factor in Nitinol Shape Memory Alloy 63
4. FRACTURE TOUGHNESS OF SMAs 76
5. CONCLUSIONS 84
APPENDIX A: FUNDAMENTAL CONCEPTS OF FRACTURE MECHANICS 87
A.1. Stress at the crack tip 87
A.2. Griffith Criterion and Energy Release Rate 89
A.3. The J Contour Integral 92
REFERENCES 94

LIST OF FIGURES

Figure 1.1. Body-centered cubic structure for austenite and monoclinic structure for martensite 2

Figure 1.2. Phase transformation temperatures 3

Figure 1.3. Stress-temperature phase diagram for an SMA 4

Figure 1.4. Stress-temperature diagram and related phase changes for shape memory effect 5

Figure 1.5. Stress-strain-temperature diagram exhibiting shape memory effect for a typical NiTi SMA 6

Figure 1.6. Stress-temperature diagram for superelastic loading 7

Figure 1.7. Superelastic stress-strain diagram 8

Figure 1.8. Deformation mechanism and lattice structure of SMAs 8

Figure 1.9. Conversion of austenite into single-variant martensite (A→ S) in 1-D model 15

Figure 1.10. Conversion of single-variant martensite into austenite (S→ A) in 1-D model 17

Figure 2.1. Geometry of the 2-D edge-cracked specimen 26

Figure 2.2. Mesh geometry of 2-D edge-cracked specimen model 26

Figure 2.3. Mesh configuration of the crack tip 27

Figure 2.4. Representation of elements used in contour integral calculation . . 28

Figure 2.5. J-integral values for different a/W ratios 29

Figure 3.1. Uniaxial behavior of superelastic nitinol 34

Figure 3.2. The uniaxial tensile stress-strain relationship of nitinol used in the subroutine 36

Figure 3.3. Phase transformation around the crack tip of a 2-D edge-cracked plate subjected to tensile loading 38

Figure 3.4. Phase transformation regions around the crack tip 39

Figure 3.5. Phase transformation Zones for 2-D edge-cracked Nitinol specimen, $a/W = 0.3$ for different applied loads 41

Figure 3.6. Phase Transformation zones at applied load 8 kN for different a/W ratios 43

Figure 3.7. Martensite fractions along a path away from the crack tip 44

Figure 3.8. Elements used in the corresponding contours 47

Figure 3.9. J-integral values with different a/W ratios and load = 8 kN 48

Figure 3.10. The non-dimensionalized SIFs obtained from J_∞ and SIF's calculated from the energy release rate, G 51

Figure 3.11. Energy stored calculated by ABAQUS 53

Figure 3.12. Comparison of energy values 54

Figure 3.13. Energy stored calculated for a single element 55

Figure 3.14. Energy stored calculated for loading-unloading analysis 56

Figure 3.15. Schematic representation of stress-strain curves for materials used to study the effect of material parameters 57

Figure 3.16. Phase transformation zones around the crack tip for four cases . . 58

Figure 3.17. J-Integral values in all cases for different crack lengths 61

Figure 3.18. K-dominant and inelastic regions around the crack tip 64

Figure 3.19. Illustration of elastic-plastic stress redistribution according to Irwin's second order estimate 65

Figure 3.20. Illustration of regions in front of the crack tip in SMAs 68

Figure 3.21. Stress redistribution around the crack tip as a result of phase transformation 69

Figure 3.22. The uniaxial tensile stress-strain relationship of the material model 74

Figure A.1. Modes of fracture 87

Figure A.2. Illustration of stress field around the crack tip 88

Figure A.3. Arbitrary contour around the crack tip 92

LIST OF TABLES

Table 2.1. J-integral values obtained from ABAQUS for different a/W ratios 29

Table 2.2. J-integral values obtained from ABAQUS and the strain energy release rates, G 30

Table 2.3. Stress intensity factors calculated with different methods for different a/W ratios for homogenous plate 31

Table 2.4. Stress intensity factor calculation for homogenous materials with different elastic modulus 32

Table 3.1. Input to Umat/Nitinol 34

Table 3.2. J-integrals for edge-cracked Nitinol for different a/W ratios and load = 8 kN 46

Table 3.3. The calculated energy release rates, G, and the stress intensity factors, K_I, computed from the equation $G = \frac{K_I^2}{E_{Tip}}$ 50

Table 3.4. K_I obtained from constant J_∞ and the energy release rate 50

Table 3.5. Non-dimensionalized stress intensity factors, K_I and the corresponding percent errors 51

Table 3.6. J-integral values for different crack lengths in all cases 59

Table 3.7. J-integral values, J_∞, calculated energy release rates, G, and the stress intensity factors, K_I for each cases 62

Table 3.8. Closed form solution for K_I for a $Ni_{50}Ti_{50}$ plate 72

Table 3.9. K_I for $Ni_{50}Ti_{50}$ plate using FE 75

Table 3.10. K_I for $Ni_{50}Ti_{50}$ plate; closed-form solution vs FE solution 75

Table 4.1. Comparison of energy release rates 79

Table 4.2. Comparison of SIFs 79

Table 4.3. Percent increase & decrease in $\frac{\Delta U}{\Delta A}$ and K_I 80

Table 4.4. Comparison of energy release rates in fixed-grip conditions 80

Table 4.5. Comparison of SIFs in fixed-grip conditions 81

Table 4.6. Percent increase & decrease in $\frac{\Delta U}{\Delta A}$ and K_I in fixed-grip conditions 81

Table 4.7. Effect of volumetric transformation strain 82

Table 4.8. Effect of larger volumetric transformation strains 83

Table A.1. Stress and displacement fields for three fracture modes 89

LIST OF SYMBOLS/ABBREVIATIONS

a	Crack length
a_{eff}	Effective crack length
A	Area
A_f	Austenite finish temperature
A_s	Austenite start temperature
A_s^σ	Austenite finish temperature at specified stress value
A_f^σ	Austenite start temperature at specified stress value
C	Stress-temperature coefficient
E	Young's modulus
E'	Effective Young's modulus
f	Finish
F	Drucker-Prager type loading unction
G	Energy Release rate
H	Plate height
I	Identity matrix
J	J-Integral
K_I	Mode-I stress intensity factor
K_{II}	Mode-II stress intensity factor
K_{III}	Mode-III stress intensity factor
K_{tr}	Stress intensity contribution due phase transformation
M_d	Martensite desist temperature
M_f	Martensite finish temperature
M_s	Martensite start temperature
M_f^σ	Martensite finish temperature at specified stress value
M_s^σ	Martensite start temperature at specified stress value
p	Pressure
P	Applied load
R	Transformation function
r_p	Length of plastic zone

r_m	Length of fully martensitic zone
r_{tr}	Length of transformation zone
s	Start
$\mathbf{t}$	Deviatoric part of the stress
t	Thickness
T	Temperature
T_0	Reference temperature
U	Elastic strain energy
W	Plate width

α	Pressure sensitivity
β	Material parameter measuring the speed of transformation
ε^L	Transformation strain
ε_V^{tr}	Volumetric transformation strain
ν	Poisson's ratio
ξ_A	Austenite fraction
ξ_M	Martensite fraction
ξ_S	Single variant martensite fraction
σ^{A_f}	Austenite finish stress at constant temperature
σ^{A_s}	Austenite start stress at constant temperature
σ^{M_f}	Martensite finish stress at constant temperature
σ^{M_s}	Martensite start stress at constant temperature
σ_s	Starting stress of detwinning
σ_f	Finishing stress of detwinning
σ_Y	Yield Stress
σ_L^S	Start of transformation loading
σ_L^E	End of transformation loading
σ_U^S	Start of transformation unloading
σ_U^E	End of transformation unloading
σ_0	Applied remote stress

σ_y	Normal stress along y-direction
τ	Kirchhoff stress

2D	2 dimensional
3D	3 dimensional
A	Austenite
AS	Conversion of austenite into single-variant martensite
BCC	Body centered cubic
CPS8R	Eight-node biquadratic plane stress quadrilateral
DIC	Digital image correlation
FE	Finite elements
ND	Non-dimensionalized
NiTi	Nickel-Titanium
NOL	Naval ordnance laboratory
PE	Pseudoelasticity
S	Single variant martensite
SA	Conversion of single-variant martensite into austenite
SE	Superelasticity
SIF	Stress intensity factor
SIM	Stress Induced Martensite
SME	Shape memory effect
SMA	Shape memory alloy
SS	Reorientation of the single-variant martensite
TWSME	Two-way shape memory effect

1. INTRODUCTION

1.1. Shape Memory Alloys (SMAs)

Shape Memory Alloys (SMAs) are smart materials and have interesting characteristics and properties. They are mainly known as materials that "remember" their original shape when their temperature is increased. This means that even when the material is deformed in a large amount, it can turn back to its original shape. In addition, under mechanical cyclic loading, SMAs can sustain large deformation by absorbing and dissipating considerable amount of mechanical energy.

In 1938 Greninger and Mooradian observed the "shape memory behavior" of some copper based alloys (i.e. Cu-Zn, Cu-Sn) [1]. After nearly 25 years, in 1962, William J. Buehler and co-workers discovered that a nickel-titanium alloy returns to its original shape as a result of a change in temperature [2]. They applied for the first patent in 1965 and named the compound "NITINOL" after "Nickel-Titanium (NiTi)" and the "Naval Ordnance Laboratory (NOL)" [3]. With studies on Nitinol, several other alloys with shape memory effect (SME) were discovered. However, only Ni-Ti and Cu-Zn-Al alloys are used commercially because they have the ability to recover from large amounts of strain, improved fatigue life and some other desirable properties such as corrosion resistance, biocompatibility etc.

SMAs can be categorized into certain groups according to their different responses to different stimuli. Shape memory effect (SME), Two-way shape memory effect (TWSME) and Superelasticity (SE) are some of the responses to stimuli such as temperature and stress. SME and SE have been studied for a long time. The main reason behind this behavior is the solid-to-solid diffusionless phase transformation. As a result of temperature or stress change, positions of particles within the crystal structure of the solid are rearranged and a phase change from *martensite* to *austenite* or *austenite* to *martensite* occurs.

Properties of SMAs have attracted attention and commercial applications have become widespread. They have been used in mechanical, electronic, automotive engineering and aerospace industry; there are medical, military, robotics and safety applications. Common commercial examples are eyeglass frames, mobile phone antennas, dental braces, actuators, smoke detectors and mostly, endovascular stents [4, 5, 6, 7, 8].

1.1.1. Phase Transformation

Phase transformation is a change of phase by an external effect such as temperature, pressure, magnetic field, etc. It is generally known as transitions between solid, liquid and gaseous states of matter. However, there is a different case which is known as solid-to-solid diffusionless phase transformation where transformation occurs between the two phases of SMA, austenite and martensite, by simple displacement of atoms without diffusion or breaking of bonds [9]. Austenite is a crystallographically more-ordered phase and is stable at high temperature and low stress whereas martensite is a crystallographically less-ordered phase, and is stable at low temperature and high stress. For example, in NiTi, austenite has body centered cubic, BCC structure, whereas martensite has monoclinic crystal structure.

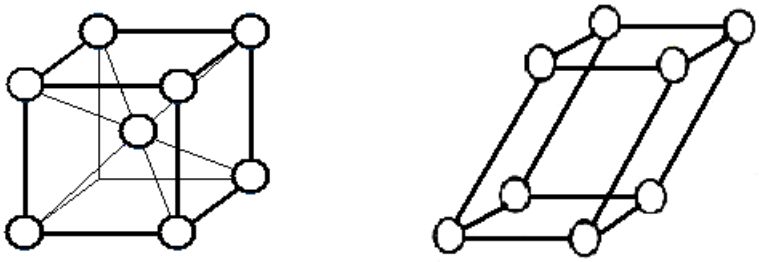

Figure 1.1. Body-centered cubic structure for austenite and monoclinic structure for martensite

Transformations between austenite (parent phase) and martensite (product phase) can be categorized into two groups: thermal-induced transformation and stress-induced transformation. Either temperature or stress change may trigger the transformation. In thermal-induced transformation, formerly deformed structure is subjected to tem-

perature change which results in phase transformation from martensite to austenite. In stress-induced transformation, the structure is subjected to a stress field at a specified constant temperature. As a result, a phase transformation occurs from austenite to martensite.

The transformation temperature,the temperature at which the SMA changes its crystallographic structure, may change according to its composition and the way it was processed. Under stress-free conditions for a specific SMA, there are four characteristic temperature values which denote the start and finish of the transformation process.

- M_s : Martensite Start Temperature
- M_f : Martensite Finish Temperature
- A_s : Austenite Start Temperature
- A_f : Austenite Finish Temperature

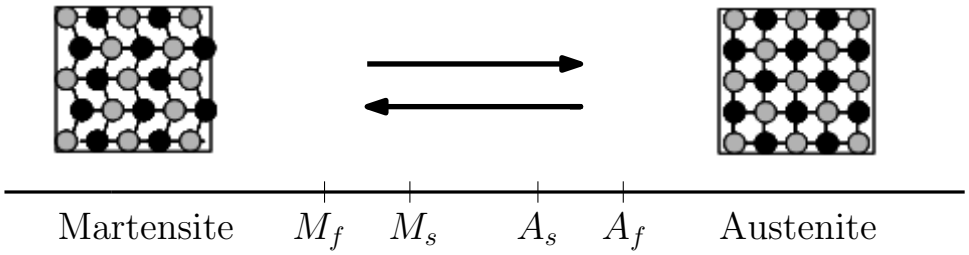

Figure 1.2. Phase transformation temperatures [10]

In the case of stress-free condition (thermal-induced transformation), transformation from austenite to martensite starts at M_s, and is completed when the material is fully martensite at M_f. Below M_f, martensite is stable, transformation cannot occur even by addition of stress. At A_s, reverse transformation (austenite to martensite) begins; and finally it is finished at A_f and the material is fully austenite. It should be noted that these temperatures are stress-dependent and change as a function of stress as shown in Figure 1.3. In the isothermal case above a specific temperature, when the material is subjected to mechanical loading, there is a transformation from austenite to martensite which is called stress induced martensitic transformation. However, this property is only observed over a specific temperature range, from near A_f up to temperature martensite desist temperature, M_d, above which stress-induced martensite

no longer appears. If applied stress increases, all of four transformation temperature values increase linearly (Figure 1.3).

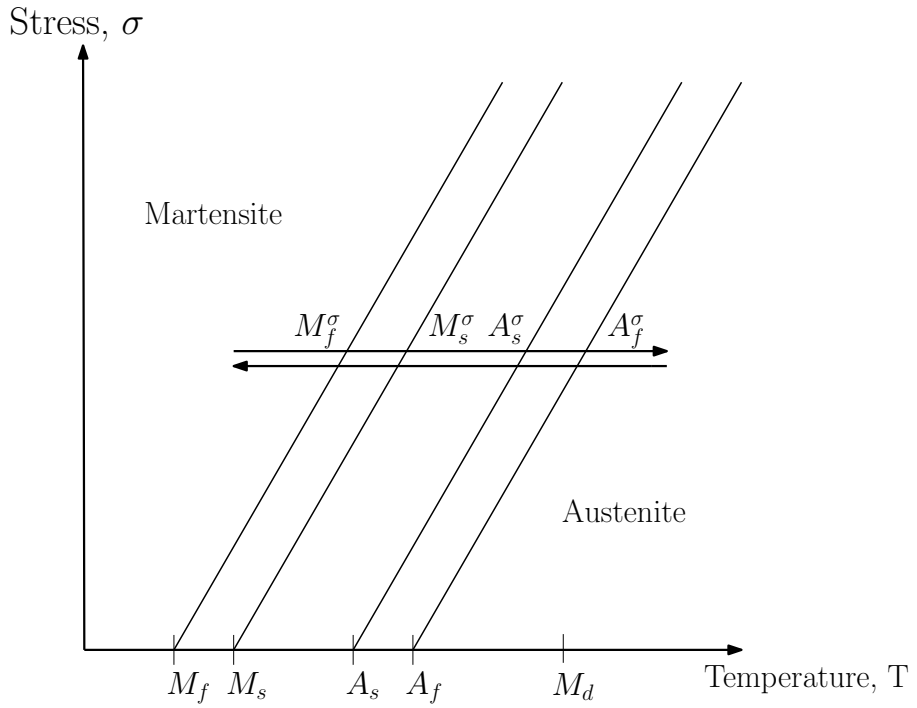

Figure 1.3. Stress-temperature phase diagram for an SMA, M_f^σ, M_s^σ, A_s^σ, A_f^σ are transformation temperatures a specific applied load

1.1.2. Shape Memory Effect

Shape Memory Effect is the ability of a deformed specimen to recover its previous shape upon heating. At high temperatures, an SMA specimen is in austenite phase and when it is cooled below M_s, it transforms into martensite and after M_f, martensite phase becomes stable. Each martensitic crystal that is formed has a different direction of orientation, called a variant. Martensite can exist in two forms: twinned martensite, which is formed by a combination of self-accommodated martensitic variants, and detwinned or reoriented martensite, in which a specific variant is dominant [8].

At low temperatures, if a material in the state of twinned martensite is mechanically loaded, certain number of variants are reoriented and the material becomes detwinned martensite. Material can be deformed at low stresses because interfaces between variants slip easily. Leading to macroscopic shape change; the deformation

remains even when the load is removed. If the material is heated above A_f, the material transforms back from detwinned martensite to austenite and as a result,it recovers its initial shape. If the material is cooled back to a temperature below M_f, twinned martensite forms again without any shape change. This phenomena is called Shape Memory Effect (SME) and is schematically summarized in Figure 1.4.

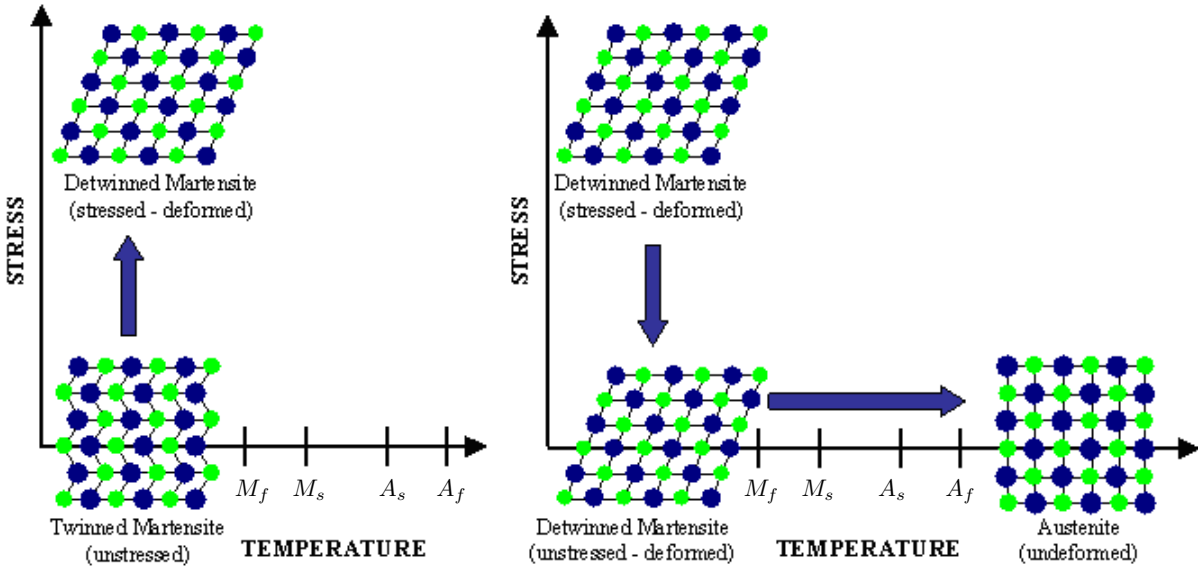

Figure 1.4. Stress-temperature diagram and related phase changes for shape memory effect [10]

In Figure 1.5, stress - strain - temperature relation of a NiTi specimen is plotted. At point A, material is in full austenite phase. When it is cooled to a temperature below M_f in stress-free state, forward transformation starts and the material becomes twinned martensite at point B. Then, it is loaded isothermally and when the applied stress exceeds the start stress level of σ_s, reorientation process initiates and the material becomes detwinned martensite. Reorientation continues until stress reaches σ_f and the material is unloaded from C to D; only elastic strain is recovered and detwinned martensite phase is sustained. Upon heating in the absence of stress, reverse transformation initiates at point E, and transformation is completed at temperature A_f at point F; all plastic strain coming from phase transformation is recovered and memorized shape is regained [8].

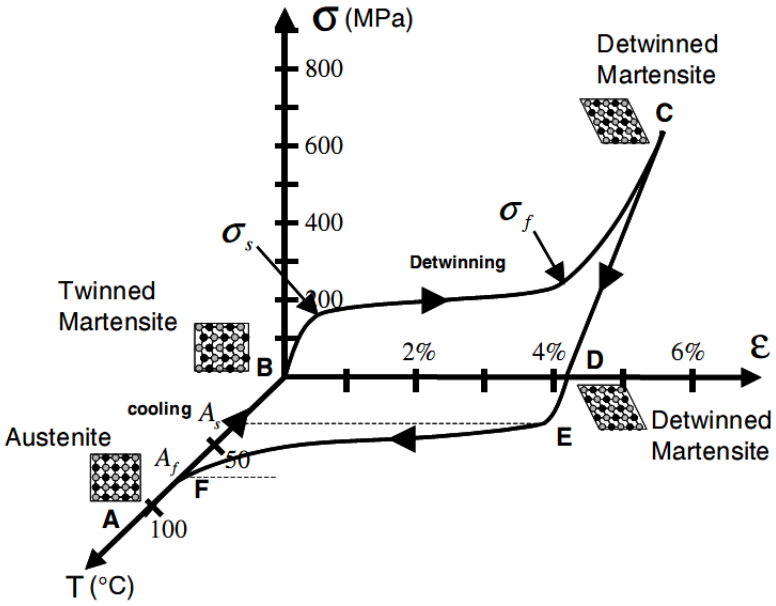

Figure 1.5. Stress-strain-temperature diagram exhibiting shape memory effect for a typical NiTi SMA [8]

1.1.3. Superelasticity

Another important and common property of shape memory alloys is the superelasticity (SE) which is also known as pseudoelasticty (PE). This property is observed in a specific temperature range. The material should be deformed above austenite finish temperature A_f , but below martensite desist temperature M_d which is the highest temperature at which martensite can no longer be stress-induced. In superelasticity, deformation occurs under constant temperature. Applied stress causes phase transformation from austenite to martensite and this is called stress-induced transformation. During transformation, austenite crystals transform into single variant martensite that are oriented parallel to loading direction. As a result, there occurs a high amount of macroscopic strain of about 8% - 11%, whereas most metals can only deform elastically to less than 1% strain. When stress is released, phase transformation occurs backwards, crystal structure returns to austenite again, strain is recovered because martensite is not stable at high temperatures and material returns to its original shape. Some experiments showed that amount of loading is important and it specifies percentage of recovered strain. If load is high enough, stress-induced martensite may be stabilized above martensite formation temperature [11].

In Figure 1.6, stress - temperature dependance of a superelastic SMA that is loaded at constant temperature T above A_f is shown. At σ^{M_s}, stress-induced martensite transformation starts; when the stress value reaches σ^{M_f}, material becomes martensite.

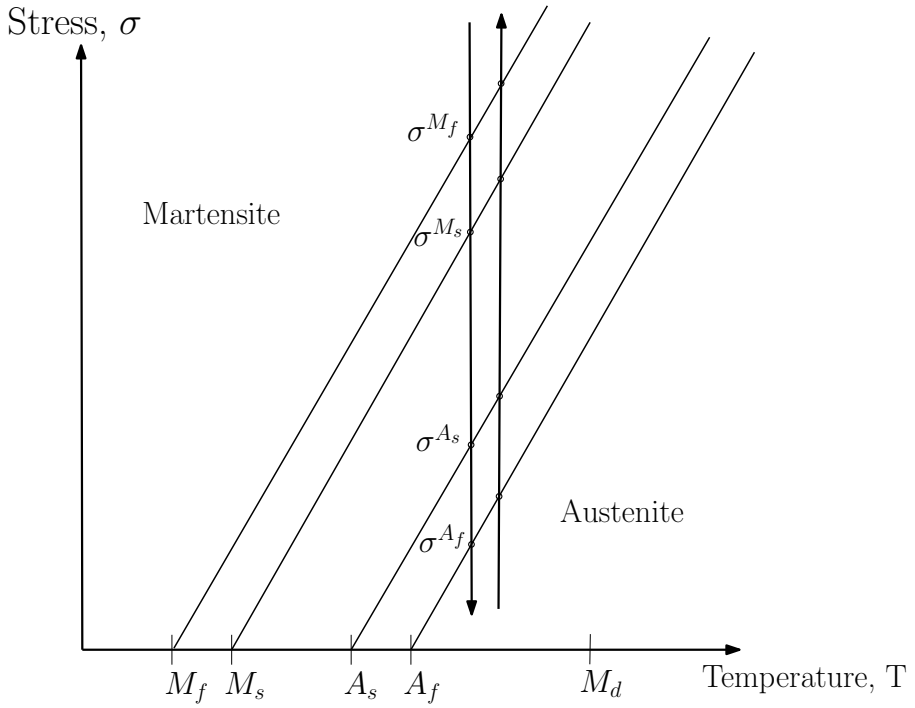

Figure 1.6. Stress-temperature diagram for superelastic loading

As shown in the superelastic stress - strain diagram, Figure 1.7, a large inelastic transformation strain, ε^T, results during transformation. An SMA at constant temperature between A_f and M_d first deforms elastically into austenite until the stress reaches σ^{Ms}. After σ^{Ms}, phase transformation onsets and transformation from martensite to austenite occurs at nearly constant stress value. Once σ^{Mf} is reached, transformation is completed and the new phase is called stress-induced martensite. In general σ^{Ms} and σ^{Mf} increase with temperature. If the loading is gradually increased, martensite starts to deform elastically. When the loading is released; first, elastic deformation of martensite is recovered and afterwards the reverse phase transformation begins. At the end of unloading, strain due to phase transformation is totally recovered. Yet there exist a hysteresis in the loading - unloading curve as shown in Figure 1.6. The unloading curve does not follow the loading curve and there exist some energy dissipation in transformation cycle.

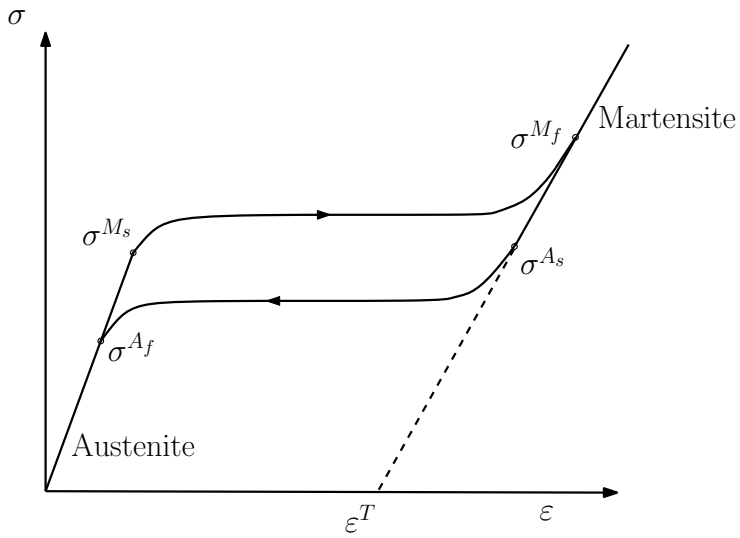

Figure 1.7. Superelastic stress-strain diagram

In Figure 1.8, deformation mechanisms, corresponding lattice structures, shape memory effect and superelasticity are summarized.

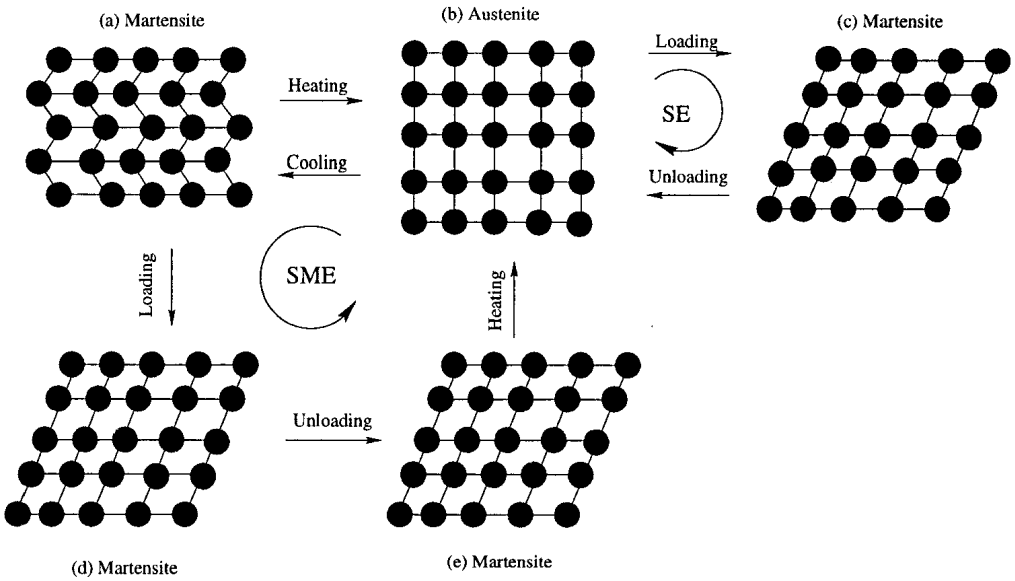

Figure 1.8. Deformation mechanism and lattice structure of SMAs [12]

1.1.4. Nitinol

Nitinol is the most known alloy among SMAs, it has many commercial applications, especially in medicine, because of its good biocompatibility, good magnetic resonance imaging opacity and corrosion resistance. It has properties superior to many other shape memory alloys and it shows superelasticity and shape memory properties at desired temperature range. This makes Nitinol popular in research and experiments. There are many experimental results for nitinol in literature which make it also suitable for numerical research.

There are different compositions of Nitinol but equiatomic composition (i.e., 50 at.% of Ni and Ti) shows the maximum A_f temperature (120^0C) for all NiTi compositions studied. It is known that changing the composition leads to change in transformation temperature. For example A_f is -40^0C for 51 at.% Nickel. 55 at.% Nickel composition shows transformation temperatures in the range of -10^0C to 60^0C and has enriched corrosion resistance [8].

1.1.5. Applications of Shape Memory Alloys

Shape Memory alloys are a subgroup of smart materials which have superior properties compared to ordinary engineering materials. Two major characteristics are superelasticity and shape memory effect. These special features make them attractive for engineers and scientists and designers have been trying to utilize them in applications that simplify our lives. Furthermore, there are many application fields of SMAs but well-known ones belong mainly to the areas of aerospace and medicine.

In aerospace industry, SMAs are generally used to actuate small elements in structures such as variable geometry airfoil where airfoil changes its configuration from symmetric to cambered [8, 13]. There are many studies focused on rotorcrafts and one of them is the SMA torque tube to change the twist of rotor blades. It forms different blade configurations and optimizes performance of aircraft in flight regimes [8]. SMAs were also implemented in Mars Pathfinder to activate an instrument to measure dust

collection from the surface of Mars. Moreover, smart wings, active flexible wings, solar panels and frangibolt device in aerospace applications are designed by using major properties of shape memory alloys.

NiTi has properties such as high corrosion resistance and biocompatibility, that make it suitable for medical applications. Biocompatibility is a serious concern because most devices are invasive, the material must not produce any allergic reaction inside body. Also, fatigue endurance of invasive material used should be high to have long service life in human body. According to many studies, biocompatibility of NiTi is higher than most of engineering materials. There are many medical applications such as guidewires, root canal surgery drills, atrial septal occlusion device, artificial bone implants, etc.

Another example of SMA application is stent, which is used in cardiac arteries to increase diameter of the vessel to enhance blood flow. Since NiTi is superelastic, it can be deformed in large amounts without any plastic deformation, and is used to produce self-expanding stents. A self-expanding stent is compressed and replaced by means of a long wire inside vessel. When stent reaches the problematic site of vessel, it is released. It expands to over twice of its compressed diameter and exerts a nearly constant pressure on walls of the vessel concerned. Another application is orthodontic SMA wires used to align teeth to provide nearly constant force over a long period of time [14]. During phase transformation, Nitinol exerts constant stress over a large strain increment. Former dental wires were stainless steel and retensioning was needed every three weeks.

There are many other applications in different fields of industry. Coupling devices and fasteners are examples of industrial applications that use shape memory property of SMAs to join pipes. At ambient temperature the coupling is processed, then it is cooled and deformed to enlarge its diameter. Expanded coupling is placed over the location to be joined and then it is heated up to ambient temperature, it recovers its memorized shape and fastens parts. There are thermal actuators made of shape memory alloys to detect a temperature change in environment. E.g., switchers for

cookers, coffee makers, kettles, fans for automobile radiators [7]. Other most common applications are mobile phone antennas, eyeglass frames, hats, golf clubs, etc.

1.2. Constitutive Models

Benefiting from fundamental properties of SMAs, many important industrial applications have been developed and this brought an increase in number of research and development on shape memory alloys and their products. Most of the researches for SMAs had been devoted to the studies of their thermomechanical properties, shape memory effects, martensitic transformation characteristics and associated superelasticity.

There are many studies about the mathematical models of shape memory alloys to understand and describe the main behaviors of these alloys since they have remarkable capabilities and common applications. Although SMAs were discovered in 1960s, the experimental investigations and mathematical models have been improved since 1980s. Most of the early researches are devoted to the material properties and the experimental studies which investigate the shape memory effect and superelasticity. In later studies, various researchers developed and are still developing mathematical models in order to explain the stress-strain-temperature relations during transformation behavior.

In the existing studies, the mechanical behavior of SMAs are modeled either microscopically or macroscopically. The micromechanical models deal with the phenomena in molecular level and obtain macro-scale quantities (macro-stress, macro-strain) from the micro-scale quantities (habit planes, martensitic variants, micro-stress, micro-strain). The construction of mathematical models from the micromechanical standpoint have been studied by several authors such as Delaey, Krishnan and Warlimont [15, 16, 17], Achenbach, and Müller [18], Fischer and Tanaka [19], Patoor et al. [20, 21], Sun and Hwang [22, 23], Marketz and Fischer [24], Comstock et al. [25], Levitas et al. [26], Lu and Weng [27], Siredey et al. [28], Gall et al. [29], Muller and Seelecke [30], Jung et al. [31], Stupkiewicz and Petryk [32], Peng et al. [33] and Wang et al. [34].

Macroscopic models deal with the phenomenological characteristics of the SMA and they are categorized according to the theory which they are based on. The first group begins to construct the model from phase transformation kinetics. There are many studies in literature on this theory. Tanaka [35, 36, 37, 38, 39] and coworkers who are the pioneers of this theory investigated transformation pseudoelasticity and shape memory effect from the thermomechanical point of view. They set up thermomechanical constitutive equations along with the kinetics of transformation and applied the theory to explain the stress-strain-temperature behavior of the material. This theory has then been developed and used by many researches. Liang and Rogers [40, 41], Brinson [42], Ivshin and Pence [43, 44], Boyd and Lagoudas [45, 46], Kasper [47], Qidwai and Lagoudas [48], Zhu et al.[49], Mook [12], Janetti [50] and Reese and Christ [51] are the authors who adapted and applied the transformation kinetic laws in their studies.

The other group of phenomenological models were generated from the concept of plasticity. Bertram [52], Lazghab[53] and Panoskaltsis et al.[54] are some of the researchers who studied this model. Also Auricchio and coworkers [55, 56, 57, 58, 59, 60, 61, 62, 63, 64] proposed a model using generalized plasticity concepts and published many studies on superelasticity and shape memory effect of SMAs. In 1996, Lubliner and Auricchio [63] showed that generalized plasticity is convenient to characterize materials undergoing phase transitions and proposed a model based on Drucker-Prager flow potential in order to represent the behavior of SMAs. Then they presented a uniaxial model [56] and simulated the shape-memory effect and the superelastic behavior. In 1997, Auricchio, Taylor and Lubliner [61, 62] developed one- and three-dimensional constitutive models based on an internal-variable formalism. Beside the basic features of SMAs, the single-variant martensite orientation process is covered. Numerical simulations of typical tests were carried out and compared with experimental data. In the subsequent study of Auricchio and Sacco [58] the different elastic properties between austenite and martensite were taken into consideration.

1.2.1. Auricchio-Taylor-Lubliner Method

In this study ABAQUS is used as a post and pre-processor and a built-in material subroutine which uses the constitutive model of Auricchio et al.[61, 62] is utilized in the analyses of SMAs. In the constitutive model, generalized plasticity of Drucker-Prager type which is based on internal-variable model of rate-independent inelasticity is applied. For more details see references [7, 63].

In the material model the control variables are assumed to be Kirchhoff stress, τ, and the temperature, T. Internal variables are;

- the austenite fraction, ξ_A,
- the single variant martensite fraction, ξ_S,
- the multiple variant martensite fraction, ξ_M,

In order to simplify the material model, one-dimensional (1-D) model is presented here. The material is assumed to be isotropic and multiple variant phase is not present. In uniaxial model the control variables are uniaxial stress, σ, and temperature, T. Either the single-variant martensite fraction, ξ_S, or austenite fraction, ξ_A, can be selected as internal variables. There is a relation between fractions that is always satisfied;

$$\xi_A + \xi_S = 1 \tag{1.1}$$

and

$$\dot{\xi}_A + \dot{\xi}_S = 0 \tag{1.2}$$

where dot means time derivative. According to Equation 1.1, there is only one independent variable and it is chosen as ξ_S in the model.

It is stated that there are three phase transformations in general:

- The conversion of austenite into single-variant martensite (A$\rightarrow$ S)
- The conversion of single-variant martensite into austenite (S$\rightarrow$ A)

• The reorientation of the single-variant martensite (S→ S)

It is assumed that during the reorientation process, there is no change in the martensitic fraction and the change in ξ_S is denoted by considering only the first two processes;

$$\dot{\xi}_S = \dot{\xi}_S^{AS} + \dot{\xi}_S^{SA} \tag{1.3}$$

The superscript AS refers to conversion of austenite into single-variant martensite and SA refers to conversion of single-variant martensite into austenite.

1.2.1.1. Conversion of austenite into single-variant martensite: A to S. Drucker-Prager type loading function, which was introduced to model phase transformation from austenite to single-variant martensite, is

$$F^{AS}(\tau, T) = ||\mathbf{t}|| + 3\alpha p - C^{AS}T \tag{1.4}$$

where $\mathbf{t}$ is the deviatoric part of the stress defined as $\mathbf{t} = \tau - tr(\tau)I/3$, I is identity matrix, p is the pressure, C^{AS} is the stress temperature coefficient, α is the pressure sensitivity and $||.||$ indicates Euclidean norm such as $||\mathbf{t}|| = \left[\sum_{A=1}^{3} (\mathbf{t}_A)^2\right]^{1/2}$.

The initial and final transformation functions can be stated as

$$F_s^{AS} = F^{AS} - R_s^{AS} \tag{1.5}$$

$$F_f^{AS} = F^{AS} - R_f^{AS} \tag{1.6}$$

where

$$R_s^{AS} = \left[\sigma_s^{AS}\left(\sqrt{\frac{2}{3}} + \alpha\right) - C^{AS}T_s^{AS}\right] \tag{1.7}$$

$$R_f^{AS} = \left[\sigma_f^{AS}\left(\sqrt{\frac{2}{3}} + \alpha\right) - C^{AS}T_f^{AS}\right] \tag{1.8}$$

σ_s^{AS} , σ_f^{AS} , T_s^{AS} and T_f^{AS} are material parameters. "s" stands for start and "f" stands for finish. The region in which the transformation occurs from austenite to single-variant martensite is shown in Figure 1.9. The arrow indicates the direction of activation. The necessary conditions to activate the production of single variant martensite are

$$F_s^{AS} > 0 \text{ , } F_f^{AS} < 0 \text{ and } \dot{F}^{AS} > 0$$

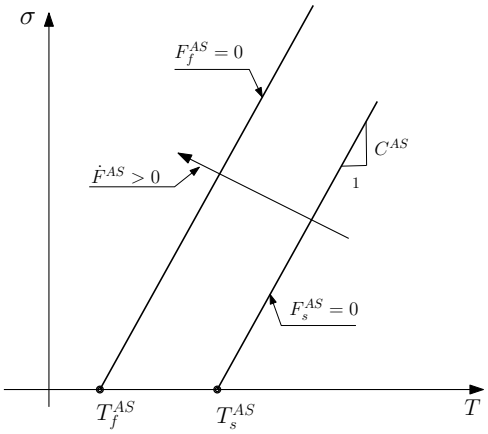

Figure 1.9. Conversion of austenite into single-variant martensite (A→ S) in 1-D model

The evolution of single variant martensite fraction is assumed to be either in quadratic form or linear form;

• Quadratic form: $\dot{\xi}_S^{AS} = H^{AS}\beta^{AS}(1-\xi_S)\frac{\dot{F}^{AS}}{(F_f^{AS})^2}$ with β^{AS} being a material parameter measuring the speed of the transformation.

• Linear form: $\dot{\xi}_S^{AS} = -H^{AS}(1-\xi_S)\frac{\dot{F}^{AS}}{F_f^{AS}}$

The scalar parameter H^{AS} is defined by the relation

$$H^{AS} = \begin{cases} 1 & \text{if} \quad F_s^{AS} > 0, \quad F_f^{AS} < 0, \quad \dot{F}^{AS} > 0 \\ 0 & \text{otherwise} \end{cases} \tag{1.9}$$

1.2.1.2. Conversion of single-variant martensite into austenite: S to A. Drucker-Prager type loading function defined as;

$$F^{SA}(\tau, T) = ||\mathbf{t}|| + 3\alpha p - C^{SA}T \tag{1.10}$$

The initial and final transformation functions are

$$F_s^{SA} = F^{SA} - R_s^{SA} \tag{1.11}$$

$$F_f^{SA} = F^{SA} - R_f^{SA} \tag{1.12}$$

where

$$R_s^{SA} = \left[\sigma_s^{SA}\left(\sqrt{\frac{2}{3}} + \alpha\right) - C^{SA}T_s^{SA}\right] \tag{1.13}$$

$$R_f^{SA} = \left[\sigma_f^{SA}\left(\sqrt{\frac{2}{3}} + \alpha\right) - C^{SA}T_f^{SA}\right] \tag{1.14}$$

σ_s^{SA} , σ_f^{SA} , T_s^{SA} and T_f^{SA} are material parameters.“s” stands for start and “f”

stands for finish. The region in which the transformation occurs from single-variant martensite to austenite is shown in Figure 1.10 . The arrow indicates the direction of activation. The necessary conditions to activate the production of austenite are

$$F_s^{SA} < 0,\ F_f^{SA} > 0 \text{ and } \dot{F}^{SA} < 0$$

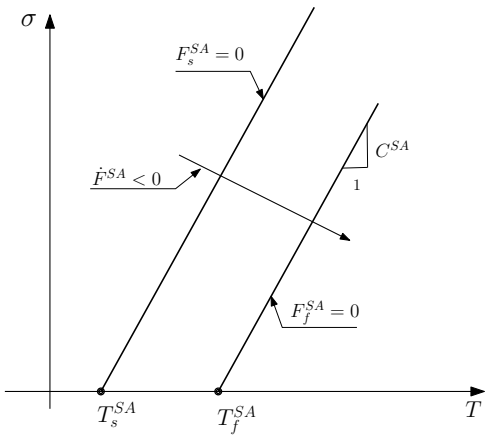

Figure 1.10. Conversion of single-variant martensite into austenite (S→ A) in 1-D model

The evolution of single-variant martensite fraction is assumed to be either in quadratic form or linear form;

• Quadratic form: $\dot{\xi}_S^{SA} = H^{SA}\beta^{SA}(1-\xi_S)\frac{\dot{F}^{SA}}{(F_f^{SA})^2}$ with β^{SA} being a material parameter measuring the speed of the transformation.

• Linear form: $\dot{\xi}_S^{SA} = -H^{SA}(1-\xi_S)\frac{\dot{F}^{SA}}{F_f^{SA}}$

The scalar parameter H^{SA} is defined by the relation

$$H^{SA} = \begin{cases} 1 & \text{if} \quad F_s^{SA} > 0, \quad F_f^{SA} < 0, \quad \dot{F}^{SA} > 0 \\ 0 & \text{otherwise} \end{cases} \tag{1.15}$$

1.2.1.3. Single-variant martensite reorientation process: S to S. Drucker-Prager type loading function defined as

$$F^{SS}(\tau, T) = ||\mathbf{t}|| + 3\alpha p - C^{SS}T \tag{1.16}$$

The transformation function is

$$F_s^{SS} = F^{SS} - R_s^{SS} \tag{1.17}$$

where

$$R_s^{SS} = \left[\sigma_s^{SS}\left(\sqrt{\frac{2}{3}} + \alpha\right) - C^{SS}T_s^{SS}\right] \tag{1.18}$$

σ_s^{SS} , C^{SS} , T_s^{SS} are material parameters. The condition for the reorientation process is

$$F_s^{SS} > 0 \tag{1.19}$$

When $\xi_S > 0$ the reorientation process is active. For a detailed discussion of the constitutive model behind the UMAT/Nitinol refer to [61, 62].

1.3. Previous Studies on Fracture of SMAs

As applications of SMAs increase, good understanding of failure mechanisms of the material are needed. In literature, there are not many studies on fracture properties and failure of SMAs.

There are some experimental work on fatigue of SMAs: In 1999, McKelvey and Ritchie [65] studied fatigue-crack propagation behavior of superelastic alloy Nitinol.

Their aim was to study the effect of environment on cyclic crack-growth resistance in a $50Ni-50Ti$ (atom %) alloy to improve functioning of medical stents. They performed experiments at human body temperature, 37^0C, using disk-shaped compact-tension specimens. The effect of cyclic loading on uniaxial behavior was investigated and it was concluded that, there is a cyclic softening. The stress at which martensite transformation begins decreases with increasing the number of cycles. They also found out that Nitinol has the lowest fatigue-crack growth resistance among the other main alloys currently used for implant applications.

In 2001, McKelvey and Ritchie [11] investigated effect of stress-induced martensitic transformation on crack-growth resistance in Nitinol (50Ni-50Ti). They found out that fatigue-crack growth resistance of martensite is superior to that of stable austenite and superelastic austenite. They observed that superelasticity does not improve crack growth resistance in NiTi. It was also revealed that phase transformation was suppressed during fatigue crack growth by the hydrostatic state of stress ahead of the crack tip in plane strain. On the other hand in the case of plane stress, stress-induced martensitic transformation occurs at crack tip because hydrostatic stress state is not present at the crack tip.

In 2003, McNaney et. al. [66] performed tension-torsion tests on thin-walled tubes made of a polycrystalline superelastic shape-memory alloy. They explained that the response of material, changes along the two loading axes and microstructural texture plays an important role on stress-induced phase transformation.

Chen et al. [67], in 2005, performed mechanical tests using NiTi specimens (50.7 at. pct.) and studied fracture process using scanning electron microscope (SEM). They observed that main crack propagates in direction of the maximum normal stress, microstructure has little effect on direction of crack propagation and in a coarse grain region, resistance to crack propagation decreases.

In 2007, Robertson et al [68] used X-ray microdiffraction to measure three-dimensional strains, phases and crystallographic alignment ahead of growing fatigue

crack. They determined that shape and size of the crack-tip transformation zone and fatigue propagation path are influenced by local texture. Main crack is stress-control propagated in line with the direction of the maximum normal stress.

Daly et al.[69] in 2007 presented an experimental study on fracture properties of edge-cracked superelastic thin sheets of nitinol under uniaxial tension test. They observed a phase boundary nucleation and propagation of fracture sample by means of Digital Image Correlation (DIC) and they measured plane strain crack initiation fracture toughness. The images, combined with the relatively high value of fracture toughness for thin sheets of Nitinol, indicated a complex mechanism where phase transformation contributes to toughening around the crack tip.

In 2008 Wang et al.[34] measured fracture toughness of a NiTi pseudoelastic alloy experimentally using compact tension (CT) specimens. They found that fracture mechanism is dominated by cleavage fracture and increasing crack velocity results in brittle response and fast fracture.

In 2008, Gollerthan et al. [70] studied mechanical behavior of a superelastic NiTi, CT specimen. They used linear elastic fracture mechanics approach to determine critical stress intensity factors and the size of the pseudoplastic zone.

Gollerthan et al. investigated crack extension under static loading in martensitic, pseudoelastic and austenitic NiTi in 2009 [71]. Miniature CT specimen were used in mechanical experiments. According to their study, stress intensity vs displacement curves of martensitic and pseudoelastic NiTi show similar trend to those observed for ductile materials. Although martensitic and pseudoelastic NiTi have different mechanical and thermal properties, cracks propagate around similar stress intensities because of the fact that in both cases, cracks grow into detwinned martensitic variant. They showed that stress-induced martensite can be formed ahead of the crack tip in plane strain conditions contrary to the study of McKelvey and Ritchie in which it was claimed that phase transformation is suppressed by hydrostatic stress ahead of the crack tip in plane strain [11].

In 2009, Wang et al. [72] performed tensile tests on double-notch NiTi plates with different notch types and sizes. They examined phase transformation, stress-strain, plastic deformation, crack initiation and fracture surface. They showed that notch type and notch size have an effect on crack initiation. They also performed FE analysis to investigate stress-strain and plastic deformations using a new constitutive model that considers permanent plastic deformation of superelastic SMAs.

There are few analytical studies on fracture toughening mechanism of SMAs in literature. In one of them, in 1997, Birman [73] examined Mode-I fracture of an SMA plate under isothermal conditions. He used constitutive theory of Tanaka and investigated effect of superelastic phase transformation on stress intensity factor. He studied size of the plastic zone occuring in the stress induced martensite (SIM) region.

In 1994, Stam and Giessen [74] explored influence of partial or full reversibility of a stress-induced phase transformation around crack tip and toughness improvement during crack growth for zirconia ceramics and SMAs. They adopted the model of Sun et al. [75] and carried out a full field finite element analysis for crack propagation under small scale transformation conditions. It was found that if the phase transformation is irreversible, it leads to toughening of the material.

Yi and Gao, in 2000, [76] applied Sun and Hwang's [22] constitutive model and investigated transformation zone for both stationary and steady advanced cracks under Mode-I loading. They found that martensite transformation reduces crack tip stress intensity factor and increases the toughness. They also mentioned that temperature has an effect on toughening process of SMAs. In a subsequent study, Yi et. al. (2001) [77], examined a macrocrack under mixed mode loading. According to their analytical results, martensite transformation results in a reduction in energy release rate and fracture toughness increases.

In addition, in 2002, Yan et. al. [78] studied effects of stress induced martensite transformation on fracture properties of superelastic SMAs theoretically and compared them with phase transformation in zirconia ceramics. They also performed finite el-

ement analysis for a semi-infinite crack using ABAQUS. According to their results, martensite transformation occurs at crack tip during steady-state crack propagation while partial reverse transformation occurs in the wake. There exists a volume contraction associated with stress-induced martensite transformation and this fact has an effect on stress intensity factor. In most of the superelastic SMAs, volume contraction during phase transformation increases stress intensity factor at the crack tip and decreases fracture toughness in contrast to zirconia ceramics.

In 2003, Yan et al. [79] performed a theoretical study on effect of plasticity on stress induced transformation. They modified the phenomenological constitutive model of Auricchio and Lubliner [61, 63] and added effect of plasticity and volume change during transformation. They stated that there is a limit for plastic strain to stabilize martensite and when this limit is exceeded, martensite will not retransform back to austenite. They also implemented the modified constitutive model into ABAQUS and analyzed plastic zone at crack tip of a semi-infinite SMA sample under plane strain.

Xiong and Liu (2007) [80] studied thermally induced fracture in Ni-Mn-Ga, Ni-Ti and Cu-Al-Ni. They found out that there exists stress redistribution around the crack tip as a result of stress-induced martensitic transformation and this leads to an increase in the crack tip stress intensity factor and a decrease in fracture toughness.

Further, a certain number of numerical analyses on fracture properties of SMAs are present in literature. Freed and Banks-Sills [81] in 2007, investigated numerically transformation toughening behavior of a slowly propagating crack in a shape memory alloy under plane strain and Mode-I deformation. Transformation zones near crack tip were derived from first term of the asymptotic solution for linear elastic material and it was found that shape of regions in the neighborhood of the crack tip coincide with the shape of the plastic zone in plastically deformed materials. Further, they implemented a cohesive zone model to simulate crack growth using finite elements and stated that the choice of cohesive strength has a great influence on toughening behavior of material and reversibility of phase transformation can reduce the toughening of the alloy.

In 2007, Wang [82] investigated evolution of stress-strain and martensite transformation in front of a notch in shape memory alloy NiTi CT specimen by finite element method. He stated that martensite transformation zone in front of a crack or a notch tip in SMAs is similar to plastic zone in normal metals and transformation zone can be characterized by plastic strain and the yield law in normal metals can be used in order to examine the martensite transformation. In that study, as a material model, an elastic-plastic constitutive model is used. He shows that with the increase of the applied load, a partially martensitic zone firstly appears and grows in front of the notch tip, then it becomes a fully martensitic zone and a plastic deformation zone occurs at fully martensitic zone. In his following paper [83], he analyzed the effect of martensite transformation on fracture behavior of NiTi in a notched specimen under plane stress state. He concluded that martensite transformation increases fracture load and improves toughness. According to his study apparent fracture toughness increases by 47%.

1.4. Objective of This Study

Most of works on Shape Memory Alloys study material properties, phase transformation and constitutive models. Although experimental, numerical and analytical techniques have recently increased, studies on fracture mechanics of SMAs are limited. Effect of phase transformation on fracture behavior of superelastic SMAs during loading and unloading are studied in literature but crack initiation, crack propagation are generally investigated experimentally.

Variation of stress intensity factor at crack tip and the effect of phase transformation on fracture toughness are major topics of numerical and analytical studies but there are only few detailed works. Effect of stress-induced martensite transformation on fracture toughness is yet to be clarified; there is no consensus on whether the fracture toughness increases or decreases as a result of superelasticity.

Main objective of this study is to understand the effect of phase transformation on fracture behavior of a superelastic Nitinol. Considering previous studies on the

concept, results of this study are intended to contribute to discussion on fracture of SMAs. The aim is to explore transformation region around crack tip using a 2-D edge-cracked model under plane stress. Using finite elements, fracture mechanics properties such as J-integrals, energy release rates and stress-intensity factors are investigated.

This study is organized as follows: In Chapter 2 an edge-cracked homogenous plate is modeled to verify the model and to compare the results of finite elements with analytical ones. First section of Chapter 3 deals with material model implementation into ABAQUS through a built-in UMAT. In subsequent sections effect of crack length and amount of loading on phase transformation around crack tip are studied. J-integrals and energy release rates are calculated. Stress intensity factors are computed, closed-form solution of Mode-I stress intensity factor proposed by Xiong and Liu [80] is discussed and finite element results and closed-form solutions are compared. In addition, a parametric study of the effect of material properties is carried out. In Chapter 4, a discussion on fracture toughness change as a result of phase transformation in SMAs is presented. Results of this study are discussed and compared to available results in literature in discussion section.

2. EDGE CRACKED HOMOGENEOUS PLATE

The main objective of this chapter is to analyze the plane stress fracture mechanics properties of a 2-D homogenous material under Mode-I loading using ABAQUS and to compare the results with analytical ones available in literature, before applying the procedure to an edge-cracked SMA plate.

2.1. Modeling & Material Properties

It is important to verify the constructed model and its mesh quality to establish the accuracy of the results. For this purpose, firstly, a linearly elastic and homogenous 2-D edge-cracked plate is modeled in ABAQUS as a plane stress analysis. A rectangular plate is loaded uniaxially, in pure Mode-I condition.

The geometry of the specimen is shown in Figure 2.1. H is the height, W is the width of the plate, a is the crack length. The dimensions chosen for edge-cracked specimen are; $H = 200$ mm, $W = 100$ mm and $a = 30$ mm in order to have the ratio of $H/W = 2$ and $a/W = 0.3$. The crack length is set to 20, 25, 30, 35 and 40 mm respectively and the same analyses are performed to observe the effect of different a/W ratios on the stress-strain distribution at the crack tip and on the fracture properties of the analyzed specimen. The thickness of the specimen is set to 1 mm, applied load is 80 MPa and the material properties are $E = 75$ GPa and $\nu = 0.3$.

Due to symmetry, only the upper half of the plate is constructed. For the crack specimen, an eight-node biquadratic plane stress quadrilateral (CPS8R) element is used to simulate a plane stress analysis.

The model is divided into regions and all regions have different mesh density. The crack tip is partitioned as circular and finely meshed. In order to have more accurate results, the mesh density is increased toward the crack tip. Moreover, most of the parameters can be evaluated as a function of angle in polar coordinates through the

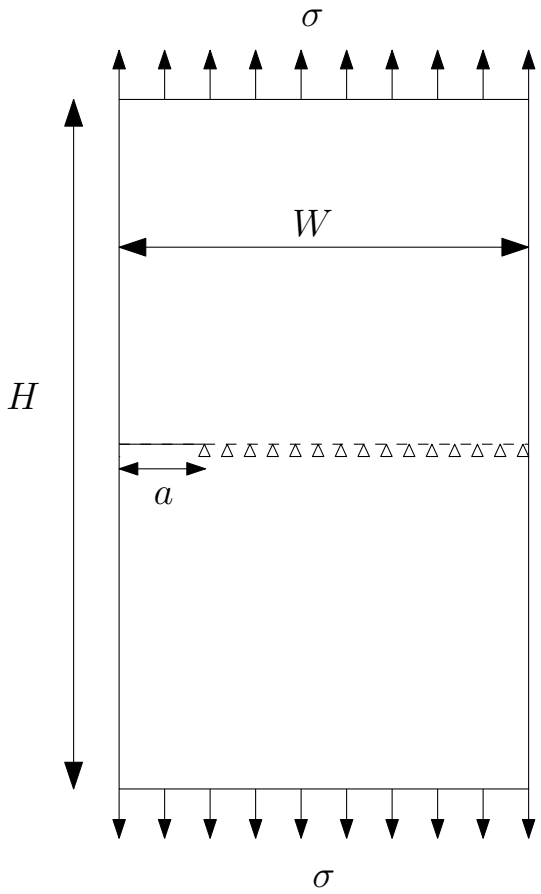

Figure 2.1. Geometry of the 2-D edge-cracked specimen

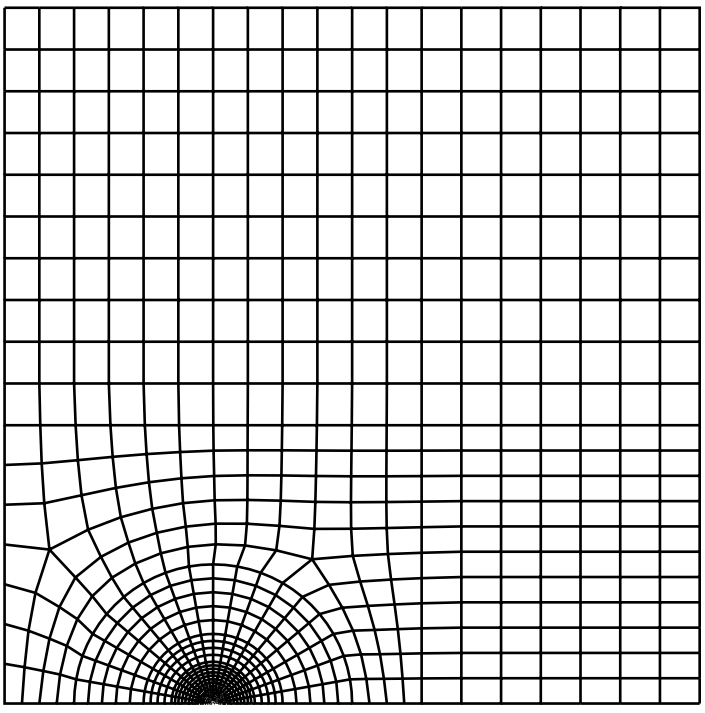

Figure 2.2. Mesh geometry of 2-D edge-cracked specimen model

construction of circular mesh. The outer regions have coarser and rectangular mesh since they are far from the crack tip and has a little effect on the solution. The mesh configuration of the model is shown in Figure 2.2 and the refinement of FEA mesh around the crack tip is illustrated in Figure 2.3.

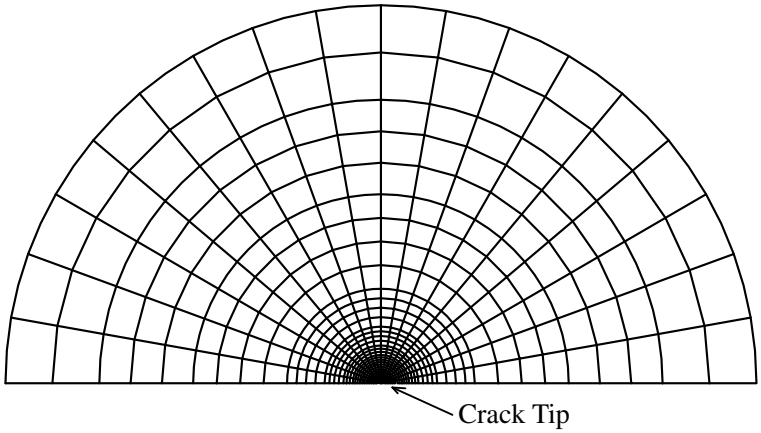

Figure 2.3. Mesh configuration of the crack tip

2.2. Fracture Properties

In fracture mechanics analysis, the stress intensity factor, which is a measure of intensity of near tip stress and strain fields, is a key parameter. The whole stress field at the crack tip can be determined if the stress intensity factor is known. In this section, stress intensity factors for the same plate with different crack lengths, are calculated to see the accuracy of the model by comparing finite element results with the data available in literature. Then the model is used in the analysis of the Nitinol plate.

Besides the analytical solutions, one of the methods for calculating the stress intensity factor is the use of energy release rate, G (see Appendix A). J-integral which is a line integral calculated at an arbitrary path around the crack tip is a more general version of energy release rate and it is used to determine the crack tip stress and strain in nonlinear materials. It is known that $J = G$ in linear elastic materials. In order to calculate stress intensity factors, SIFs, for the model, G and J-integrals are evaluated using ABAQUS and compared with the analytical solutions.

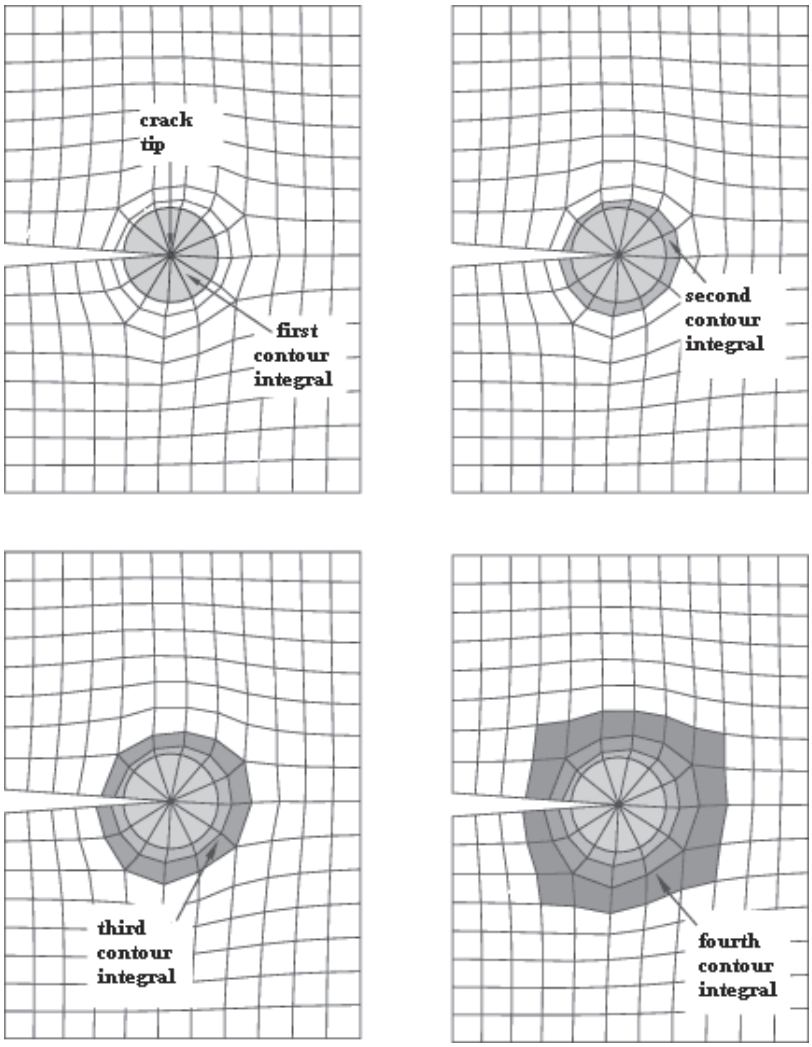

Figure 2.4. Representation of elements used in contour integral calculation [84]

The contours which are selected to calculate the J-integral around the crack tip in the finite element model are shown in Figure 2.4 schematically.

In order to verify the accuracy of the model, J-integral values obtained from ABAQUS for different crack lengths are calculated and tabulated in Table 2.1 to see the contour dependence of the J-integral. It is seen that J-integral values are the same except for the first two paths and then it converges to a constant value. Elements used in the first two contours have a higher aspect ratio that's why the first two J-integral values are different from the others. The values are same for the rest of the contours and this proves the contour independency of the J-integral in linear elastic homogenous materials and the validity of the mesh configuration.

Table 2.1. J-integral values obtained from ABAQUS for different a/W ratios, load = 80 MPa

J-integral values for homogenous plate					
Contour	***a/W* ratios**				
Number	**0.20**	**0.25**	**0.30**	**0.35**	**0.40**
1	10.04	15.06	22.21	32.56	47.89
2	10.03	15.04	22.18	32.54	47.85
3	10.03	15.05	22.19	32.55	47.86
4	10.03	15.05	22.19	32.55	47.87
5	10.03	15.05	22.19	32.55	47.87
6	10.03	15.05	22.19	32.55	47.87
7	10.03	15.05	22.19	32.55	47.87
8	10.03	15.05	22.19	32.55	47.87
9	10.03	15.05	22.19	32.55	47.87
10	10.03	15.05	22.19	32.55	47.87

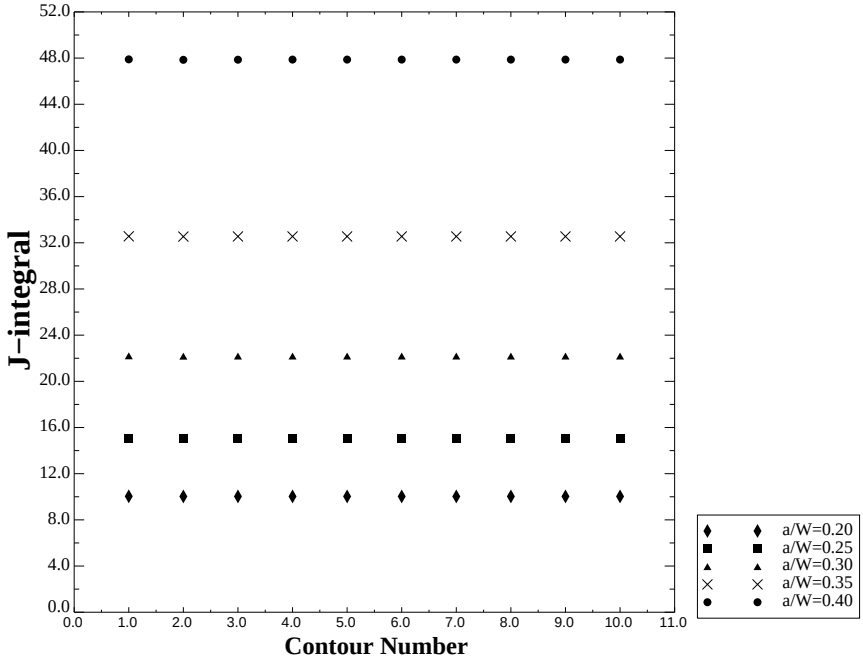

Figure 2.5. J-integral values for different a/W ratios

Further, the energy release rate, G, is calculated for the homogenous plate. G is energy dissipated per unit area of new fracture surface and it is also defined as the change of elastic strain energy per unit crack area, $G \approx \frac{\Delta U}{t\Delta a} = \frac{\Delta U}{\Delta A}$, where ΔU is the change in elastic strain energy, t is thickness, Δa is the change in crack length and ΔA is the change in crack surface area.

In the model, the length of the crack is increased by 0.5 mm and the differences between strain energies are calculated. The J-integrals obtained from ABAQUS and G values calculated from the strain energy output of ABAQUS are displayed in Table 2.2. It can be seen that there is a significant correspondence between the values.

Table 2.2. J-integral values obtained from ABAQUS and the strain energy release rates, G

a/W	**J-integral**	$G \approx \frac{\Delta U}{\Delta A}$
0.20	10.03	10.25
0.25	15.05	15.35
0.30	22.19	22.62
0.35	32.55	33.18
0.40	47.87	48.81

Next, the stress intensity factors for Mode-I loading are calculated using energy release rates. They are listed in Table 2.3 with the ones obtained from ABAQUS and the analytical solutions. Analytical results are computed using K_I solutions for common test specimens [85]. As can be seen from Equation 2.1, stress intensity factor (SIF) depends only on the geometry of the plate and the loading. The material property does not have an effect on SIF. For single-edge notch tension specimen the K_I solution is given by

$$K_I = \frac{P}{t\sqrt{W}} \times \frac{\sqrt{2\tan\frac{\pi a}{2W}}}{\cos\frac{\pi a}{2W}} \left[0.752 + 2.02\left(\frac{a}{W}\right) + 0.37\left(1 - \sin\frac{\pi a}{2W}\right)^3\right] \tag{2.1}$$

where P is applied load, t is thickness, a is crack length and W is width of the plate. FE solutions are taken directly from ABAQUS and the solutions get from energy release rate is calculated from the following equation (See details in Appendix A).

$$G = \frac{K_I}{E'}$$

E' is the Young's modulus and equal to

$$E' = \begin{cases} E \quad \text{if} \quad \text{plane} \quad \text{stress} \\ E/\left(1-\nu^2\right) \quad \text{if} \quad \text{plane} \quad \text{strain} \end{cases}$$

Table 2.3. Stress intensity factors calculated with different methods for different a/W ratios homogenous plate, ($E = 75$ GPa)

Stress Intensity Factor, K_I					
a/W	**Analytical**	**FE**	**error %**	**From G**	**error %**
0.20	866.6	867.5	0.0988	876.7	1.1601
0.25	1059.3	1062	0.2558	1073.1	1.2974
0.30	1285.4	1290	0.3547	1302.6	1.3359
0.35	1557.3	1562	0.2992	1577.5	1.2944
0.40	1890.4	1895	0.2423	1913.3	1.2128

It is obvious that the FE results and the results calculated from G, are very close to the analytical solutions and the corresponding error percentages are very small. This shows the validity of the method of finding K_I by using G and the accuracy of the mesh configuration.

In order to show that there is no material dependency on SIF, similar analyses are performed for different materials with the same plate geometry. The SIFs are displayed in Table 2.4. The analytical solutions and the ones computed directly by ABAQUS are

the same for each case. Also the SIFs computed from energy release rate, G are almost the same and this shows the material independency of SIF in linear elastic homogenous materials.

Table 2.4. Stress intensity factor calculation for homogenous materials with different elastic modulus

	Stress Intensity Factor, K_I			
	E (GPa)	Analytical	FEM	From G
$a/W = 0.30$	22	1285.4	1290.11	1302.55
	28	1285.4	1290.11	1302.61
	62	1285.4	1290.11	1302.62
	75	1285.4	1290.11	1302.61
	200	1285.4	1290.11	1302.31
$a/W = 0.35$	22	1557.3	1562.45	1577.54
	28	1557.3	1562.45	1577.54
	62	1557.3	1562.45	1577.56
	75	1557.3	1562.45	1577.50
	200	1557.3	1562.45	1577.59

3. EDGE CRACKED SMA PLATE

3.1. Modeling & Material Properties

In the case of shape memory alloys, such as Nitinol, it is not a simple task to model and implement the material behavior using ABAQUS to get fracture mechanics properties. Nitinol is a complex material and is difficult to characterize. It can undergo very large elastic deformations. The loading part resembles to that of a hyperelastic material and for this reason early solutions were approximated using the idea of hyperelasticity. Modeling the uniaxial behavior of Nitinol is simpler. On the other hand, the 3-D constitutive model is very complicated. To characterize material properties and to implement the constitutive behavior in ABAQUS, a user defined material subroutine is needed. In this study UMAT/Nitinol subroutine which is written by Hibbitt, Karlsson & Sorensen (West) following the Auricchio-Taylor-Lubliner constitutive model [86] is used. This model is based on generalized plasticity [62, 61, 63].

Material properties used for Nitinol in this study are estimated using an uniaxial tension data given by Daly [87], who studied macroscopic stress-strain behavior of a dog-bone specimen subjected to uniaxial tension under displacement control. The uniaxial stress-strain curve and stress-temperature curve for the superelastic Nitinol are shown in Figure 3.1 schematically.

The model requires 14 constants and the user may anneal the material during analysis by giving an extra parameter [86]. The parameters used in the model are indicated in Figure 3.1 and their definitions are given in Table 3.1.

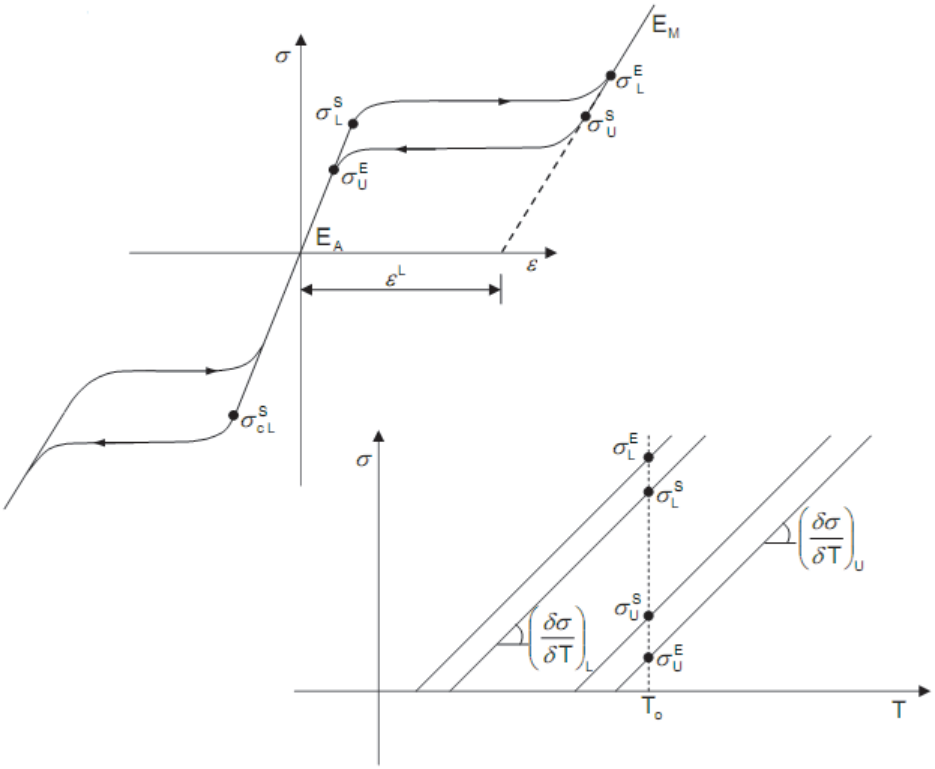

Figure 3.1. Uniaxial behavior of superelastic nitinol [86]

Table 3.1. Input to Umat/Nitinol [86]

E_A	Elastic modulus of Austenite
ν_A	Poisson's ratio of Austenite
E_M	Elastic modulus of Martensite
ν_M	Poisson's ratio of Martensite
ε^L	Transformation strain
$\left(\frac{\delta\sigma}{\delta T}\right)_L$	Rate of change of stress with respect to temperature during loading
σ_L^S	Start of transformation loading
σ_L^E	End of transformation loading
T_0	Reference Temperature
$\left(\frac{\delta\sigma}{\delta T}\right)_U$	Rate of change of stress with respect to temperature during unloading
σ_U^S	Start of transformation unloading
σ_U^E	End of transformation unloading
σ_{CL}^S	Start of transformation stress during loading in compression, as a positive value
ε_V^L	Volumetric transformation strain. If ε^L=ε_T^L, an associated algorithm is used, with ε_T^L computed based on σ_L^S and σ_{CL}^S
N_A	Number of annealings to be performed during the analysis σ_L^S

The parameters used in this model are adopted from the experimental study of Daly [87]. Values for the specified material are;

$$E_A = 75 \text{ GPa},$$

$$E_M = 28 \text{ GPa},$$

$$\nu_A = \nu_M = 0.33,$$

$$(\frac{\delta\sigma}{\delta T})_L = (\frac{\delta\sigma}{\delta T})_U = 5.71 \text{ MPa}/^0\text{K},$$

$$\sigma_L^S = 400 \text{ MPa},$$

$$\sigma_L^E = 410 \text{ MPa},$$

$$\sigma_U^S = 310 \text{ MPa},$$

$$\sigma_U^E = 300 \text{ MPa},$$

$$\varepsilon_V^L = \varepsilon^L = 0.04$$

$$T_0 = 22^0\text{C}.$$

In order to see whether the material model implemented into ABAQUS using UMAT/Nitinol and the uniaxial stress-strain behavior of the material are consistent with the theory, a tensile test is performed in ABAQUS. For a single element test, a plane stress element (CPS4) is generated and uniaxial stress is applied under displacement control. The corresponding stress-strain curve is shown in Figure 3.2. First, the material is in austenitic state and deforms linearly upon loading. Around 0.6% strain, the curve begins to depart from the linear, which is the starting value for the martensite transformation process. During the transformation, stress remains nearly

constant and large deformation occurs. After the completion of transformation around 5.5% strain, Nitinol starts again to deform linearly. If loading continues the material deforms linearly since the material model does not allow for any plasticity. As can be seen from Figure 3.2, uniaxial behavior of this material is similar to the ones in literature (see Figure 1.7) and it is consistent with the given parameters.

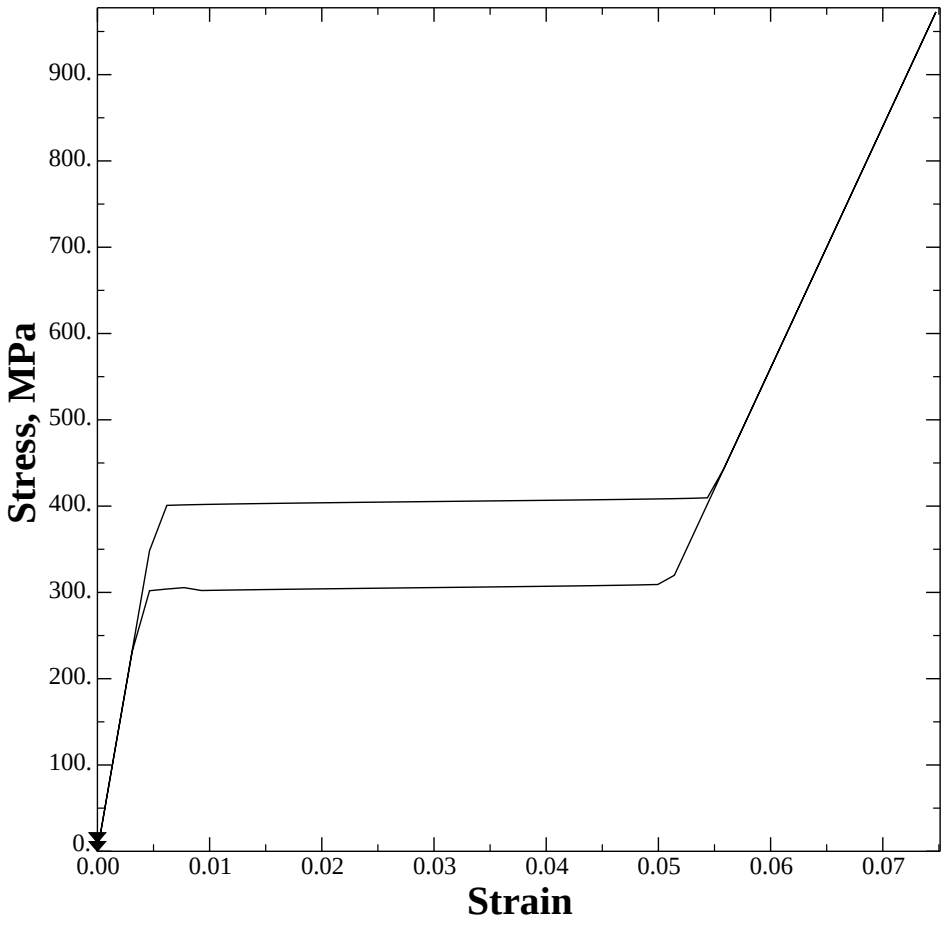

Figure 3.2. The uniaxial tensile stress-strain relationship of nitinol used in the subroutine

3.2. Effect of a Crack on Phase Transformation

A crack inside a material is a stress raiser. In superelastic SMAs increasing of stress at constant temperature may lead to phase transformation. To analyze the effect of a crack on phase transformation in Nitinol, a 2-D edge-cracked plane stress plate is modeled in ABAQUS and subjected to loading from both ends. The crack tip is sharp and the crack faces are traction free. The model used in the fracture analysis of homogenous plate is again used with the same dimensions and the same mesh configuration. W is the width of the plate, a is the crack length and a/W ratio is set to 0.20, 0.25, 0.30, 0.35, and 0.40 respectively.

Upon loading, the stress increases around the crack tip and martensite transformation zone appears in early stages as shown in Figure 3.3. In an ideal superelastic material, the transformed zone vanishes upon unloading. However, in this study, only loading is considered and no unloading or reverse phase transformation is allowed in any step of the analysis.

In Figure 3.4, the phase transformation regions around the crack tip in whole plate can be seen. The red region at the crack tip is totally transformed into martensite; the green region surrounds the red one and is a mixture of martensite and austenite. The blue region is the untransformed phase, austenite. The length of the total transformation zone is measured to be 5.4 mm under 10kN tensile load for $a/W = 0.3$. The stress-strain behavior of the cracked material is similar to that of the uniaxial tension test specimen but the stress values are much larger in the vicinity of the crack tip as expected.

Firstly, the evolution of martensite in front of the crack tip and its fraction is investigated by analyzing the 2-D plates with the same crack lengths but different applied loads. The analysis is performed for different loads to observe the evolution of martensite transformation and the size of transformed and transformation zones. In Figure 3.5 the transformation zones are displayed for edge-cracked specimen of $a/W = 0.3$ at applied tensile loads 1.25kN, 1.6kN, 2kN, 3kN, 3.5kN, 4kN, 4.5kN, 5kN,

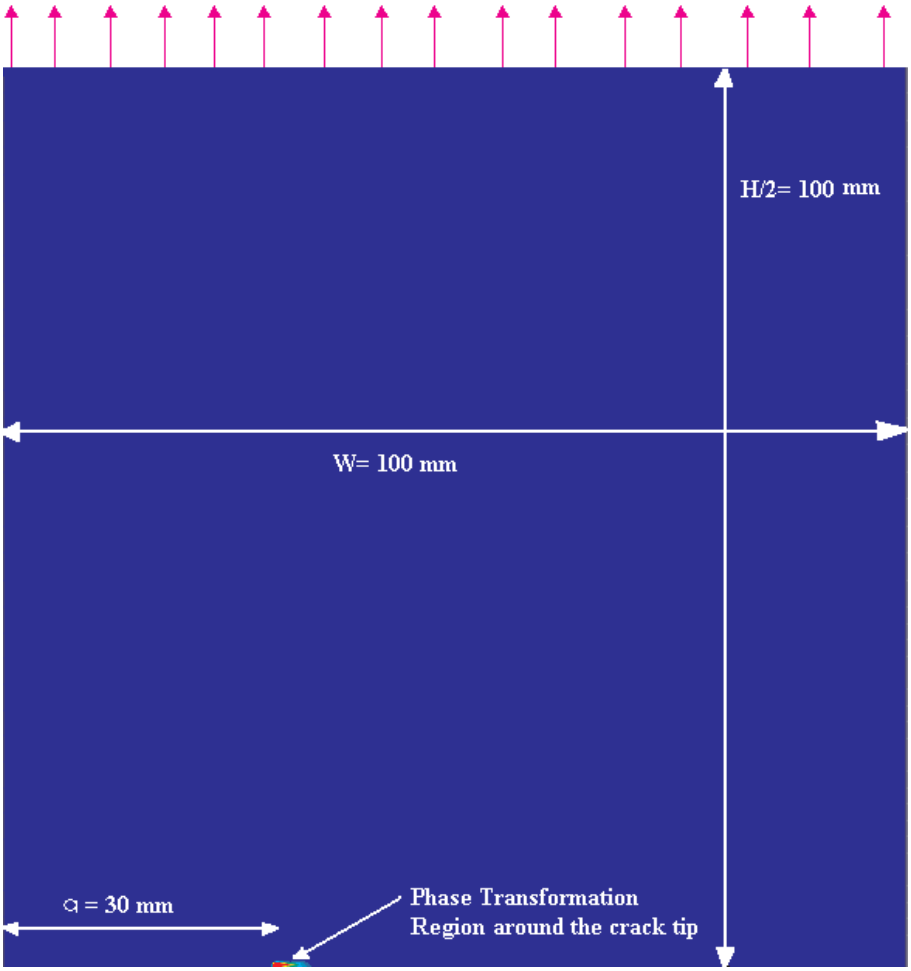

(a) Half of the plate

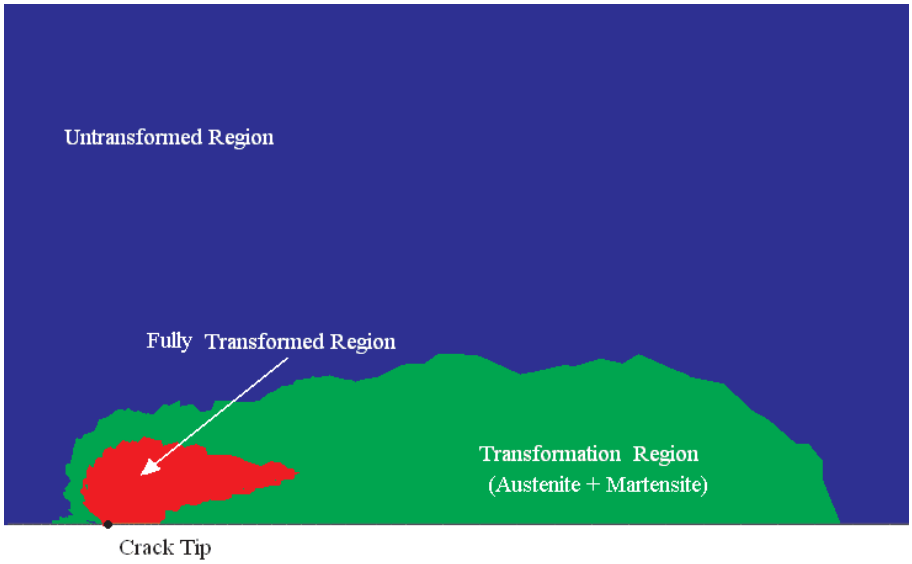

(b) Region around the crack

Figure 3.3. Phase transformation around the crack tip of a 2-D edge-cracked plate with $a/W = 0.30$ subjected to 10 kN tensile loading from both ends

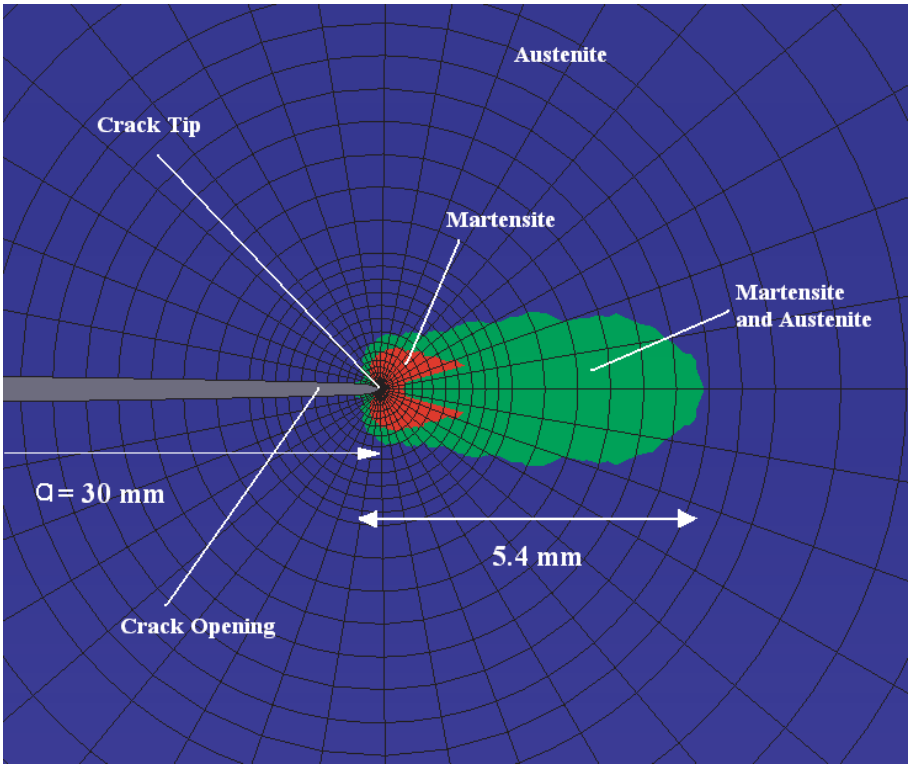

Figure 3.4. Phase transformation regions around the crack tip (magnified from Figure 3.3)

5.5kN and 6kN respectively. It is observed that sharp crack results in a severe stress concentration, therefore phase transformation occurs at the crack tip from the very beginning of loading and the transformation zone is getting larger when the load is increased.

High stresses lead to phase transformation from martensite to austenite and this constitutes non-homogenous zones in front of the crack tip. In Figure 3.5 the zones which are totally transformed into martensite are indicated by claret and the austenite regions are indicated by of navy blue. The regions between claret and navy blue have different martensite fractions. The totally transformed and the transformation regions have the same shape in each loading process but the size increases with increasing load. At the beginning of the loading, the transformation region starts from the crack tip and enlarges as a circle around it. When the transformation advances, the circle shaped zones start to enlarge from crack tip to right side of the plate and takes the shape of kidney.

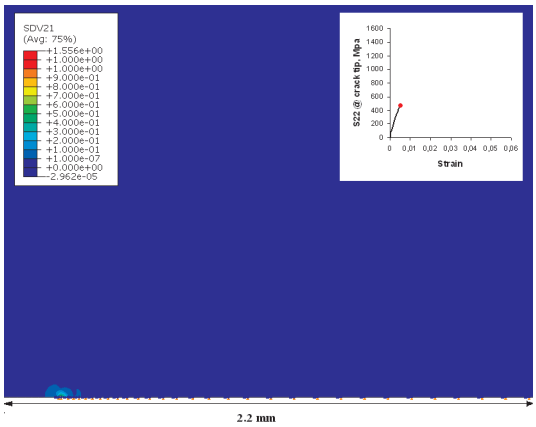

(a) 1.25kN

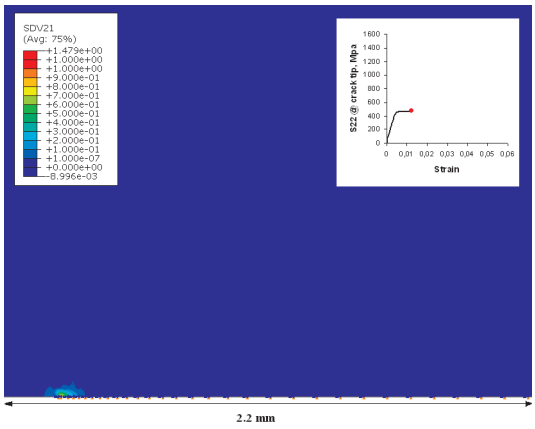

(b) 1.6kN

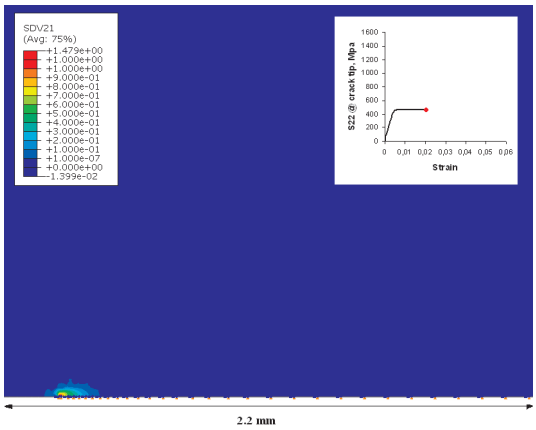

(c) 2kN

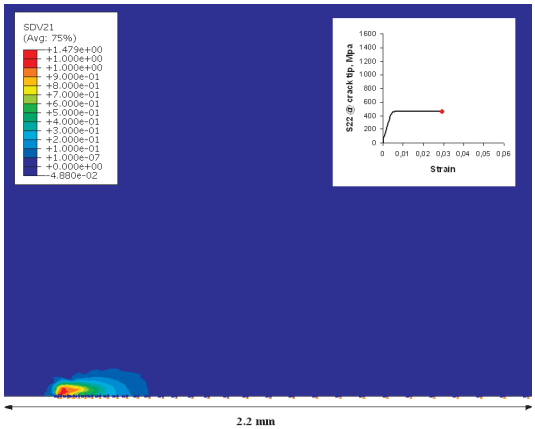

(d) 3kN

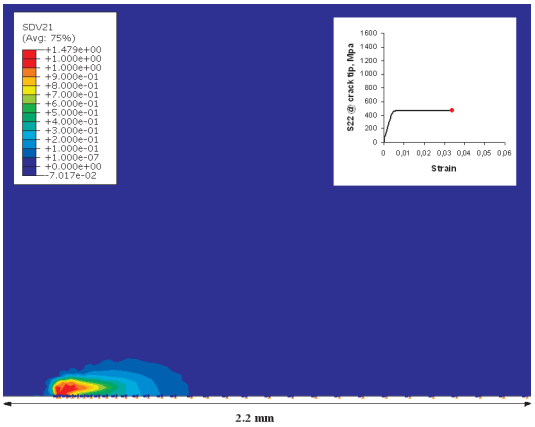

(e) 3.5kN

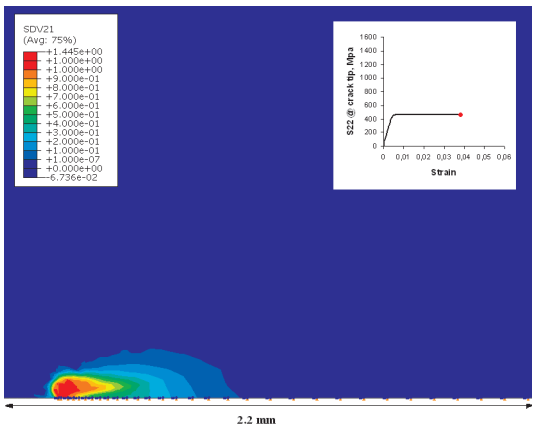

(f) 4kN

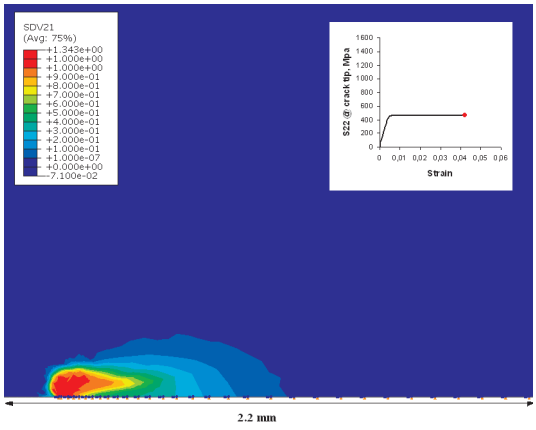

(g) 4.5kN

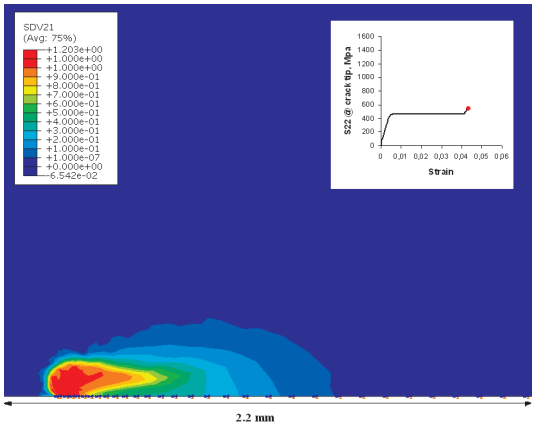

(h) 5kN

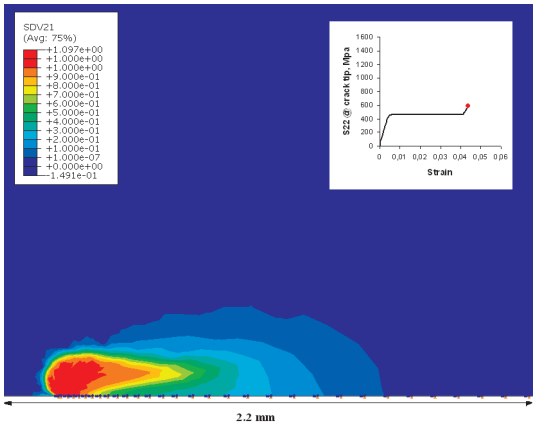

(i) 5.5kN

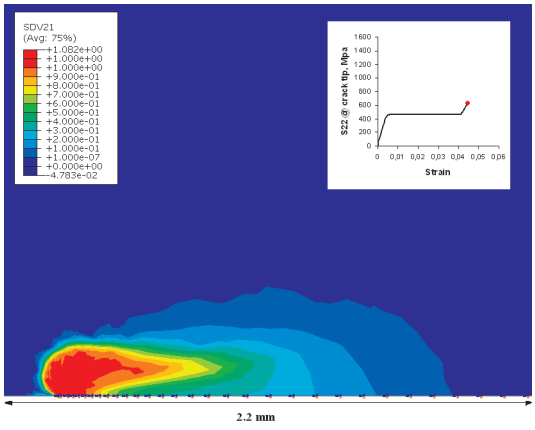

(j) 6kN

Figure 3.5. Phase transformation zones for 2-D edge-cracked Nitinol specimen, $a/W = 0.3$ for different applied loads

The martensite fraction of each region is shown on the upper left side of each Figure. $SDV21$ is the output from UMAT/Nitinol and shows the martensite fraction which changes from 0 to 1. The displayed maximum fraction is higher than 1 because when ABAQUS constructs the contour plot, it extrapolates the values from integration points to the nodes.

A similar study is done for SMA plates with different crack lengths to show the effect of the crack length on martensite transformation. In Figure 3.6 phase transformation zones at the crack tip of plates with different a/W ratios under the tensile load of 8 kN are shown.

It is observed that when the crack length is increased, the stress values at the crack tip increase and this leads to larger transformation regions around the crack tip for the same tensile load. When we compare the transformation zones between the plate with a/W ratio 0.20 and the plate with a/W ratio 0.40, it is seen that the size of the zone in the second one is nearly 4 times of the first one.

The martensite fractions for different crack lengths are displayed along a horizontal path away from the crack tip in Figure 3.7 . The transformation zone lengths are getting larger when the crack length increases under the same applied loading. Fully martensite zone which is indicated by fraction 1 is the largest in plate with crack length 40mm since stress around the crack tip is the highest. The legth of total transformation zone is nearly 7 mm for $a/W = 0.4$ whereas, it is 1.4 mm for $a/W = 0.2$.

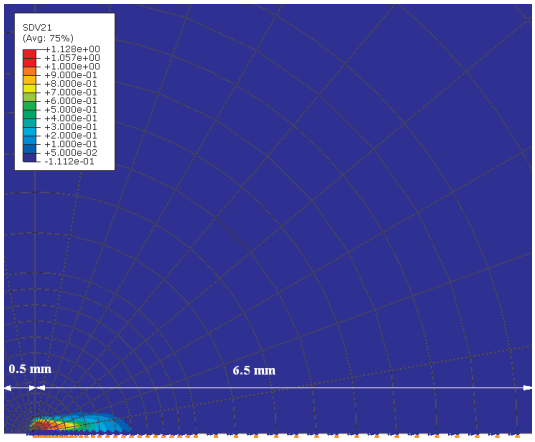

(a) $a/W = 0.20$

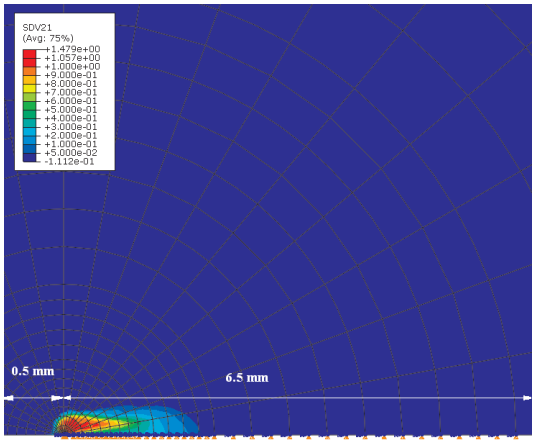

(b) $a/W = 0.25$

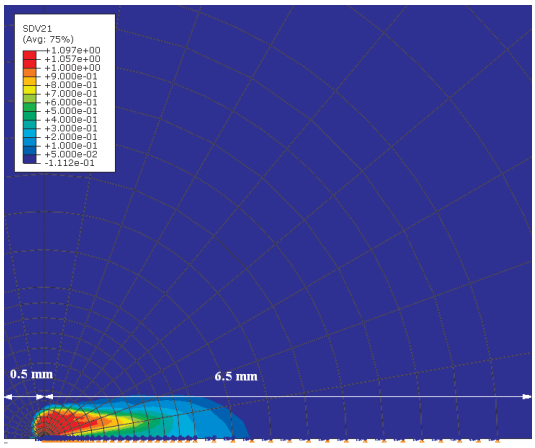

(c) $a/W = 0.30$

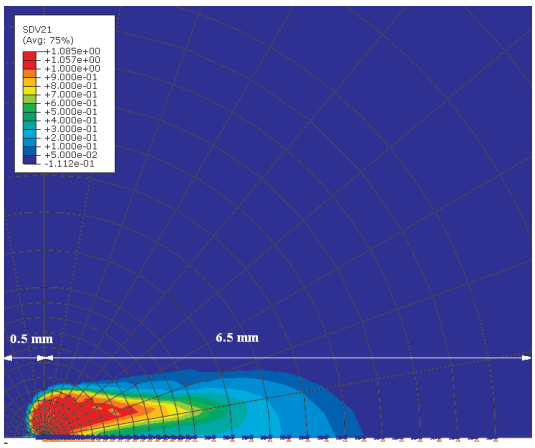

(d) $a/W = 0.35$

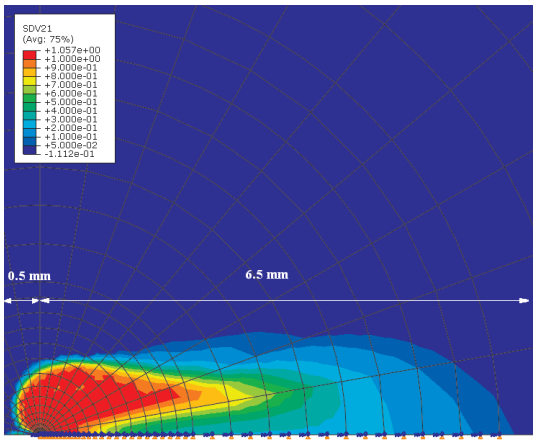

(e) $a/W = 0.40$

Figure 3.6. Phase transformation zones around the crack tip at applied load 8kN for different a/W ratios. The width length, W, is 100 mm for each plate and the crack lengths are a) 20mm, b) 25mm, c) 30mm, d) 35mm, e) 40mm

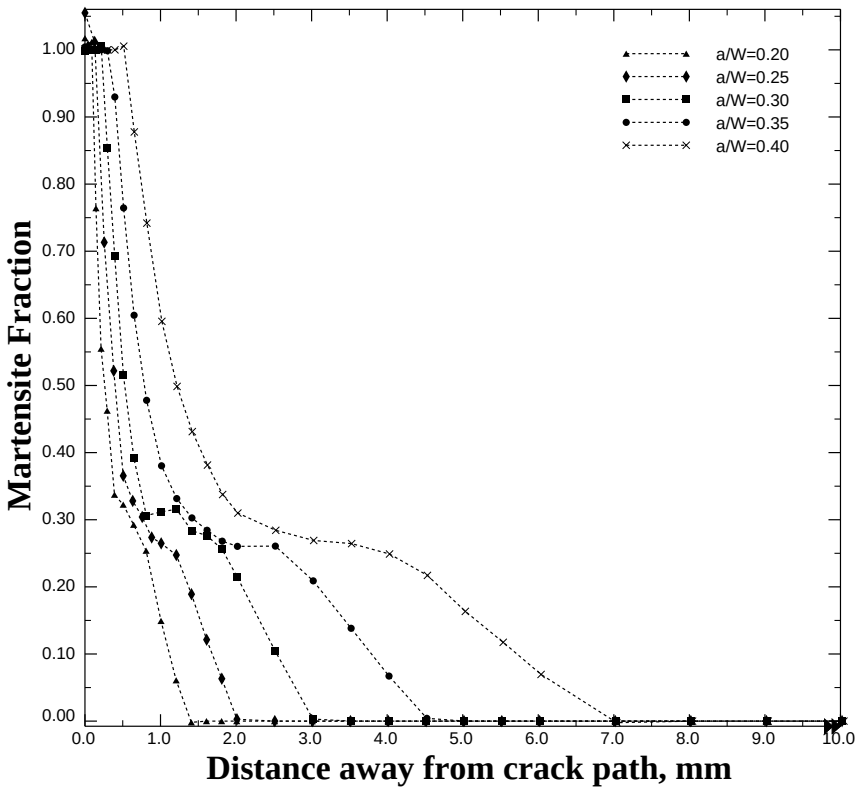

Figure 3.7. Martensite fractions along a path away from the crack tip for different a/W ratios, applied load is 8kN

3.3. Fracture Properties

The utilization of SMAs has been recently increased especially in the area of medicine. As the applications increase, studies focus more on failure mechanism of the material since any unexpected and sudden failure may result in catastrophe. In this section it is aimed to investigate the basic fracture mechanics properties of a 2-D shape memory alloy plate with a single edge crack. The Linear Elastic Fracture Mechanics (LEFM) basics and assumptions are used to analyze the fracture properties.

There are two main approaches in linear fracture which are the energy criterion and the stress intensity approach (See details in Appendix A). LEFM is valid for linear elastic materials and applies the elasticity theory to define the stress field around the crack tip for small strains, for this reason it gives good results for brittle materials. Nevertheless, there are plastic deformation and some other nonlinear effects near the crack tip which makes LEFM inadequate and nonlinear fracture mechanics concept is needed. In some circumstances inelastic region around the crack tip is very small (called small-scale yielding) relative to crack size and the geometry. For this cases LEFM can still provide good approximations.

In this model, it is assumed that there is a small scale transformation near the crack tip and LEFM basics are used. The finite element model which is used in the analysis of a homogenous material is adopted. The validity of the model and its mesh was confirmed in the previous analysis by calculating the stress intensity factors at the crack tip and comparing them with the analytical solutions.

3.3.1. J-Integral

The J-integral values for 2-D edge-cracked Nitinol plate for different a/W ratios calculated by ABAQUS are tabulated in Table 3.2. They are contour dependent for certain contours in front of the crack tip and converge to a value and become contour independent away from the crack tip. This is due to existence of a non-homogenous zone near the crack tip as a result of phase transformation. It is known that in a non-

homogenous medium J-integral is contour dependent. On the other hand, the J-integral values in totally austenite region are contour independent because of the homogeneity. Since the martensite transformation zones are getting bigger under the same applied load when the crack length increases (Figure 3.6), it is required to increase the number of contours to show the contour independency of J-integral in homogenous austenite.

Table 3.2. J-integrals for edge-cracked Nitinol for different a/W ratios and load = 8 kN

J-integral values for Nitinol					
Contour	***a/W* ratios**				
Number	**0.20**	**0.25**	**0.30**	**0.35**	**0.40**
1	10.11	14.96	23.31	35.54	55.51
2	10.06	14.76	23.36	35.49	55.57
3	9.81	14.75	23.29	35.46	55.48
4	9.65	14.96	22.98	35.35	55.42
5	9.78	15.12	22.62	35.02	55.32
6	9.92	15.26	22.27	34.57	54.95
7	10.04	15.38	22.17	34.09	54.39
8	10.15	15.48	22.39	33.69	53.68
9	10.23	15.56	22.63	33.75	52.95
10	10.29	15.63	22.87	34.05	52.37
11	10.34	15.68	23.09	34.35	52.43
12	10.36	15.73	23.26	34.61	52.83
13	10.37	15.76	23.39	34.85	53.19
14	10.37	15.77	23.47	35.08	53.47
15	10.37	15.77	23.55	35.28	53.74
16	10.37	15.77	23.64	35.51	54.20
17	10.37	15.77	23.74	35.72	54.75
18	10.37	15.77	**23.77**	35.87	55.14
19	10.37	15.77	23.77	35.99	55.39
20	10.37	15.77	23.77	36.06	55.59
21	10.37	15.77	23.77	36.09	55.75
22	10.37	15.77	23.77	36.09	55.88
23	10.37	15.77	23.77	36.09	55.99
24	10.37	15.77	23.77	36.09	56.09
25	10.37	15.77	23.77	36.09	56.12
26	10.37	15.77	23.77	36.09	56.12
27	10.37	15.77	23.77	36.09	56.12
28	10.37	15.77	23.77	36.09	56.12
29	10.37	15.77	23.77	36.09	56.12
30	10.37	15.77	23.77	36.09	56.12

The schematic representation of contours used by ABAQUS in the evaluation of J-integrals are shown in Figure 3.8. The Figure displays the phase transformation for $a/W = 0.30$ and load = 8 kN. The elements that belong to the same contour are shaded and the colors of transformation region are left as they are to show the amount of transformation in each contour.

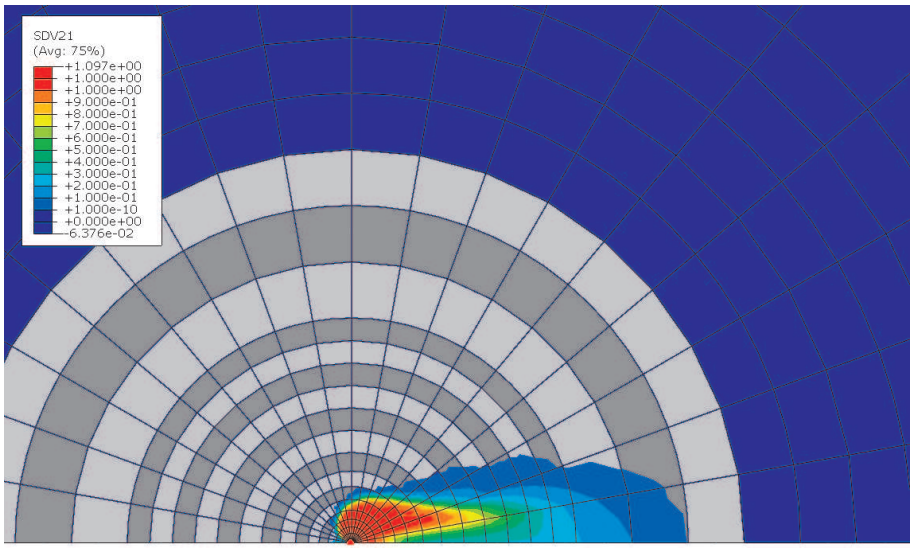

Figure 3.8. Elements used in the corresponding contours. The amount of phase transformation in each contour can be seen, $a/W = 0.30$ and the applied force is 8 kN

In Figure 3.8 the outermost shaded ring is the 18th contour and elements that belong to that contour have no phase transformation. In Table 3.2, J-integral values for $a/W = 0.30$ starting from the 18th contour are constant. This explains that phase transformation leads to inhomogeneity at the crack tip and J-integrals are contour dependent up to full austenite region. Also from outer to inner contour, size of elements decrease and the total martensite fraction in the corresponding contour ring increases. The J-integral values for different a/W ratios are shown in Figure 3.9.

In each graph, the same trend is observed. First the value of the J-integral decreases with increasing contour number, then at a certain contour, the value starts to increase and reaches a constant value. In order to check whether this trend is the result of mesh configuration or the phase transformation, same analyses are performed on a uniformly meshed model with quadratic elements where the element size at the

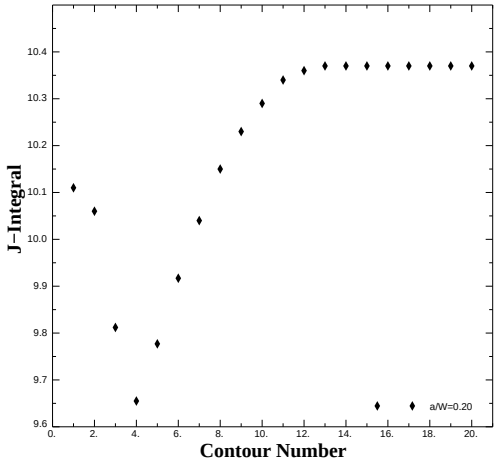

(a) $a/W = 0.20$

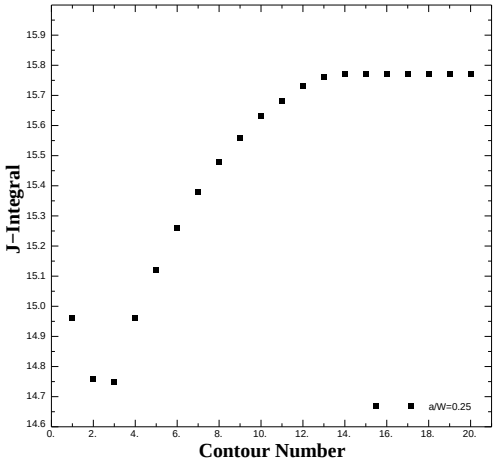

(b) $a/W = 0.25$

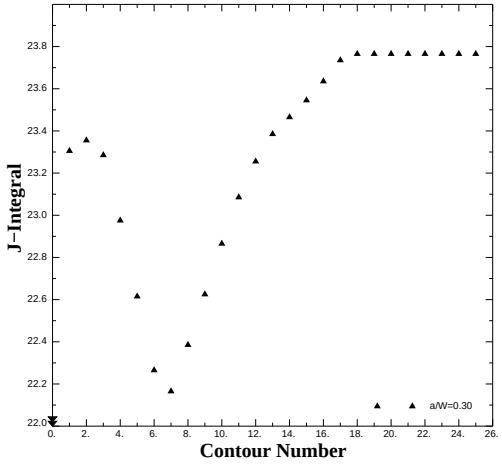

(c) $a/W = 0.30$

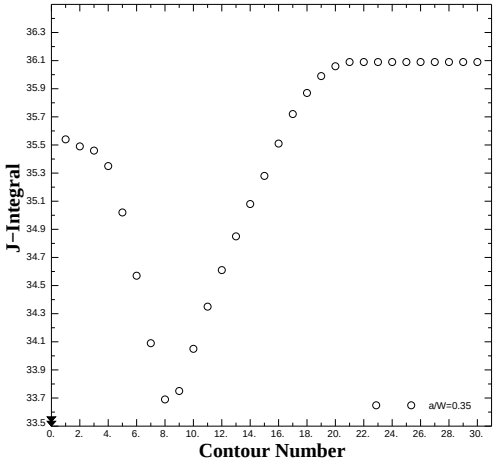

(d) $a/W = 0.35$

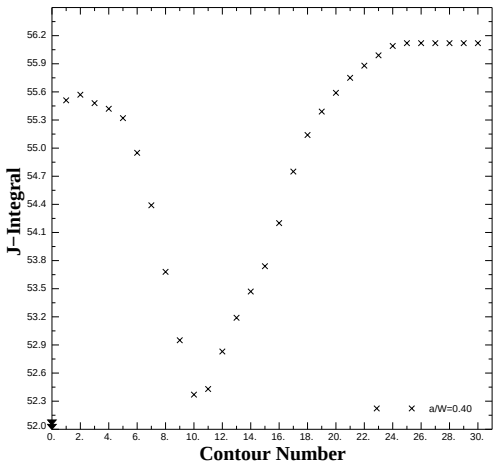

(e) $a/W = 0.40$

Figure 3.9. J-integral values with different a/W ratios and load = 8 kN

crack tip is left the same as in the case of circular mesh. The same trend is observed in the uniformly meshed model as well which shows that this is the result of martensite transformation at the crack tip. The decreasing trend occurs in contours of full martensite region. Since the transformation takes place in front of the crack tip and there is no transformation at the wake region, going away from the crack tip leads to fewer martensite elements in corresponding contour. The increasing trend starts in contours when the martensite transformation begins to decrease. Also, the J-integral converges to a constant value when there is no martensite phase.

3.3.2. Energy Release Rate & Stress Intensity Factor

In Figure 3.9 it is shown that the J-integral values are contour dependent around the crack tip because of the phase transformation and hence they can not be used in stress intensity factor, K_I, calculations. Also ABAQUS does not calculate SIFs when a material user subroutine is used in the analysis. On the other hand, energy release rate of the specimen, G, can be calculated from the strain energy output and can be used to estimate the K_I. Energy release rate is defined as the change of potential energy per unit crack area and has a relationship with stress intensity factor such as $G = \frac{K_I^2}{E}$ for homogenous materials (Appendix A). In the case of nonhomogenous materials the stress intensity factor can be calculated as in homogenous material if the crack-tip experiences nonlinear deformations and the process zones are inside the region dominated by SIFs. Then the energy release rate can be related to stress intensity factor by $G = \frac{K_I^2}{E_{Tip}}$, where E_{Tip} is the Young's modulus for the material at the crack tip [88]. In superelastic Nitinol plate, crack tip becomes martensite at the early stages of loading, and E_{Tip} is set to E_m which is the Young's modulus of martensite. In the material model E_m, is given as 28 Gpa.

Table 3.3. The calculated energy release rates, G, and the stress intensity factors, K_I, computed from the equation $G = \frac{K_I^2}{E_{Tip}}$

K_I **Calculation from ABAQUS**		
a/W	$G \approx \Delta U/\Delta A$	$K_{I(MPA.mm^{1/2})}$
0.20	10.6	545.718
0.25	16.2	673.498
0.30	24.4	826.559
0.35	37.1	1019.215
0.40	58.4	1279.012

It is observed that J-integral values in full austenite region are close to the energy release rate, G, and it will be denoted by J_∞. Thereupon it is considered as $J_\infty = G = \frac{K_I^2}{E_{Tip}}$. Stress intensity factors calculated using constant J-integral values of the austenite region (J_∞) are compared to the ones calculated from energy release rate and tabulated in Table 3.4. In Table 3.4, ND stands for non-dimensionalized and the

Table 3.4. K_I obtained from constant J-Integral value at the austenite region, J_∞, vs K_I from the energy release rate, $G \approx \frac{\Delta U}{\Delta A}$

a/W	J_∞	K_I^∞	ND K_I^{aust}	$G \approx \frac{\Delta U}{\Delta A}$	K_I^G	ND K_I^G
0.20	10.37	538.85	1.506	10.64	545.718	1.525
0.25	15.77	66.50	1.661	16.20	673.498	1.683
0.30	23.77	815.82	1.861	24.40	826.559	1.886
0.35	36.09	1005.24	2.123	37.10	1019.215	2.153
0.40	56.12	1253.53	2.477	58.42	1279.012	2.528

SIFs are divided by $\sqrt{a}.P$ in order to make them non-dimensionalized. The ND SIFs are illustrated in Figure 3.10 and the percent errors are shown in Table 3.5. Since the values are very close to the ones calculated from J_∞ values and error percent is below 2 %, the equality $J_\infty = G$ can be used to calculate the stress intensity factors in SMAs.

Table 3.5. Non-dimensionalized stress intensity factors, K_I, calculated from J_∞ and from energy release rate and the corresponding percent errors

ND K_I^∞	ND K_I^G	error %
1.51	1.53	1.26
1.66	1.68	1.34
1.86	1.89	1.30
2.12	2.15	1.37
2.48	2.53	1.99

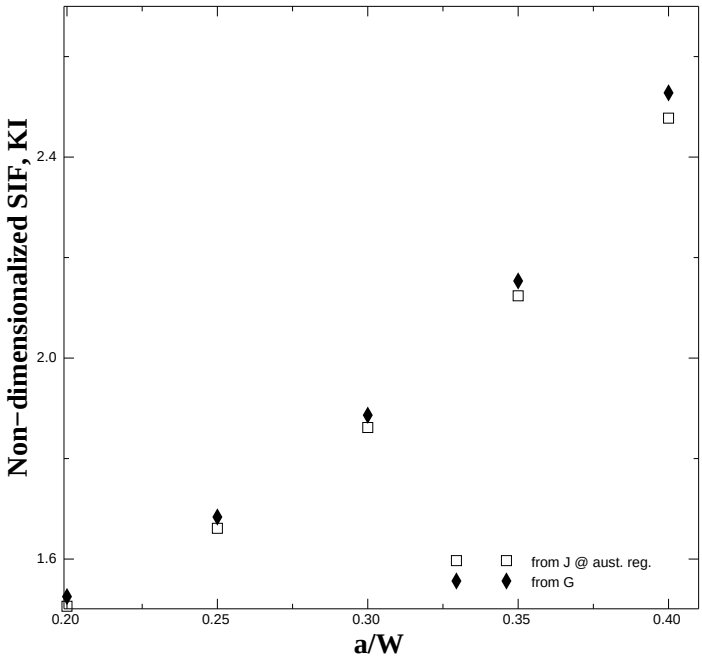

Figure 3.10. The non-dimensionalized SIFs obtained from constant J-integrals in the austenite region, J_∞, and SIF's calculated from the energy release rate, $G \approx \frac{\Delta U}{\Delta A}$

The accuracy of the technique to calculate the stress intensity factors will be discussed in Section 3.5.

3.3.3. Discussion on Energy Stored

The external work done on an elastic body leads to deformation. If there is no energy lost in the form of heat, the external work is converted into strain energy. It can also be defined as the mechanical energy stored in stressed materials. The elastic strain energy caused by elastic deformation is mostly recoverable. Total internal energy is consists of elastic strain energy plus the energy dissipated through plastic deformation and crack growth.

$$E = U^e + U^p \tag{3.1}$$

One can get the energy stored using ABAQUS through following commands [84]:

- ALLSE: Elastic Strain energy for the whole model.
- ALLPD: Energy dissipated by plastic deformation for the whole model.
- ALLIE: Total strain energy for the whole model.

  ALLIE=ALLSE + ALLPD
- ALLKE: Kinetic Energy for the whole model.
- ALLWK: External work for the whole model.
- ETOTAL: Total Energy for the whole model.

  ETOTAL=ALLKE+ALLIE−ALLWK

In the analysis of edge cracked Nitinol plate, ALLSE gives the total elastic strain energy and ALLPD gives the transformation strain energy for the whole model. The UMAT/Nitinol provides elastic and transformation strain energies not only for the whole model but also for a single element and for integration points. SENER is the output for elastic strain energy and PENER is the output for transformation strain energy at integration points. Similarly, ELSE gives the elastic strain energy and ELDP gives the transformation strain energy for single element. Since static loading is applied ALLKE gives zero output. The energy values vs time graphics are presented in Figure 3.11 for the edge-cracked Nitinol plate with $a/W = 0.30$ under 80 MPa tensile loading.

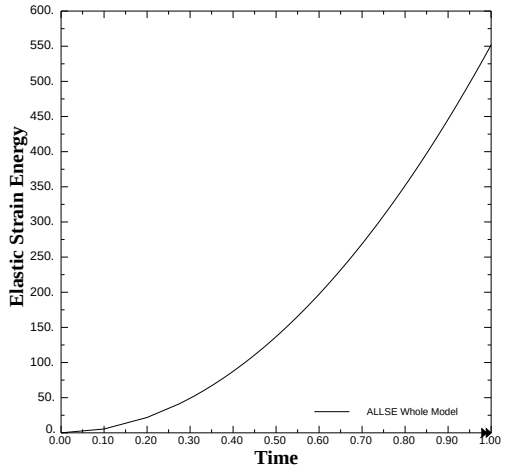

(a) Elastic strain energy

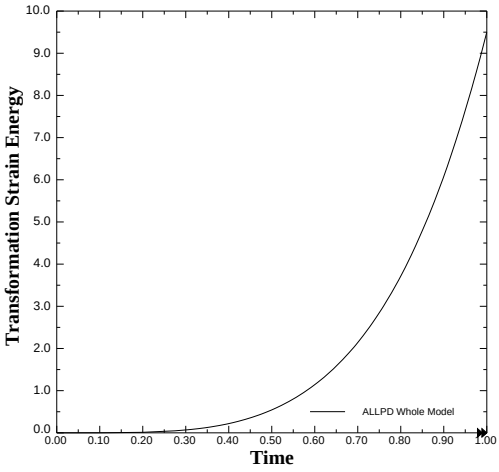

(b) Transformation strain energy

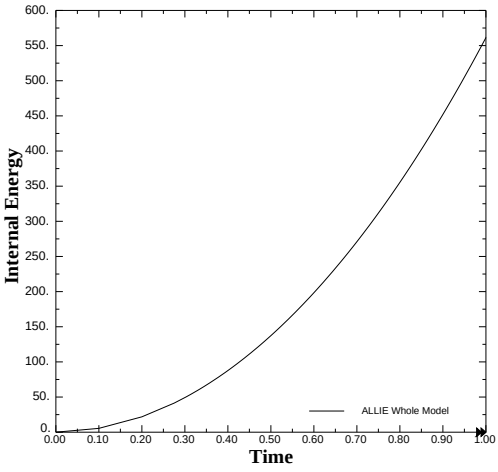

(c) Internal energy

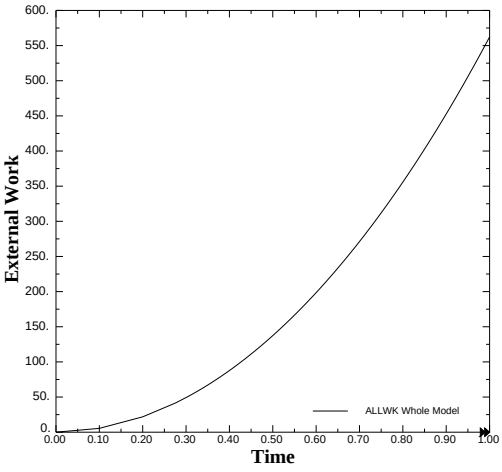

(d) External work

Figure 3.11. Energy stored calculated by ABAQUS for the edge-cracked Nitinol plate with $a/W = 0.30$ under 80 MPa tensile loading. The values are for the half plate. For whole plate all the values must be multiplied by 2

The energy plots in Figure 3.11 are values for the whole model. The elastic strain energy is strictly increasing until the end of loading whereas the transformation strain energy is zero at the beginning because there is only elastic deformation and no phase transformation. When the transformation occurs, the transformation strain energy starts to increase as can be seen from Figure 3.11(b). For the model (half plate, $a/W = 0.30$, tensile load= 80 MPa), the transformation strain energy which is 9.49982 mJ is not very much relative to elastic strain energy, 551.733 mJ since there is a small scale transformation at the crack tip which contributes little to total internal energy. In Figure 3.12, elastic and transformation strain energies and internal energy which is the sum of the former ones are displayed.

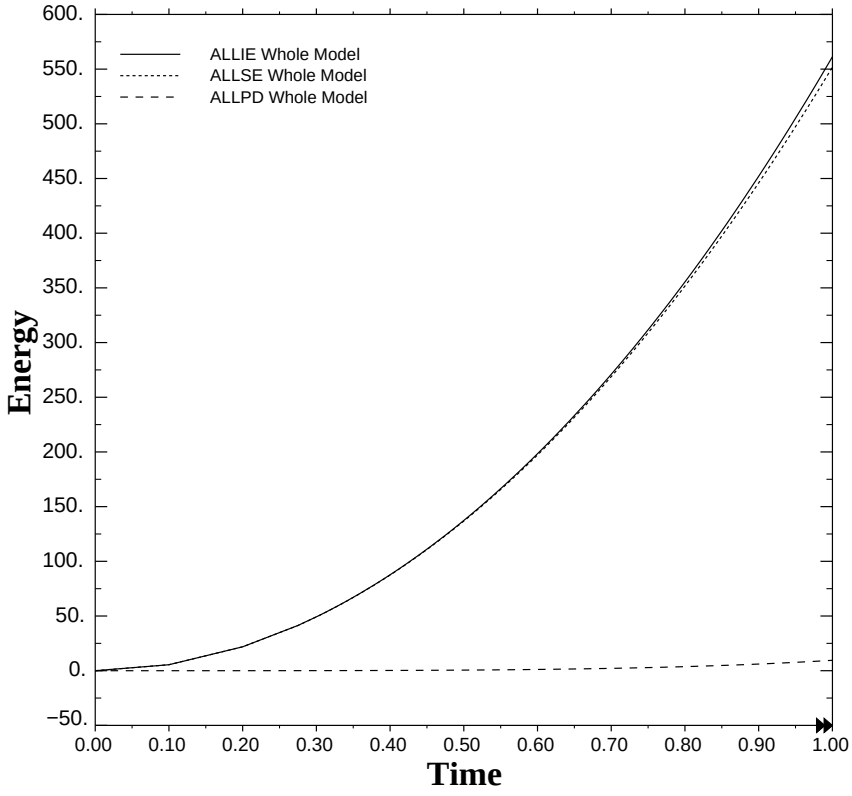

Figure 3.12. Comparison of energy values displayed in Figure 3.11

In Figure 3.13 the elastic and transformation strain energies of a single element near the crack tip which is totaly transformed into martensite at the end of loading are displayed. In the elastic strain energy curve, the trend of increase changes at 25% and at 70% of total time which correspond to the starting times of martensite transformation and the elastic deformation in martensite respectively. The transformation strain

energy curve remains zero up to 25% of the total time, then it begins to increase with the start of martensite transformation. Around the 70% of total time it becomes constant since the martensite transformation is completed at the corresponding element.

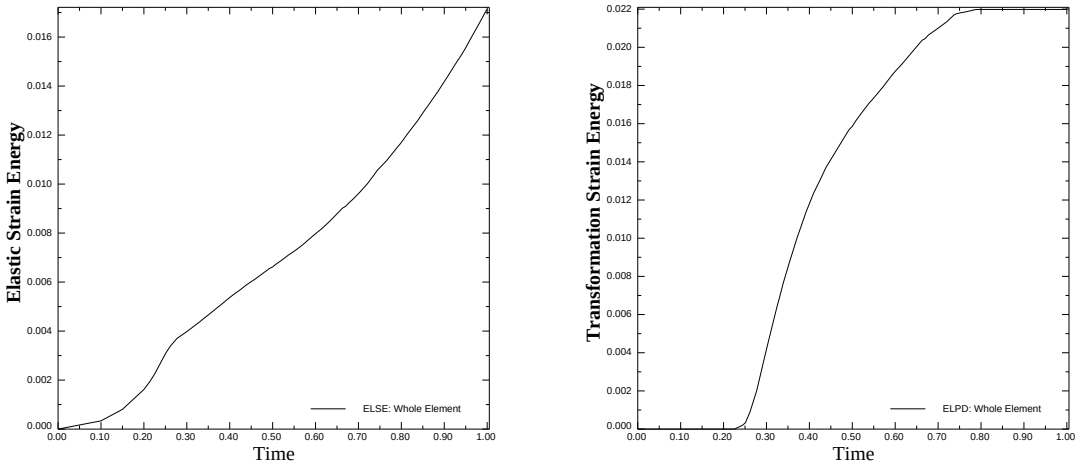

(a) Elastic strain energy (b) Transformation strain energy

Figure 3.13. Energy stored calculated for a single element near the crack tip, $a/W = 0.30$, under 80 MPa tensile loading

In addition, the whole elastic and transformation strain energy values for the edge-cracked Nitinol plate with $a/W = 0.30$ subjected to 80 MPa tensile loading and subsequent unloading are shown in Figure 3.14. The elastic strain energy is recovered upon unloading. When we look at the transformation strain curve (Figure 3.14(b)), it is observed that energy begins to increase as the transformation starts and increases until the end of loading. Then it stays constant for a while at the beginning of unloading because of the fact that first the elastic energy recovers and then the reverse transformation initiates. Notice that the transformation strain energy is not zero at the end of unloading. This may be the result of residual stresses occuring at the crack tip.

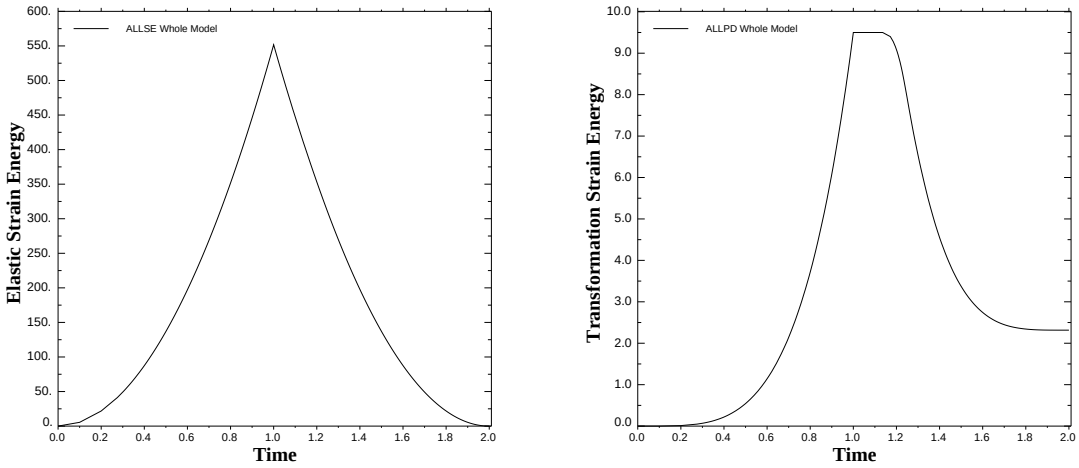

(a) Elastic strain energy (b) Transformation strain energy

Figure 3.14. Energy stored calculated for loading-unloading analysis of the edge-cracked Nitinol plate with $a/W = 0.30$ under 80 MPa load

3.4. Parametric Study of the Effect of Material Properties

In order to see the effects of any change in the material parameters on phase transformation and on fracture mechanics properties of Nitinol, similar analyses are performed by changing one specific material property at a time. Variation in material properties are shown on stress-strain diagrams in Figure 3.15. Case I is the main analysis performed in previous section, in case II, only the starting and ending values of stress of transformation in loading are increased from $400 - 410$ Mpa to $500 - 510$ Mpa; in case III, transformation strain is decreased to its half, from 0.04 to 0.02 and in case IV, the entire hysteresis loop is shifted upwards by 200 Mpa. In each case the 2-D Nitinol plate with $a/W = 0.30$ is subjected to 8 kN tensile loading. First, the size and the shape of the phase transformation zones are studied.

In case II, phase transformation starts later when compared to case I. In Figure 3.16, under the same tensile loading the shapes of the transformation zones are similar but the size of the zone for the second one is smaller than the first one. An increase in the value of transformation starting stress delays the phase transformation as expected and the size of the total transformation zone is reduced from 3mm to 2.1mm. In case III, halving the transformation strain leads to a change in both the size and the shape

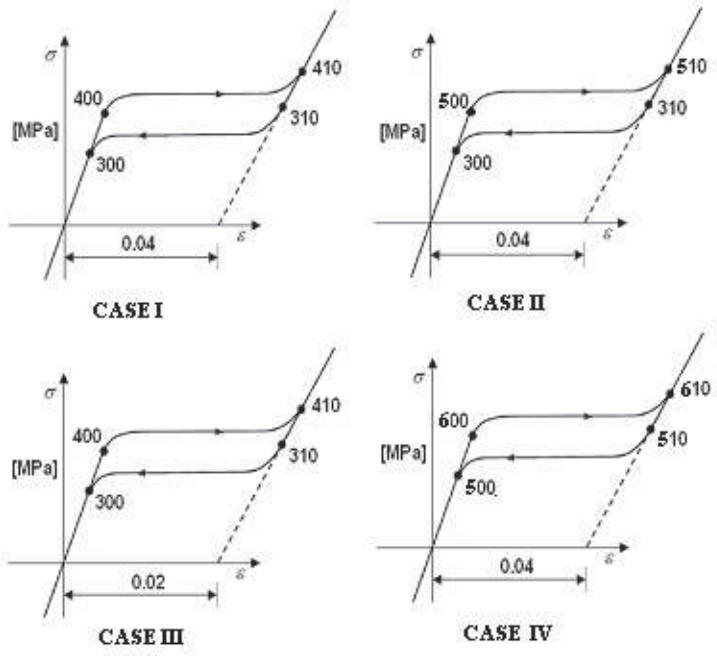

Figure 3.15. Schematic representation of stress-strain curves for materials used to study the effect of material parameters

of the transformation zone. The transformation zone has a tend to progress away from the crack tip horizontally in the first two cases. However in case III, transformation zone grows in the vertical direction. Decreasing transformation strain increases the height of the transformation zone. In case IV, the hysteresis loop is shifted upward by 200MPA, and as a result the transformation starting stress increased and the size of the zone decreased.

Next, for each case, J-integrals are calculated and the results are tabulated in Table 3.6. A similar trend is observed for each case: There is a non-homogenous zone around the crack tip as a result of phase transformation, and J-integrals are contour dependent around the crack tip. They become contour independent away from the crack tip because there is no transformation and only austenite phase is present.

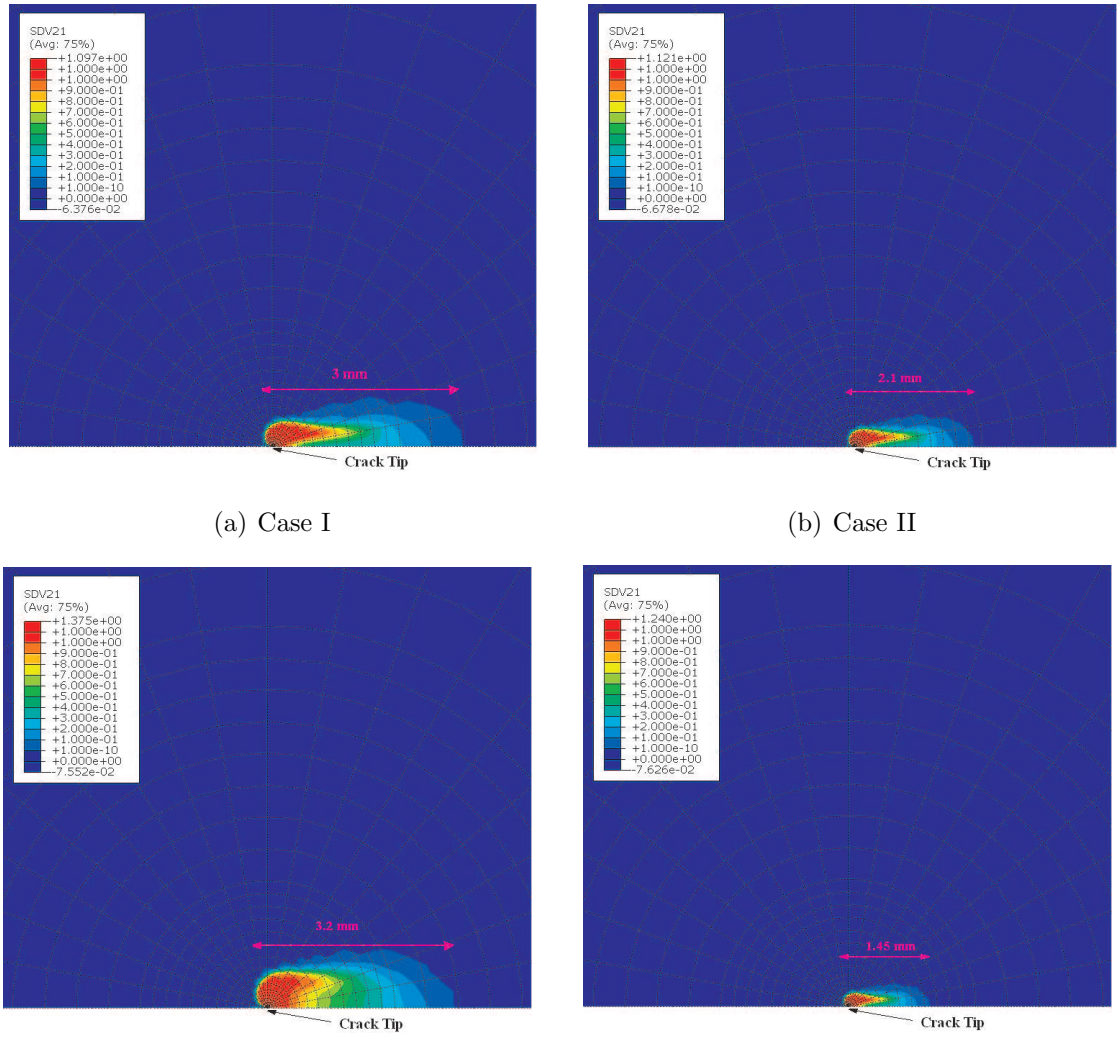

(a) Case I

(b) Case II

(c) Case III

(d) Case VI

Figure 3.16. Phase transformation zones around the crack tip for four cases studied. In all cases applied load is 8 kN and $a/W = 0.30$

Table 3.6. J-integral values for different crack lengths (In all cases, load = 8 kN)

J-integral values for a/W=0.20				
Contour #	case I	case II	case III	case IV
1	10.11	9.87	10.08	9.72
2	10.06	9.70	10.02	9.42
3	9.81	9.44	9.81	9.37
4	9.66	9.58	9.53	9.63
5	9.78	9.77	9.41	9.85
6	9.92	9.93	9.59	9.99
7	10.04	10.05	9.79	10.10
8	10.15	10.14	9.97	10.16
9	10.23	10.21	10.10	10.16
10	10.29	10.23	10.22	10.16
11	10.34	10.23	10.29	10.17
12	10.36	10.23	10.33	10.17
13	10.37	10.23	10.33	10.17
14	10.37	10.23	10.33	10.17
15	10.37	10.23	10.33	10.17
16	10.37	10.23	10.33	10.17
17	10.37	10.23	10.33	10.17
18	10.37	10.23	10.33	10.17
19	10.37	10.23	10.33	10.17
20	10.37	10.23	10.33	10.17

J-integral values for a/W=0.25				
Contour #	case I	case II	case III	case IV
1	14.96	14.79	15.06	14.37
2	14.76	14.29	14.77	14.23
3	14.75	14.58	14.33	14.67
4	14.96	14.87	14.37	14.96
5	15.12	15.09	14.67	15.14
6	15.26	15.22	14.90	15.25
7	15.38	15.31	15.08	15.31
8	15.48	15.38	15.22	15.33
9	15.56	15.44	15.35	15.33
10	15.63	15.47	15.48	15.33
11	15.68	15.48	15.58	15.33
12	15.73	15.48	15.65	15.33
13	15.76	15.48	15.69	15.33
14	15.77	15.48	15.69	15.33
15	15.77	15.48	15.69	15.33
16	15.77	15.48	15.69	15.33
17	15.77	15.48	15.69	15.33
18	15.77	15.48	15.69	15.33
19	15.77	15.48	15.69	15.33
20	15.77	15.48	15.69	15.33

J-integral values for a/W=0.30				
Contour #	case I	case II	case III	case IV
1	22.31	22.61	23.10	22.14
2	23.36	22.67	23.09	22.11
3	23.29	22.35	23.03	21.59
4	22.98	21.88	22.85	20.99
5	22.62	21.41	22.50	20.96
6	22.27	21.44	22.05	21.38
7	22.17	21.77	21.64	21.76
8	22.39	22.07	21.46	22.11
9	22.63	22.34	21.76	22.39
10	22.87	22.62	22.18	22.59
11	23.09	22.81	22.52	22.74
12	23.26	22.93	22.78	22.80
13	23.39	23.03	22.97	22.81
14	23.47	23.10	23.13	22.81
15	23.55	23.13	23.26	22.81
16	23.64	23.13	23.43	22.81
17	23.74	23.13	23.57	22.81
18	23.77	23.13	23.60	22.81
19	23.77	23.13	23.60	22.81
20	23.77	23.13	23.60	22.81
21	23.77	23.13	23.60	22.81
22	23.77	23.13	23.60	22.81
23	23.77	23.13	23.60	22.81
24	23.77	23.13	23.60	22.81
25	23.77	23.13	23.60	22.81
26	23.77	23.13	23.60	22.81
27	23.77	23.13	23.60	22.81
28	23.77	23.13	23.60	22.81
29	23.77	23.13	23.60	22.81
30	23.77	23.13	23.60	22.81

J-integral values for a/W=0.35				
Contour #	case I	case II	case III	case IV
1	35.54	34.10	35.03	33.21
2	35.49	34.09	34.98	33.31
3	35.46	33.96	34.92	32.91
4	35.35	33.53	34.85	32.18
5	35.02	32.92	34.65	31.36
6	34.57	32.25	34.27	31.03
7	34.09	31.96	33.74	31.51
8	33.69	32.30	33.09	32.04
9	33.75	32.73	32.62	32.51
10	34.05	33.13	32.50	32.99
11	34.35	33.49	32.94	33.34
12	34.61	33.81	33.42	33.56
13	34.85	34.04	33.81	33.73
14	35.08	34.20	34.13	33.84
15	35.28	34.32	34.40	33.91
16	35.51	34.48	34.75	33.91
17	35.72	34.62	35.12	33.91
18	35.87	34.63	35.39	33.91
19	35.99	34.63	35.57	33.91
20	36.06	34.63	35.67	33.91
21	36.09	34.63	35.68	33.92
22	36.09	34.63	35.68	33.92
23	36.09	34.63	35.68	33.92
24	36.09	34.63	35.68	33.92
25	36.09	34.63	35.68	33.92
26	36.09	34.63	35.68	33.92
27	36.09	34.63	35.68	33.92
28	36.09	34.63	35.68	33.92
29	36.09	34.63	35.68	33.92
30	36.09	34.63	35.68	33.92

Table 3.6. (continued) J-integral values for different crack lengths (In all cases, load = 8 kN)

J-integral values for a/W=0.40				
Contour #	**case I**	**case II**	**case III**	**case IV**
1	55.51	51.77	54.01	49.99
2	55.57	51.72	54.14	49.95
3	55.48	51.69	54.06	49.50
4	55.42	51.55	53.99	49.27
5	55.32	51.08	53.91	48.27
6	54.95	50.39	53.73	47.45
7	54.39	49.52	53.33	46.69
8	53.68	48.74	52.72	46.86
9	52.95	48.63	51.90	47.63
10	52.37	49.19	51.00	48.33
11	52.43	49.76	50.40	48.92
12	52.83	50.20	50.13	49.46
13	53.19	50.60	50.39	49.89
14	53.47	50.98	50.91	50.18
15	53.74	51.32	51.43	50.41
16	54.20	51.73	52.18	50.69
17	54.75	52.10	52.97	50.93
18	55.14	52.36	53.54	50.96
19	55.39	52.54	53.97	50.96
20	55.59	52.62	54.32	50.96
21	55.75	52.62	54.60	50.96
22	55.88	52.62	54.81	50.96
23	55.99	52.62	54.98	50.96
24	56.09	52.62	55.08	50.96
25	56.12	52.62	55.09	50.96
26	56.12	52.62	55.09	50.96
27	56.12	52.62	55.09	50.96
28	56.12	52.62	55.09	50.96
29	56.12	52.62	55.09	50.96
30	56.12	52.62	55.09	50.96

Tabulated values of J-integral are plotted in Figure 3.17. The pattern of the curves in each case is similar. For case III, transformation strain is half of case I, and this leads to a shift in curve to lower-right. In cases II and IV, changes on material properties delayed the martensitic transformation, thus J-integral curves are nearly the same but they are shifted downward.

The energy release rates, $\frac{\Delta U}{\Delta A}$, are calculated for different crack lengths for each case. Mode-I stress intensity factors are computed assuming that from $G \approx \frac{\Delta U}{\Delta A}$. Results are tabulated in Table 3.7

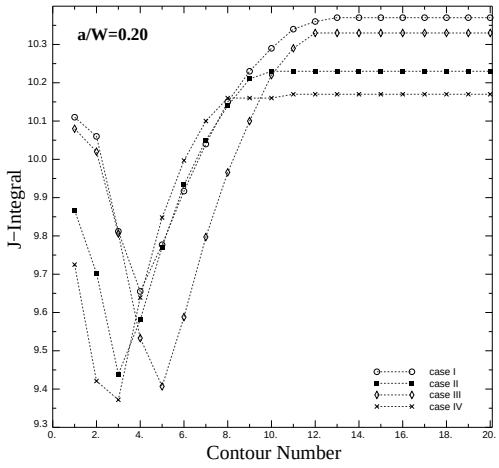

(a) $a/W = 0.20$

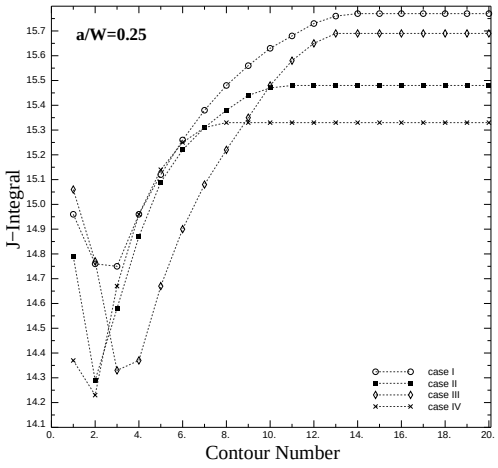

(b) $a/W = 0.25$

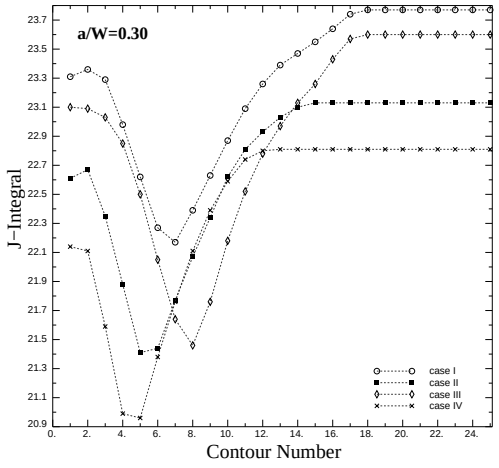

(c) $a/W = 0.30$

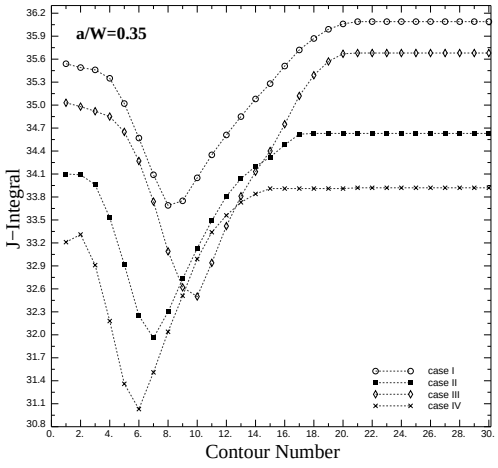

(d) $a/W = 0.35$

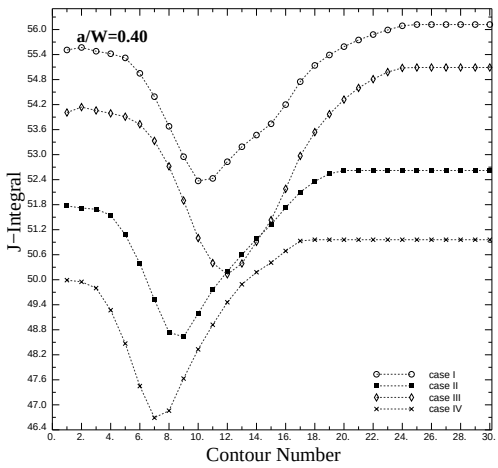

(e) $a/W = 0.40$

Figure 3.17. J-Integral values in all cases for different crack lengths, load = 8 kN.

Table 3.7. The constant J-integral values in austenitic region, J_∞, calculated energy release rates, $G \approx \frac{\Delta U}{\Delta A}$, and stress intensity factors, K_I. For each cases load = 8kN.

	a/W	J_∞	$\frac{\Delta U}{\Delta A}$	$\mathbf{K_I^G}$
C	0.20	10.37	10.64	545.718
A	0.25	15.77	16.20	673.498
S	0.30	23.77	24.40	826.559
E	0.35	36.09	37.10	1019.215
1	0.40	56.12	58.42	1279.012

	a/W	J_∞	$\frac{\Delta U}{\Delta A}$	$\mathbf{K_I^G}$
C	0.20	10.24	10.50	542.218
A	0.25	15.48	15.93	667.904
S	0.30	23.13	23.73	815.098
E	0.35	34.63	35.62	998.623
2	0.40	52.62	54.38	1233.908

	a/W	J_∞	$\frac{\Delta U}{\Delta A}$	$\mathbf{K_I^G}$
C	0.20	10.33	10.63	545.615
A	0.25	15.69	16.19	673.249
S	0.30	23.60	24.38	826.152
E	0.35	35.68	37.19	1020.369
3	0.40	55.09	58.01	1274.494

	a/W	J_∞	$\frac{\Delta U}{\Delta A}$	$\mathbf{K_I^G}$
C	0.20	10.17	10.43	540.459
A	0.25	15.33	15.81	665.300
S	0.30	22.81	23.39	809.371
E	0.35	33.92	34.87	988.138
4	0.40	50.96	52.50	1212.436

3.5. A Closed Form Solution of Mode-I Stress Intensity Factor in Nitinol Shape Memory Alloy

The effect of stress-induced phase transformation on crack tip stress intensity factor (SIF) and on toughness of shape memory alloys is a phenomenon that is not fully understood and has recently become a focus of attention. There are only few studies on this subject. Birman [73], Yi and Gao [76, 77], Yan et al. [78] and Xiong and Liu [80] are the authors who have recently studied the calculation of stress intensity factors at crack tip in SMAs. According Birman [73], the effect of phase transformation on stress intensity is relatively small and it is suggested that the magnitude of the stress intensity factor may be evaluated based on the properties of austenite. Yi and Gao [76, 77] noted that martensitic transformation reduces crack tip stress intensity and increases the toughness of SMAs and temperature has an important role on toughening process. On the contrary, Yan et al. [78] and Xiong and Liu [80] stated that phase transformation leads to volume contraction at the crack tip and as a result of volume contraction, stress intensity factor increases, and toughness decreases.

Previous studies tried to find a way to calculate SIFs. In the study of Xiong and Liu [80], the effect of phase transformation on crack tip stress intensity factor in a Ni-MN-Ga shape memory alloy is investigated and a closed form solution for crack tip stress intensity factor calculation is developed. They have stated that the stress intensity factor of the crack tip, K_I^* consists of two parts, one due to externally applied load, K_I, and the other due to phase transformation around the crack tip, K_{tr}:

$$K_I^* = K_I + K_{tr} \tag{3.2}$$

If $K_{tr} > 0$, the phase transformation leads to an increase in crack tip of SIF, and to a decrease if $K_{tr} < 0$. In SMAs, when transformation begins, stress induced martensite is surrounded by an untransformed region of austenite at the crack tip. According to previous studies, stress induced martensitic transformation produces an extra tensile stress field around crack tip which results in a negative volume change in the case of Nitinol. The volume contraction is indicated as 0.5% in the studies of Jackson et al.

[89] and Jacobus et al. [90] and 0.39% by Yan et al.[78] and Holtz et al. [91]. For most SMAs, there is a volume contraction and as a result K_{tr} is positive. This causes an increase in crack tip SIF, K_I^*.

According to the elastic-plastic fracture mechanics, there is some inelasticity in the form of plasticity, creep or phase change around the crack tip under external tensile stress. The local stress field around the crack tip can be calculated from Linear Elastic Fracture Mechanics (LEFM) theory using stress intensity factors. Applied loading, crack length and geometrical configuration of cracked bodies influence the strength of these fields [92].

There is an asymptotic field, called D as shown in Figure 3.18, which is limited to a very small region around crack tip and stress singularity dominates inside this region [92]. There is a smaller region inside D, represented by R, which shows the inelastic deformation. If R is very small compared to D and crack length, LEFM can be used. This is called "small-scale yielding".

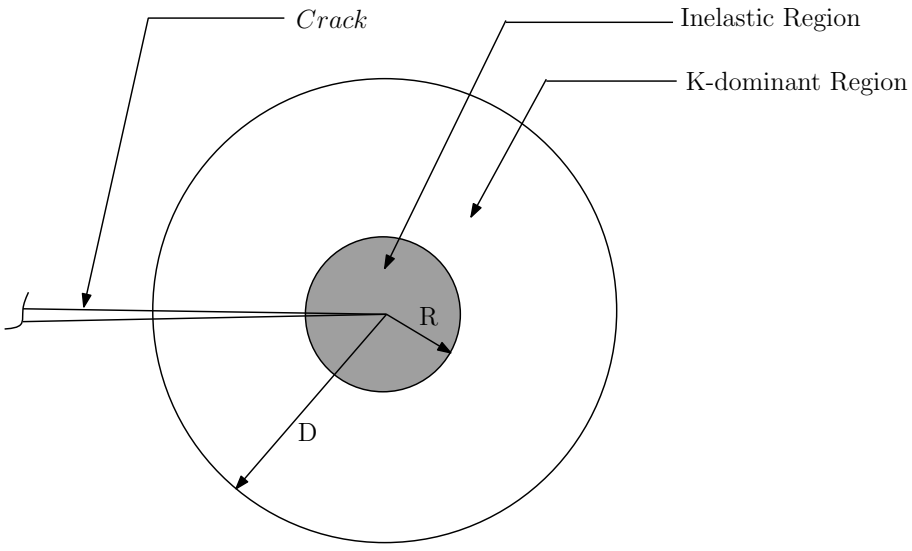

Figure 3.18. K-dominant and inelastic regions around the crack tip [92]

In that region, in a linearly elastic material stresses can be calculated on the crack plane, $\theta = 0$ as;

$$\sigma = \sigma_{xx} = \sigma_{yy} = \frac{K_I^0}{\sqrt{2\pi r}} \tag{3.3}$$

For plane stress conditions, yielding occurs when $\sigma = \sigma_Y$ and the stress in the plastic zone is confined to yield strength σ_Y. If we substitute σ by σ_Y in Equation 3.3 and solve for r, we have a first order approximation for the plastic zone size;

$$r_p^1 = \frac{1}{2\pi}\left(\frac{K_I^0}{\sigma_Y}\right)^2 \tag{3.4}$$

where

$$K_I^0 = \sigma_0\sqrt{\pi a} \tag{3.5}$$

Equation 3.4 gives the first order estimation of Irwin [93] to the plastic zone radius but this is inaccurate because stress redistribution is required when yielding occurs to satisfy equilibrium. The stress in the shaded area in Figure 3.19 cannot be carried in an elastic-plastic material since the stress can not exceed the yield stress and stresses must be redistributed to satisfy the equilibrium. Thus, the actual plastic zone length must be larger than r_p^1 [80].

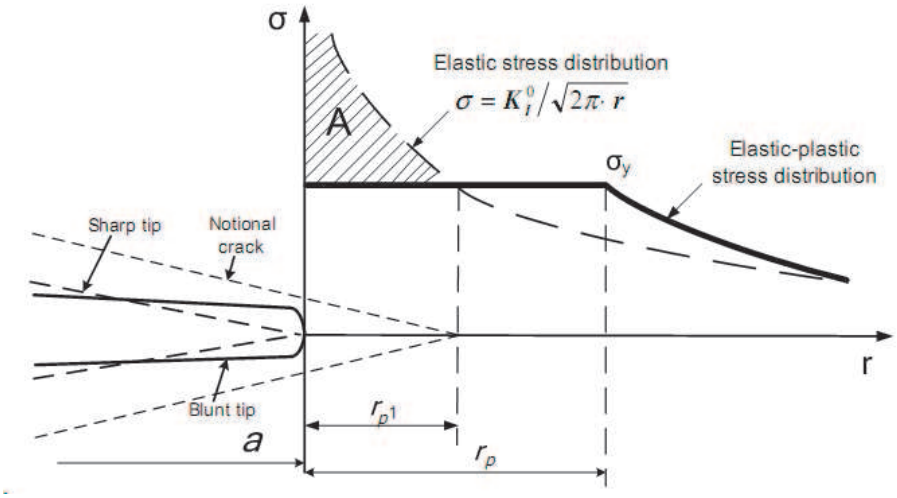

Figure 3.19. Illustration of elastic-plastic stress redistribution according to Irwin's second order estimate [80]

The second order estimation of Irwin to plastic zone is calculated from the force balance equation as shown below:

$$\sigma_Y r_p = \int_0^{r_p^1} \sigma dr = \int_0^{r_p^1} \frac{K_I^0}{\sqrt{2\pi r}} dr \tag{3.6}$$

Integrating Equation 4.5 and solving for r_p gives the following result:

$$r_p = \frac{1}{\pi} \left(\frac{K_I^0}{\sigma_Y} \right)^2 \tag{3.7}$$

which is twice the first order estimation, r_p^1.

For a central crack of length 2a in an infinite plate subjected to uniaxial stress σ_0, the new crack length, called the effective crack, a_{eff}, is the sum of the actual crack length and the length of plastic zone according to the correction of Irwin's model:

$$a_{eff} = 2(a + \frac{r_p}{2}) \quad . \tag{3.8}$$

Further, the stress intensity factor corresponding to the effective crack length is the effective SIF, K_{eff}, and it is given for plane stress by:

$$K_{eff} = \sigma_0[\pi(a + \frac{r_p}{2})]^{1/2} \quad . \tag{3.9}$$

For simplicity K_{eff} will be referred to as K_I in the following equations. If the half of the crack length is much larger than the plastic zone (i.e. $a >> r_p$), then $K_I \approx K_I^0$. Therefore,

$$K_I = \sigma_0[\pi(a + \frac{r_p}{2})]^{1/2} \quad , \tag{3.10}$$

$$r_p = \frac{1}{\pi}\left(\frac{K_I}{\sigma_Y}\right)^2 = \frac{\sigma_0^2\left(a+\frac{r_p}{2}\right)}{\sigma_y^2} \tag{3.11}$$

$$\Rightarrow \quad r_p = \frac{2\sigma_0^2}{2\sigma_y^2 - \sigma_0^2}a \tag{3.12}$$

By combining Equation 3.10 and Equation 3.12, K_I can be expressed as a function of σ_0;

$$K_I = \sigma_0\sqrt{\frac{2\pi.a.\sigma_y^2}{2\sigma_y^2 - \sigma_0^2}} \quad . \tag{3.13}$$

The stress field in K dominant zone will be given by:

$$\sigma = \begin{cases} \sigma_Y & r < r_p \\ \frac{K_I}{\left(2\pi.(r-\frac{r_p}{2})\right)^{1/2}} & r \geq r_{\mathrm{p}} \end{cases} \tag{3.14}$$

where r is the distance from the crack tip.

In the case of an SMA, the area around the crack tip can be divided into four regions as shown in Figure 3.20. In region I, martensite is plastically deformed, in region II there is elastically deformed martensite, in region III stress induced martensite and austenite coexist and in region IV, there is untransformed austenite. The length of the corresponding regions are: r_p is the length of the plastic region in fully martensitic zone, r_m is the total length of fully martensitic zone and r_{tr} is the length of the whole transformation zone.

In Figure 3.20, the curve with dashed line is the stress curve at the crack tip for an elastic-plastic material while the piecewise curve $a-b-c-d-e$ is the stress curve around the crack tip of an SMA. In region I, the stress is constant and equal to σ_Y of stress induced mastensite; whereas in region III, it is constant again and equal to σ_{crit}^{SIM} which is the critical stress that induces martensitic transition and it is linearly distributed in region II, indicating the elastic deformation of martensite. The piecewise

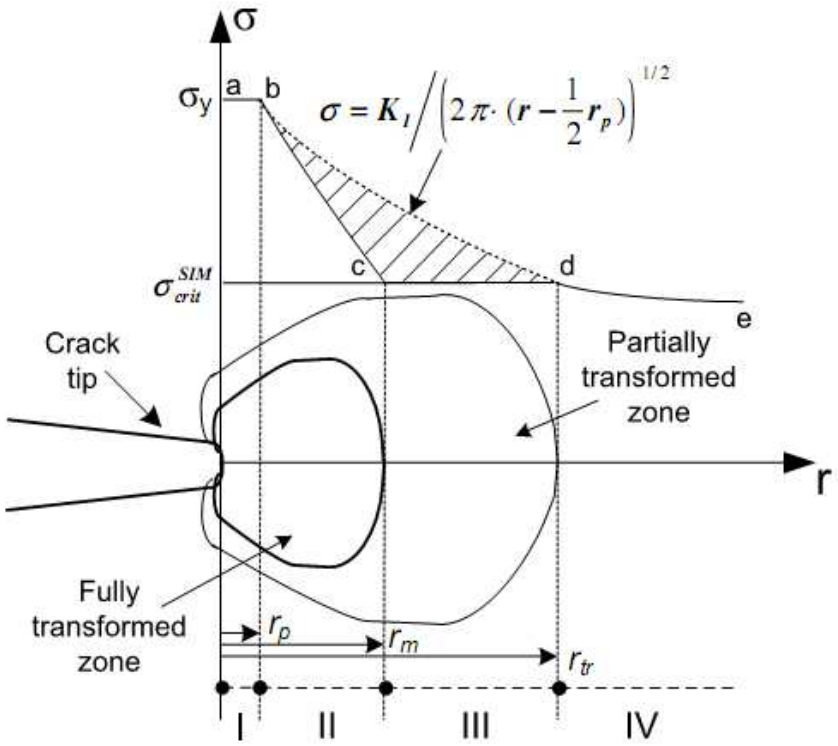

Figure 3.20. Illustration of regions in front of the crack tip in SMAs

stress curve $a-b-c-d-e$ leads to a decrease in load carrying capacity and in order to satisfy the equilibrium condition, stress redistribution is needed to balance the hatched region. It is expected that the plastic zone expands to bear the additional stress. The plastic zone size and the crack tip stress intensity factor are denoted as r_p^* and K_I^* after stress redistribution.

In Figure 3.21, the stress redistribution around the crack tip as a result of SIM transformation is shown. The plastic zone and the full martensite zone lengths increase and after redistribution they are denoted as r_p^* and r_m^*. It is assumed that the stress distribution in region IV is unaffected and r_{tr} does not change. If the second order estimation of Irwin is considered, to keep the force equilibrium, the areas of the shaded regions must be equal and regions A and B should have equal areas. This equilibrium can be formulated as

$$\int_{r_p}^{r_{tr}} (\sigma - \sigma_{crit}^{SIM}) dr = \frac{1}{2}(\sigma_y - \sigma_{crit}^{SIM}) \left\{ \left(r_p^* - r_p\right) + (r_m^* - r_p) \right\} \tag{3.15}$$

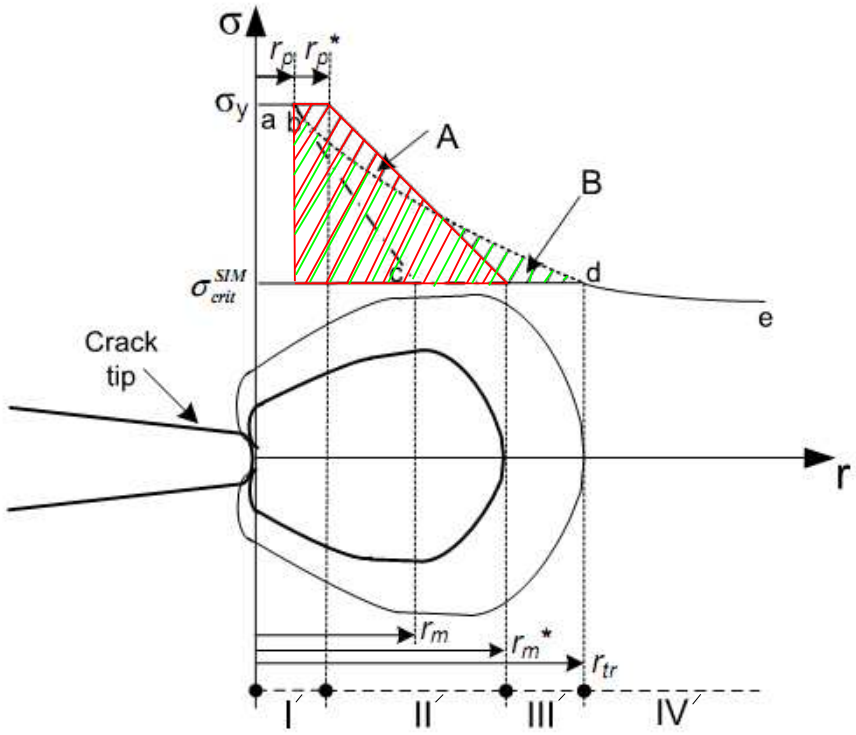

Figure 3.21. Stress redistribution around the crack tip as a result of phase transformation

The martensite fraction zone, r_m, can be expressed from the constitutive relation proposed by Tanaka et al. [35]. The martensite volume fraction, denoted as ξ, is equal to 1 if the material is in fully martensite and is equal to 0.01 if it is in austenitic state. ξ is an exponential function of temperature T and effective stress, σ_{eff}, and it is denoted as

$$\xi = 1.01 - \exp\left\{b_M\left(M_s^0 - T\right) + \frac{b_M}{d_m}\sigma_{eff}\right\} \tag{3.16}$$

where b_M is a material constant and defined as

$$b_M = \frac{\ln 0.01}{(M_s^0 - M_f^0)} \quad . \tag{3.17}$$

M_s^0 and M_f^0 are stress free martensite start and finish temperatures, d_m is the slope of the martensite transformation temperature lines in the stress-temperature plane $\sigma_{crit}^{SIM} = d_m(T - M_s^0)$, σ_{eff} is defined as the von Mises effective stress and is equal to the stress given in 3.14. To have a fully transformed zone ($\xi = 1$), the following

condition should be satisfied:

$$\sigma_{eff} \geq \sigma_{crit}^{SIM} = d_m(T - M_f^0) \quad . \tag{3.18}$$

If we combine Equation 3.18 with Equation 3.14 we get

$$\frac{(K_I)^2}{2\pi.(r_m - \frac{r_p}{2})} = d_m^2(T - M_f^0)^2 \tag{3.19}$$

which yields

$$r_m = \frac{K_I^2}{\left\{2\pi.d_m^2(T - M_f^0)^2\right\}} + \frac{r_p}{2} \tag{3.20}$$

Then Equation 3.13 is replaced into Equation 3.20, and $r_m$is redefined as

$$r_m = \frac{\sigma_0^2}{d_m^2(T - M_f^0)^2}.\frac{1}{2 - (\frac{\sigma_0}{\sigma_Y})^2}a + \frac{1}{2}r_p \tag{3.21}$$

or

$$r_m = \frac{\sigma_0^2}{(\sigma_{crit}^{SIM})^2}.\left(\frac{T - M_s^0}{T - M_f^0}\right)^2.\frac{1}{2 - (\frac{\sigma_0}{\sigma_Y})^2}a + \frac{1}{2}r_p \quad . \tag{3.22}$$

Combining Equation 3.7 and Equation 3.22 gives

$$r_m = \frac{\sigma_0^2}{d_m^2(T - M_f^0)^2}.\frac{1}{2 - (\frac{\sigma_0}{\sigma_Y})^2}a + \frac{1}{2}r_p \quad . \tag{3.23}$$

The stress beyond the transformation zone is defined from Equation 3.14 as

$$\sigma = \frac{K_I}{\left(2\pi.(r - \frac{r_p}{2})\right)^{1/2}} \quad , \tag{3.24}$$

which is also equal to σ_{crit}^{SIM} at the boundary $r = r_{tr}$, which yields

$$\sigma_{crit}^{SIM} = \frac{K_I}{\sqrt{2\pi(r_{tr} - \frac{r_p}{2})}} \quad , \tag{3.25}$$

and

$$r_{tr} = \frac{\left\{\sigma_Y^2 + (\sigma_{crit}^{SIM})^2\right\}.\sigma_0^2}{(2\sigma_Y^2 - \sigma_0^2).(\sigma_{crit}^{SIM})^2} a \quad . \tag{3.26}$$

If $\sigma_0 \leq \sigma_Y$, the following can be written:

$$r_{tr} \approx \frac{1}{2}\left\{\frac{1}{(\sigma_{crit}^{SIM})^2} + \frac{1}{\sigma_Y^2}\right\}.\sigma_0^2.a \quad , \tag{3.27}$$

The size of partial martensite zone (region III) is

$$r_{tr} - r_m = \frac{1}{2}.\frac{\sigma_0^2}{d_m^2}\left\{\frac{1}{(T - M_s^0)^2} - \frac{1}{(T - M_f^0)^2}\right\} a \quad . \tag{3.28}$$

If we go back to Equation 3.15 and assume that the relations $r_p^* = \frac{1}{\pi}\left(\frac{K_I^*}{\sigma_Y}\right)^2$ and $r_m^* = \frac{(K_I^*)^2}{\left\{2\pi.d_m^2(T-M_f^0)^2\right\}} + \frac{r_p^*}{2}$ are still applicable, the crack tip stress intensity factor K_I^*, is;

$$K_I^* = \sqrt{-\frac{2d_M^2(M_f - T)^2\{-a\sigma_0^2\pi((\sigma_{crit}^{SIM})^2 + \sigma_y^2) + 4\sigma_{crit}^{SIM}\sigma_y[K_I^2}{\sigma_{crit}^{SIM}(\sigma_{crit}^{SIM} - \sigma_y)}...} \tag{3.29}$$

$$...\frac{+\sigma_0\sigma_y\sqrt{-\frac{a2\pi\sigma_y^2}{\sigma_0^2 - 2\sigma_y^2}}(\sqrt{a\sigma_0^2\pi(\frac{1}{(\sigma_{crit}^{SIM})^2} + \frac{1}{\sigma_y^2}) - \frac{K_I^2}{\sigma_y^2}} - \sqrt{\frac{K_I^2}{\sigma_y^2}})]\}}{(3d_M^2(M_f - T)^2 + \sigma_y)}}$$

Using material parameters of $Ni_{50}Ti_{50}$ listed in the study of McKelvey and Ritchie [11], applied, transformation and crack tip stress intensity factors for Mode-I loading are calculated and tabulated in Table t:sifssma. The material parameters used are;

$$M_s^0 = -26.9\ ^0\text{C}$$
$$M_f^0 = -54.8\ ^0\text{C}$$
$$d_M = 6.4\ \text{MPa/K}^0$$
$$\sigma_Y = 1300\ \text{MPa}$$
$$\sigma_{crit}^{SIM} = 410\ \text{MPa}$$
$$\sigma_0 = 80\ \text{MPa}$$
$$T = 37\ ^0\text{C}$$

For different a/W ratios, calculated SIFs are shown in Table 3.8.

Table 3.8. Closed form solution for K_I for a $Ni_{50}Ti_{50}$ plate [80]

K_I			
a/W	K_I	K_{tr}	K_I^* $(MPA.mm^{1/2})$
0.20	634.573	17.819	652.392
0.25	709.474	19.923	729.397
0.30	777.190	21.824	799.014
0.35	839.461	23.573	863.034
0.40	897.421	25.201	922.622

Next a center-cracked plate under plane stress with different a/W ratios subjected to tensile stress of 80Mpa is modeled to check the validity of results obtained by using the method of Xiong and Liu [80] and stress intensity factor, K_Is, are calculatted using FE. Since Umat/Nitinol is used to implement the material model, ABAQUS does not calculate and give SIFs directly. Also, because there is a non-homogenous region around the crack tip as a result of phase transformation, J-integrals are contour dependent and

can not be used as they are in the calculation of K_I. SIF, K_I is calculated using $\frac{\Delta U}{\Delta A}$. $G = \frac{K_I^2}{E_{Tip}}$ [88] is used, and $E_{Tip} = E_m = 22$ GPa is taken. The material properties used are listed below [11];

$$E_A = 62 \text{ GPa}$$

$$E_M = 22 \text{ GPa}$$

$$\nu_A = \nu_M = 0.33$$

$$(\frac{\delta\sigma}{\delta T})_L = (\frac{\delta\sigma}{\delta T})_U = 6.4 \text{ MPa/K}^0$$

$$\sigma_L^S = 400 \text{ MPa}$$

$$\sigma_L^E = 410 \text{ MPa}$$

$$\sigma_U^S = 220 \text{ MPa}$$

$$\sigma_U^E = 180 \text{ MPa}$$

$$\varepsilon_V^L = \varepsilon^L = 0.0264$$

$$T_0 = 37^0\text{C}$$

The uniaxial stress-strain diagram of the corresponding material model is plotted in Figure 3.22.

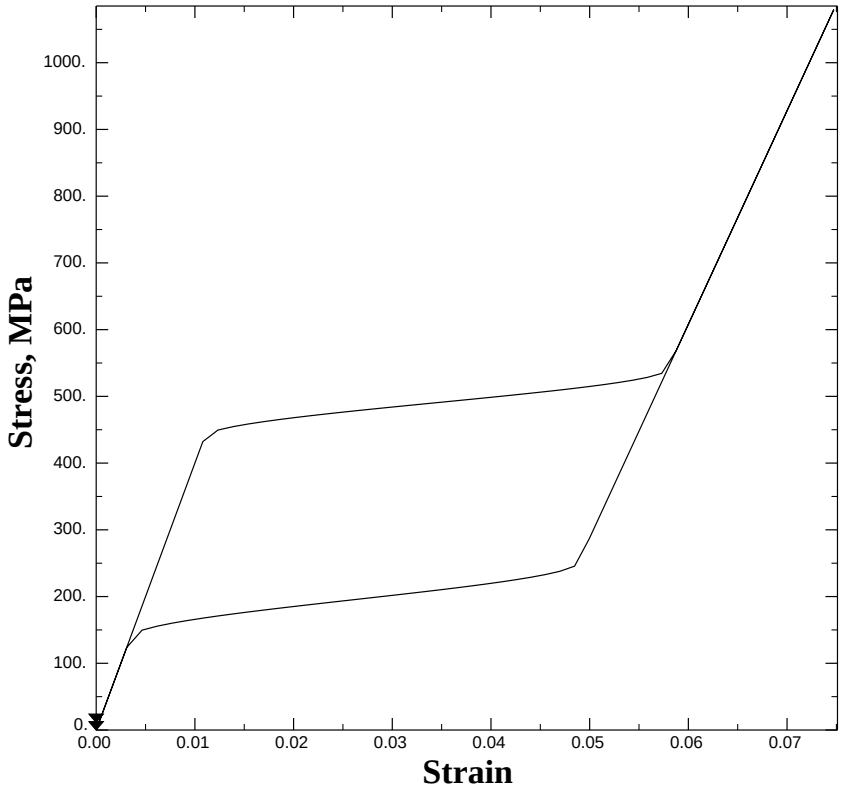

Figure 3.22. The uniaxial tensile stress-strain relationship of the material model

The stress intensity factor, K_I calculated from the energy release rate method is tabulated in Table 3.9. The model is simulated using ABAQUS and the SIF is calculated from $G \approx \frac{\Delta U}{\Delta A} = \frac{K_I^2}{E_{Tip}}$, $E_{Tip} = E_m = 22$ GPa.

Results obtained from the closed-form solution [80] and the FE results are summarized in Table 3.10. factors obtained using $\frac{\Delta U}{\Delta A}$ and the closed-form solutions are similar to each other. Therefore the stress intensity factors in SMAs can be calculated using $\frac{\Delta U}{\Delta A}$. The closed form solution gives both applied and crack tip SIF. Any increase or decrease in crack tip SIF gives an idea on the change in fracture toughness.

Table 3.9. K_I for $Ni_{50}Ti_{50}$ plate using FE

K_I		
a/W	$G \approx \Delta U/\Delta A$	$K_{I(MPA.mm^{1/2})}$
0.20	14.28	560.499
0.25	17.68	623.666
0.30	20.36	669.268
0.35	27.60	779.230
0.40	32.32	843.231

Table 3.10. K_I for $Ni_{50}Ti_{50}$ plate; closed-form solution vs FE solution. ND: Non-dimensionalized form of K_I

The Stress Intensity Factor, K_I in $Ni_{50}Ti_{50}$ specimen					
a/W	Closed-form Sol.(K_{cf})	ND K_{cf}	FEA sol. (K_{FEA})	ND K_{FEA}	difference %
0.20	652.392	1.824	560.450	1.531	16.03
0.25	729.397	1.824	623.666	1.552	14.88
0.30	799.014	1.824	669.268	1.563	14.29
0.35	863.034	1.824	779.230	1.604	12.03
0.40	922.622	1.824	843.231	1.646	9.74

4. FRACTURE TOUGHNESS OF SMAs

Fracture toughness is a material property that describes resistance of a material to fracture. It is a significant parameter because every material has defects and design safety can be provided by utilizing fracture toughness. It is generally denoted by K_{IC}. I stands for Mode-I and C stands for critical, and it has the units of $MPa\sqrt{m}$.

In general, fracture toughness is a fracture criterion for brittle materials and there are two approaches in fracture: energy approach and stress intensity approach. In energy approach the idea is to determine the amount of energy required for propagation of an existing crack. If the energy release rate, G, which is defined as the change of potential energy per unit crack growth area is equal to critical energy release, $G = G_c$, the crack propagates. G can be defined as the driving force and G_C is the material resistance to crack growth. In stress intensity approach, K_I which is Mode-I stress intensity factor (SIF) is the key. If the fracture occurs at a critical value of stress-strain, then there should be a critical value of the SIF called critical stress intensity factor and denoted by K_{IC}; if $K_I = K_{IC}$ fracture occurs. There is a relationship between K_{IC} and G_C in linear elastic fracture mechanics: $G_C = \frac{{K_{IC}}^2}{E'}$ (see Appendix A).

In this study, one of the purpose was to see the effect of phase transformation on fracture toughness of Nitinol. Compared to ordinary materials, Nitinol experiences phase transformation at crack tip because of the high stress region around the tip, and transformation is expected to effect fracture toughness. Although fracture toughness is a material property and can be determined by associated experiments, here a computational approach will be used to discuss toughness.

In literature, there are few efforts to determine effect of phase transformation on fracture and fracture toughness of SMAs. Yi and Gao [76] studied fracture toughening mechanisms in superelastic SMAs due to phase transformation under Mode-I loading. They used the constitutive model of Sun and Hwang [22] and assumed that under

small-scale transformation stress field can be characterized by $\sigma_{ij} = \frac{K^{app}}{\sqrt{2\pi r}}.f_{ij}(\theta)$. It is then stated that since the material near the crack tip is fully transformed, the stress field at the crack tip becomes $\sigma_{ij} = \frac{K^{tip}}{\sqrt{2\pi r}}.f_{ij}(\theta)$. They compared SIFs to interpret the fracture toughness and they stated that **martensite transformation reduces the crack tip stress intensity factor and increases the toughness**. In their study, they did not take volumetric strain into account and they assumed that only shear strain has an effect on toughness.

On the other hand, it is discovered that there is a volume contraction of -0.39% in austenite-to-martensite transformation and volume strain has an important effect on crack tip SIF [11, 91]. In studies of Yan et. al.[78] and Xiong-Liu [80] the volumetric strain is taken into account and they stated that **volume contraction at the crack tip leads to a higher crack tip SIF and toughness reduces**. When the toughness is reduced, material becomes more brittle and crack propagates more easily. Yan et. al. performed analysis for pure volumetric strain and pure shear strain. According to their results, in the case of pure shear strain, toughness increases and if the volumetric strain increases relative to shear strain, fracture toughness decreases.

In the study of Wang [83], finite element analysis isperformed and stress-strain distribution is calculated in front of a notch tip for two materials: Superelastic Nitinol with stress-induced martensite transformation (MT) and fully transformed martensite NiTi without the transformation (NMT). Wang stated that martensite transformation zone in front of a crack or a notch tip in SMAs is similar to plastic zone in normal metals and transformation zone can be characterized by the plastic strain and the yield law in normal metals can be used in examine martensite transformation. As a material model, an elastic-plastic constitutive model is used and material properties are given by digitizing the uniaxial stress-strain curve of the corresponding material. He concluded that martensite transformation increases the load to produce plastic deformation in the transformed martensite at notch tip and decreases maximum normal stress and plastic strain near notch tip. This tends to suspend crack nucleation and propagation at the notch tip in fully transformed martensite and thus increases the fracture load and improves toughness.

In this study, fracture properties of Nitinol are investigated using ABAQUS. A model of 2-D edge cracked SMA plate is prepared and subjected to tensile loading from both ends. Material properties are implemented using a subroutine called UMAT/Nitinol. The subroutine allows the use of some specific parameters given as inputs and there is no direct access to the code and this brings some limitations. The main aim is to interpret the change in fracture toughness of SMA/Nitinol by calculating and observing stress intensity factors and energy release rates.

It is known that SIF is dependent only on the geometry of the plate, the crack length and the applied load, for which some calculations ate tabulated in Table 2.4. This suggests that if a proper SIF calculation is performed for an SMA, the change in the fracture toughness may be clarified. On the other hand, ABAQUS does not calculate stress intensity factor directly for materials defined through UMAT. As a result, an alternative approach is used instead and SIFs are calculated from $\frac{\Delta U}{\Delta A}$s.

In contrast to the study of Wang [83], two edge-cracked plates which are totally austenite at the beginning are considered. Since superelastic Nitinol is fully austenite before phase transformation and a small martensitic region forms around the crack tip upon loading, it is suggested that comparing fully austenite homogenous plate with superelastic SMA one is more accurate. The first plate is a homogenous material that is totally austenite without any phase transformation, with Young's modulus, $E_A = 75$ GPa. The second plate is made of an SMA and subjected to phase transformation from austenite to martensite at a critical stress value. A full martensitic region forms around the crack tip because stresses are extremely high at the tip. The Young's modulus, E_M for martensite is 28 GPa. The geometry of the two plates are exactly the same and they are subjected to the same tensile load. Approximate energy release rates, $\frac{\Delta U}{\Delta A}$, are calculated for different crack lengths in both cases using FE . Results are tabulated in Table 4.1.

Table 4.1. Comparison of energy release rates

$G \approx \Delta U/\Delta A$		
a/W	Homogenous	SMA
0.20	10.25	10.64
0.25	15.35	16.20
0.30	22.62	24.40
0.35	33.18	37.10
0.40	48.81	58.42

Stress intensity factors are determined from approximate energy release rates using $G = \frac{K_I^2}{E}$ for homogenous case and $G \approx \frac{K_I^2}{E_{tip}}$ for SMA case. The results are tabulated in Table 4.2 .

Table 4.2. Comparison of SIFs

Stress Intensity Factor, K_I		
a/W	Homogenous	SMA
0.20	876.698	545.718
0.25	1073.033	673.498
0.30	1302.613	826.559
0.35	1577.498	1019.215
0.40	1913.348	1279.012

In Table 4.1 $\frac{\Delta U}{\Delta A}$s are larger for SMA than the homogenous. For $a/W = 0.20$ there is an increase of 3.8% in $\frac{\Delta U}{\Delta A}$ and the percent increase is getting larger when the crack length increases. On the other hand SIFs are very much smaller in SMA plate than homogenous plate and the percent decrease is decreasing with increasing crack length (See Table 4.3). Since $\frac{\Delta U}{\Delta A}$s are larger in SMA, it is expected that SIFs should be larger as well . Nevertheless Young's modulus of martensite is one third of Young's modulus of austenite and this difference compensates the increase in $G \approx \frac{\Delta U}{\Delta A}$ and reverses the effect. This shows that calculation of K_I has its own shortcomings and brings extra problems to discussion of toughness.

Table 4.3. Percent increase & decrease in $\frac{\Delta U}{\Delta A}$ and K_I

a/W	% increase in $\frac{\Delta U}{\Delta A}$	% decrease in K_I
0.20	3.8	37.8
0.25	5.5	37.2
0.30	7.9	36.5
0.35	11.8	35.4
0.40	19.7	33.2

In energy release rate calculations there are two conditions called fixed-grip and dead-load conditions (See details in Appendix A). In calculations summarized above, dead-load conditions are satisfied by keeping the applied load the same when crack propagates. To examine the behavior of energy release rates of homogenous (austenite) and SMA plate in fixed-grip conditions, new models are constructed. In this new case, displacement boundary conditions are applied at the ends of the plate and kept constant while crack is growing. $\frac{\Delta U}{\Delta A}$ s are calculated for different crack lengths for both cases using FE and results are tabulated in Table 4.4. Stress intensity factors are also calculated and tabulated in Table 4.5.

Table 4.4. Comparison of energy release rates in fixed-grip conditions

$G \approx \Delta U/\Delta A$		
a/W	Homogenous	SMA
0.20	21.48	23.52
0.25	25.12	26.92
0.30	27.92	29.32
0.35	29.88	30.88
0.40	31.12	31.72

As in the case of dead-load conditions $\frac{\Delta U}{\Delta A}$ s are larger and SIFs are smaller in SMA. When percent increases in $\frac{\Delta U}{\Delta A}$ s are compared, in fixed-grip conditions %

Table 4.5. Comparison of SIFs in fixed-grip conditions

Stress Intensity Factor, K_I		
a/W	Homogenous	SMA
0.20	1269.252	811.517
0.25	1372.589	868.194
0.30	1447.066	906.068
0.35	1496.997	929.860
0.40	1527.743	942.422

difference is much smaller than in dead-load conditions and it is decreasing when crack length increases. If we look at the percent decreases in K_I s, they are close to the ones in dead-load condition. Nevertheless the percent decrease is decreasing with increasing crack length in dead-load conditions while it is increasing with increasing crack length in fixed-grip conditions (see Table 4.6).

Table 4.6. Percent increase & decrease in $\frac{\Delta U}{\Delta A}$ and K_I in fixed-grip conditions

a/W	% increase in $\frac{\Delta U}{\Delta A}$	% decrease in K_I
0.20	9.5	36.1
0.25	7.2	36.7
0.30	5.0	37.4
0.35	3.3	37.9
0.40	1.9	38.3

In calculations above, effect of volumetric transformation strain is not taken into account. The parameter ε_V^L determines the amount of volumetric strain which is formed by phase transformation from austenite to martensite. In UMAT/Nitinol, the volumetric transformation strain around the crack tip can be controlled by the user. If it is given equal to transformation strain ε^L, a different algorithm is used by the subroutine and the volumetric transformation is set to zero [86]. This means that there is no effect of volumetric transformation strain on results, only shear strain effects are considered. As discussed in Section 3.5, there is a negative volume change of -0.39% at the crack

tip of a Nitinol plate as a result of phase transformation [78]. In order to see the effects of change in volumetric strain, the volumetric transformation strain is set to -0.0039 and 0.0039 respectively. Corresponding energy release rates and SIFs are tabulated in Table 4.7.

Table 4.7. Effect of volumetric transformation strain

	$\varepsilon_V^{tr} = 0.0039$		$\varepsilon_V^{tr} = 0$		$\varepsilon_V^{tr} = -0.0039$	
a/W	$\frac{\Delta U}{\Delta A}$	K_I	$\frac{\Delta U}{\Delta A}$	K_I	$\frac{\Delta U}{\Delta A}$	K_I
0.20	10.632	545.615	10.636	545.718	10.628	545.513
0.25	16.196	673.415	16.200	673.498	16.208	673.665
0.30	24.400	826.559	24.400	826.559	24.372	826.085
0.35	37.088	1019.051	37.100	1019.215	37.084	1018.996
0.40	58.304	1277.698	58.424	1279.012	58.500	1279.844

Results tabulated in Table 4.7 show that there is a slight difference between values of $\frac{\Delta U}{\Delta A}$. In this material model, effect of a volume contraction by an amount of -0.39% on fracture properties can be ignored. To clarify the effect of volumetric transformation strain, larger volumetric strains are used in the material model. The results are tabulated in Table 4.8.

According to results in Table 4.8, volumetric transformation strain has a little effect on results in SIF. There is a tendency to increase when the volumetric transformation strain is negative and a tendency to decrease if it is positive. But this is not very clear and differences are very small, less than 0.3%. This shows that the effect of volumetric transformation strain in plane stress analysis is very small but it may have a larger influence on plane strain analysis. This should be investigated in future works for an appropriate interpretation.

In ductile materials there is a plastic deformation around crack tip and this makes the crack tip blunt and crack growth is more difficult. As in the case of plastic deformation, phase transformation consumes some internal energy to transformation and this may be considered as a toughening effect if energy is concerned. In both

Table 4.8. Effect of larger volumetric transformation strains

	$\varepsilon_V^{tr} = -0.04$		$\varepsilon_V^{tr} = -0.03$		$\varepsilon_V^{tr} = -0.02$	
a/W	G	K_I	G	K_I	G	K_I
0.20	10.672	546.641	10.648	546.026	10.624	545.410
0.25	16.256	674.661	16.240	674.329	16.220	673.914
0.30	24.560	829.265	24.532	828.792	24.456	827.507
0.35	37.516	1024.914	37.464	1024.203	37.268	1021.520
0.40	58.600	1280.937	58.276	1288.304	58.068	1275.109
	$\varepsilon_V^{tr} = 0$		$\varepsilon_V^{tr} = 0.02$		$\varepsilon_V^{tr} = 0.03$	
a/W	G	K_I	G	K_I	G	K_I
0.20	10.636	545.718	10.640	545.820	10.632	545.615
0.25	16.200	673.498	16.184	673.166	16.176	672.999
0.30	24.400	826.559	24.436	827.169	24.460	827.575
0.35	37.100	1019.215	37.260	1021.411	37.660	1026.879
0.40	58.424	1279.012	58.296	1277.610	58.096	1275.417

dead-load and fixed-grip conditions, $\frac{\Delta U}{\Delta A}$ s are larger in superelastic SMA plate than in fully austenite homogenous plate. Energy release rate, $\frac{\Delta U}{\Delta A}$, which is defined as the required energy to increase the crack extension may be considered as a parameter to interpret the fracture toughness change in SMAs. The energy need to increase the crack extension is larger in SMA and hence, this implies an increase toughness.

On the other hand the crack tip stress intensity factor plays an important role on deciding the effect of phase transformation on fracture toughness. According to few studies, the crack tip SIF increases since there is a volume contraction at the crack tip after transformation and this reduces the toughness. Using the material subroutine UMAT/Nitinol, if results of ABAQUS are considered, an accurate conclusion is impossible because it is shown that volume contraction has a little effect on SIF. SIF calculations using $\frac{\Delta U}{\Delta A}$ bring out extra problems, and is not easy to make a proper conclusion on fracture toughness discussion. To give accurate decisions on fracture toughness change of SMAs, further numerical and experimental investigations should be carried out.

5. CONCLUSIONS

The aim of this work was to study computationally the effect of phase transformation on fracture properties of a Shape Memory Alloy (SMA), Nitinol.

Shape Memory Alloys have two major properties: shape memory effect and superelasticity. In this study, the superelastic property was the major concern. It is known that, if the SMA specimen which is formerly in austenite phase, is subjected to a stress field, a phase transformation from austenite to martensite occurs, called stress induced martensite. The results of this phase transformation and the effect of stress induced martensite on fracture properties were investigated in this study using finite element tools.

A 2-D edge cracked homogenous plate under plane stress conditions was modeled using ABAQUS to verify finite element method and accuracy of the constructed model. J-integrals, energy release rates were calculated for the edge cracked homogenous plates with different a/W ratios. Mode-I stress intensity factors evaluated from J-integral and energy release rate were compared to results available literature data and the validity of the method and the model were proved.

A similar analysis was performed for a 2-D edge cracked SMA plate under plane stress loading. Nitinol was chosen as the material and UMAT/Nitinol subroutine was used to define material properties for ABAQUS. Phase transformation zones around crack tip were investigated for different applied loads and for different a/W ratios. It was observed that a sharp crack results in a severe stress concentration at the crack tip; therefore, phase transformation occurs around the crack tip from the very beginning of loading and the transformation zone becomes larger when the load is increased. When the crack length is increased, the stress values at the crack tip increases and this leads to larger transformation regions around the crack tip.

J-integrals and energy release rates were calculated for edge-cracked Nitinol plate. J-integrals are contour dependent for certain contours, however, they converge to a specific value and become contour independent away from crack tip which due to the existence a non-homogenous zone around the crack tip as a result of phase transformation in non-homogenous materials. Stress intensity factors were calculated using $\frac{\Delta U}{\Delta A}$. It is observed that the constant J-integral values in the fully austenite region, J_∞ are close values of $\frac{\Delta U}{\Delta A}$. Stress intensity factors calculated from J_∞ were compared to ones calculated from the energy release rate, $\frac{\Delta U}{\Delta A}$. Since values are very close, J_∞ can be used to calculate the stress intensity factors in SMAs instead of $\frac{\Delta U}{\Delta A}$.

A parametric study on effect of material properties was carried out and four different cases were constructed. In each case only one material parameter was changed and same analysis was performed. J-integrals, energy release rates and stress intensity factors for different crack lengths are calculated and compared in each case.

Additionally, a closed form solution of Mode-I stress intensity factor developed by Xiong and Liu [80] for a center-cracked 2-D plane stress was used and solutions were compared to the results obtained from ABAQUS. It is observed that stress intensity factors obtained from $\frac{\Delta U}{\Delta A}$ and the closed-form solutions are similar. It was concluded that, stress intensity factors in SMAs can be calculated using $\frac{\Delta U}{\Delta A}$.

Finally the effect of phase transformation on toughness of SMA was investigated. Analyses were repeated for both "dead-load" and "fixed-grip" conditions for an homogenous material which is totally austenite without any phase transformation, and for SMA/Nitinol with phase transformation around crack tip. The elastic modulus of austenite was considered to be equal in both cases. In both dead-load and fixed-grip conditions, $\frac{\Delta U}{\Delta A}$ s are larger in superelastic SMA plate than in fully austenite homogenous plate. Energy release rate, $\frac{\Delta U}{\Delta A}$, which is defined as the required energy to increase the crack extension may be considered as a parameter to interpret the fracture toughness change in SMAs. The energy need to increase the crack extension is larger in SMA and hence, this implies an increase toughness.

As a future work, plane strain analyses may be performed to see the effect of phase transformation on fracture toughness. Volumetric strain may affect directly the phase transformation and indirectly the energy release rates and fracture toughness. Furthermore, a material model should be developed to have full control of material parameters and external conditions, and the fracture behaviors should be evaluated in that perspective.

APPENDIX A: FUNDAMENTAL CONCEPTS OF FRACTURE MECHANICS

Fracture mechanics is concerned with the formation of cracks, mechanics of the cracked bodies, the material's resistance to fracture and the behavior of materials under fracture. Fracture mechanics can be divided into two sub-categories which are linear elastic fracture mechanics (LEFM) and elasto-plastic fracture mechanics (EPFM). LEFM is used to analyze fracture of brittle materials such as high-strength steel, glass, concrete, etc., whereas EPFM is used for ductile materials such as stainless steels, aluminium alloys and polymers in which plasticity always occurs upon fracture.

A.1. Stress at the crack tip

A crack in a solid can be formed in three different modes as illustrated in Figure A.1. These modes are called opening mode (Mode-I), sliding mode (Mode-II) and tearing mode (Mode-III). In Mode-I loading, tensile stress separates the crack faces and opens the crack perpendicular to the plane of crack. In Mode-II and Mode-III loading there are shearing actions, in-plane and out-of-plane shearing, respectively. In "sliding mode", shearing is normal to crack front, whereas in "tearing mode" it is parallel.

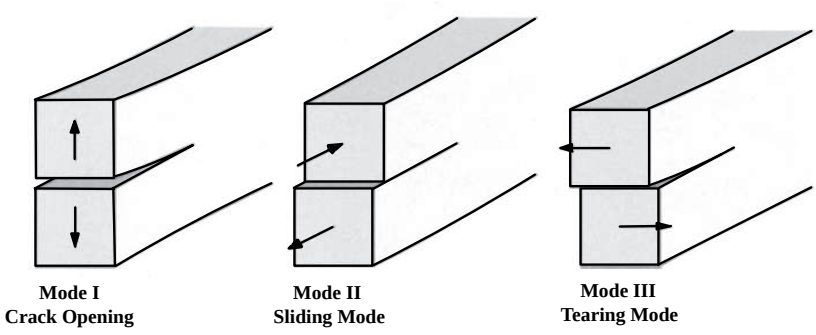

Figure A.1. Modes of fracture

In an isotropic linear elastic material, the stresses in the body can be expressed in closed form. If a polar coordinate axis is defined at the crack tip (Figure A.2), the stress field in a cracked body can be written as

$$\sigma_{ij} = \frac{K}{\sqrt{2\pi r}} f_{ij}(\theta) \tag{A.1}$$

where σ_{ij} are the components of stress tensor, K is the stress intensity factor, θ and r are as defined in Figure A.2. As can be seen from Equation A.1, the stress near the crack tip varies with $\frac{1}{\sqrt{r}}$ and as r $\rightarrow$ 0, stress approaches infinity.

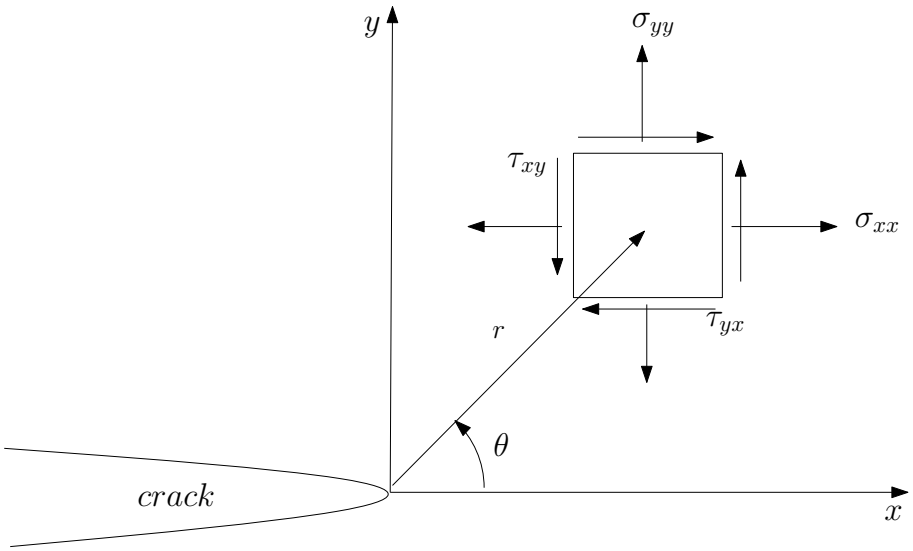

Figure A.2. Illustration of stress field around the crack tip

Stress intensity factor is a parameter which is used in calculation of stress field at the crack tip. It only depends on the geometry of the specimen and the loading conditions. If the stress intensity factor is known, stress-strain and displacement field around the crack tip can be calculated using asymptotic equations. For different loading modes, K's are denoted as K_I, K_{II} and K_{III} and the stress fields are indicated as

$$\lim_{r\to 0} \sigma_{ij}^{(I)} = \frac{K_I}{\sqrt{2\pi r}} f_{ij}^{(I)}(\theta) \tag{A.2}$$

$$\lim_{r\to 0} \sigma_{ij}^{(II)} = \frac{K_{II}}{\sqrt{2\pi r}} f_{ij}^{(II)}(\theta) \tag{A.3}$$

$$\lim_{r\to 0} \sigma_{ij}^{(III)} = \frac{K_{III}}{\sqrt{2\pi r}} f_{ij}^{(III)}(\theta) \tag{A.4}$$

$$\tag{A.5}$$

In a mixed-mode problem the total stress is;

$$\sigma_{ij}^{(total)} = \sigma_{ij}^{(I)} + \sigma_{ij}^{(II)} + \sigma_{ij}^{(III)} \tag{A.6}$$

The complete list of stress and displacement fields for three fracture modes is given in Table A.1

Table A.1. Stress and displacement fields for three fracture modes [94]

	Mode I	Mode II	Mode III
σ_{xx}	$\frac{K_I}{\sqrt{2\pi r}}\cos\frac{\theta}{2}\left[1-\sin\frac{\theta}{2}\sin\frac{3\theta}{2}\right]$	$-\frac{K_{II}}{\sqrt{2\pi r}}\sin\frac{\theta}{2}\left[2+\cos\frac{\theta}{2}\cos\frac{3\theta}{2}\right]$	0
σ_{yy}	$\frac{K_I}{\sqrt{2\pi r}}\cos\frac{\theta}{2}\left[1+\sin\frac{\theta}{2}\sin\frac{3\theta}{2}\right]$	$\frac{K_{II}}{\sqrt{2\pi r}}\sin\frac{\theta}{2}\cos\frac{\theta}{2}\cos\frac{3\theta}{2}$	0
τ_{xy}	$\frac{K_I}{\sqrt{2\pi r}}\cos\frac{\theta}{2}\sin\frac{\theta}{2}\sin\frac{3\theta}{2}$	$\frac{K_{II}}{\sqrt{2\pi r}}\cos\frac{\theta}{2}\left[1-\sin\frac{\theta}{2}\sin\frac{3\theta}{2}\right]$	0
τ_{xz}	$\begin{cases} 0 & \text{plane stress} \\ \upsilon(\sigma_{xx}+\sigma_{yy}) & \text{plane strain} \end{cases}$	$\begin{cases} 0 & \text{plane stress} \\ \upsilon(\sigma_{xx}+\sigma_{yy}) & \text{plane strain} \end{cases}$	0
σ_{zz}	0	0	$-\frac{K_{III}}{\sqrt{2\pi r}}\sin\frac{\theta}{2}$
τ_{yz}	0	0	$\frac{K_{III}}{\sqrt{2\pi r}}\cos\frac{\theta}{2}$
u_x	$\frac{K_I}{2\mu}\sqrt{\frac{r}{2\pi}}\cos\frac{\theta}{2}\left[\kappa-1+2\sin^2\frac{\theta}{2}\right]$	$\frac{K_{II}}{2\mu}\sqrt{\frac{r}{2\pi}}\sin\frac{\theta}{2}\left[\kappa+1+2\cos^2\frac{\theta}{2}\right]$	0
u_y	$\frac{K_I}{2\mu}\sqrt{\frac{r}{2\pi}}\sin\frac{\theta}{2}\left[\kappa-1+2\cos^2\frac{\theta}{2}\right]$	$\frac{K_{II}}{2\mu}\sqrt{\frac{r}{2\pi}}\cos\frac{\theta}{2}\left[\kappa-1-2\sin^2\frac{\theta}{2}\right]$	0
u_z	$\begin{cases} -\frac{\upsilon z}{E}(\sigma_{xx}+\sigma_{yy}) & \text{plane stress} \\ 0 & \text{plane strain} \end{cases}$	$\begin{cases} -\frac{\upsilon z}{E}(\sigma_{xx}+\sigma_{yy}) & \text{plane stress} \\ 0 & \text{plane strain} \end{cases}$	$\frac{K_{III}}{\mu}\sqrt{\frac{r}{2\pi}}\sin\frac{\theta}{2}$

μ is the shear modulus, $\kappa = 3-4\nu$ for plane strain, $\kappa = (3-\nu)/(1+\nu)$ for plane stress

A.2. Griffith Criterion and Energy Release Rate

In 1921, Griffith [95, 96] proposed a thermodynamic, energy based criterion for fracture by considering the total change in energy of a cracked body as crack size increases. This criterion suggests that there is an energy transfer from external work and/or strain energy to surface energy when crack propagates [92]. According to law of conservation of energy, the energy balance can be written as;

$$\dot{W} = \dot{E} + \dot{K} + \dot{\Gamma} \tag{A.7}$$

where $\dot{W}$ is the external work per unit time, $\dot{E}$ is the rate of change of total internal energy and $\dot{K}$ is the rate of change of kinetic energy. $\dot{\Gamma}$ is the surface energy per unit time. The internal energy can be written in two part;

$$E = U^e + U^p \tag{A.8}$$

where U^e is elastic strain energy and U^p is plastic strain energy.

If loads are applied quasi statically and the crack grows slowly K is negligible. All changes are caused by changes in crack size and time derivative can be written as;

$$\frac{\partial}{\partial t} = \frac{\partial A}{\partial t}\frac{\partial}{\partial A} \tag{A.9}$$

and Equation A.7 becomes

$$\frac{\partial W}{\partial A} = (\frac{\partial U^e}{\partial A} + \frac{\partial U^p}{\partial A}) + \frac{\partial \Gamma}{\partial A} \quad . \tag{A.10}$$

Equation A.10 shows that, during crack propagation the rate of external works is equal to the rate of elastic plus plastic strain energy and the energy dissipated. It can be rewritten as

$$-\frac{\partial \Pi}{\partial A} = \frac{\partial U^p}{\partial A} + \frac{\partial \Gamma}{\partial A} \tag{A.11}$$

and

$$\Pi = U^e - W \tag{A.12}$$

This shows that the rate of the potential energy decrease during crack propagation is equal to the sum of the rates of energy dissipation in plastic deformation and crack

growth.

According to Griffith theory, for ideally brittle materials the energy dissipation in plastic deformation is negligible and Equation A.10 becomes

$$G = -\frac{\partial \Pi}{\partial A} = \frac{\partial W}{\partial A} - \frac{\partial U^e}{\partial A} = \frac{\partial \Gamma}{\partial A} \tag{A.13}$$

The left-hand side of the the equation is defined as the energy available for crack growth or the crack driving force and the right-hand side is the resistance of the material to crack growth [92].

There are two cases in practice which are "fixed-grip" and "dead-load". In fixed-grip conditions, it is considered that the system is isolated and there is no external work. The Equation A.13 becomes

$$G = -\frac{\partial U^e}{\partial A} \tag{A.14}$$

An increase in crack length results in a decrease in stored elastic strain energy, ΔU^e. In dead-load conditions the applied loads on the surface are kept constant during crack growth. According to Clapeyron's theorem the work performed by the external loads is twice the increase of elastic strain energy [97]. This gives

$$\frac{\partial W}{\partial A} = 2\frac{\partial U^e}{\partial A} \tag{A.15}$$

and

$$G = \frac{\partial U^e}{\partial A} \tag{A.16}$$

In dead-load conditions the required energy for crack propagation is supplied from external work. The half of the external work is released during crack growth and the other half is stored as the elastic strain energy. This means that internal strain energy

increases during crack growth.

From the stress analysis of a through crack in an infinitely wide plate with unit thickness under Mode-I loading proposed by Griffith [95]

$$G = \frac{dU}{t.da} = \frac{K_I^2}{E'} = \frac{\pi\sigma^2 a}{E'} \tag{A.17}$$

where t is thickness, da is the change in crack length, K_I^2 is Mode-I stress intensity factor, a is the initial crack length and E' is effective Young's modulus and is equal to

$$E' = \begin{cases} E \quad \text{if} \quad \text{plane} \quad \text{stress} \\ E/\left(1-\nu^2\right) \quad \text{if} \quad \text{plane} \quad \text{strain} \end{cases} \tag{A.18}$$

A.3. The J Contour Integral

In linear elastic materials, it is assumed that there is no crack tip plasticity and by means of the energy release rate, G, the elastic stress field can be determined. In the case of crack tip plasticity, instead of G, the J-integral is used to calculate the nonlinear strain energy release rate. It is developed by Rice [98] and it can be written as a path-independent line integral. It is used to establish the crack tip stresses and strains in materials with nonlinear behaviors. J integral is calculated at an arbitrary

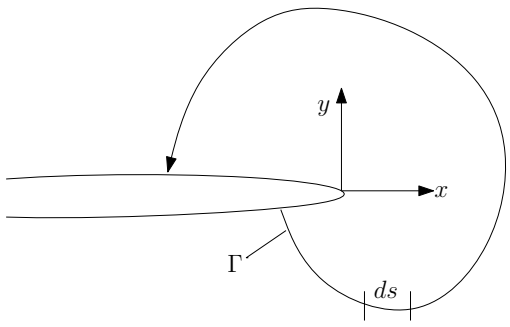

Figure A.3. Arbitrary contour around the crack tip

counter-clockwise path, Γ, around the crack tip (see Figure A.3) and is stated as

$$J = \int_{\Gamma} w dy - \int_{\Gamma} T_i \frac{\partial u_i}{\partial x} ds \tag{A.19}$$

where w is the strain energy density, T_i are components of the traction vector, u_i are the displacement vector components and ds is a length increment along the contour Γ. The strain energy density is defined as

$$w = \int_{0}^{\varepsilon_{ij}} \sigma_{ij} d\varepsilon_{ij} \tag{A.20}$$

where σ_{ij} and ϵ_{ij} are the stress and strain tensors respectively. T_i are the normal stresses acting on the boundaries. Components of the traction vector are

$$T_i = \sigma_{ij} n_j \tag{A.21}$$

where n_j are the components of the unit vector to path Γ. For a linear elastic homogenous material, J-integral is contour independent and stress intensity factor, K can be calculated using the J-integral. Also $J = G$ in which G is the energy release rate and equals to Equation A.17.

REFERENCES

1. Greninger, A. B. and V. G. Mooradian, "Strain Transformation in Metastable Copper-Zinc and Beta Copper-Tin Alloys", *Transactions AIME*, Vol. 128, pp. 337-341, 1938.

2. Buehler, W. J., J. V. Gilfrich and R. C. Wiley, "Effects of Low-Temperature Phase Changes on the Mechanical Properties of Alloys Near Composition TiNi", *Journal of Applied Physics*, Vol. 34, pp. 1475, 1963.

3. Buehler, W. J. and F. E. Wang, "Nickel-Base Alloys", *U.S. Patent*, 3,174,851, 1965.

4. Birman, V., "Review of Mechanics of Shape Memory Alloy Structures", *Applied Mechanics Reviews*, Vol. 50, No. 11, Part 1, 1997.

5. Mantovani, D., "Shape Memory Alloys: Properties and Biomedical Applicaitons", *Smart Materials*, October 2002.

6. Duerig, T. W., "Applications of Shape Memory Alloys", *Materials Science Forum*, Vol. 56-58, pp. 679-692, 1990.

7. Auricchio, F., "Shape Memory Alloys: Applications, Micromechanics, Macromodeling And Numerical Simulations", Ph.D. Thesis, University of California at Berkeley, 1995.

8. Lagoudas, D. C. (Editor), "Shape Memory Alloys: Modelling and Engineering Approches", Springer Science+Business Media, LLC, New York, 2008.

9. Duerig, T. W., K. N. Melton, D. Stockel, and C. M. Wayman, "Engineering Aspects of Shape Memory Alloys", Butterworth-Heinemann Ltd., London, 1990.

10. Smart Lab, Texas A&M, *Definition of a Shape Memory Alloy*, http://smart.tamu.

edu/overview/smaintro/simple/definition.html, 2009.

11. McKelvey, A. L. and R. O. Ritchie, "Fatigue-Crack Growth Behavior in the Superelastic and Shape-Memory Alloy Nitinol", *Metallurgical and Materials Transcation A*, Vol. 32, pp. 731, 2001.

12. Mook, K. S., "Shape Memory Alloys: Stress-Induced Phase Transformation, Constitutive Model and Nonlinear Finite Element Formulation" Ph.D. Thesis, University of Florida, 2003.

13. Strelec, J. K., D. C. Lagoudas, M. A. Khan, and J. Yen, "Design and Implementation of a Shape Memory Alloy Actuated Reconfigurable Wing", *Journal of Intelligent Material Systems and Structures*, Vol. 14, pp. 257-273, 2003.

14. Godard, O., M. Lagoudas and D. Lagoudas, "Design of Space Systems Using Shape Memory Alloys", *Proceedings of SPIE, Smart Structures and Materials*, San Diego, CA, Vol. 5056, pp. 545-558, 2003.

15. Delaey, L., R. V. Krishnan, H. Tas and H. Warlimont, "Thermoelasticity, Pseudoelasticity and the Memory Effects Associated with Martensitic Transformations-Part1", *Journal of Materials Science*, Vol. 9, No. 9, pp. 1521-1535, 1974.

16. Krishnan, R. V., L. Delaey, H. Tas and H. Warlimont, "Thermoelasticity, Pseudoelasticity and the Memory Effects Associated with Martensitic Transformations-Part2", *Journal of Materials Science*, Vol. 9, No. 9, pp. 1536-1544, 1974.

17. Warlimont, H., L. Delaey, R. V. Krishnan and H. Tas, "Thermoelasticity, Pseudoelasticity and the Memory Effects Associated with Martensitic Transformations-Part3", *Journal of Materials Science*, Vol. 9, No. 9, pp. 1545-1555, 1974.

18. Achenbach, M. and I. A. Müller, "A model for Shape Memory", *Journal de Physique*, Vol. 12, No. 43, pp. 163-167, 1982.

19. Fischer, F. D. and K. Tanaka, "A micromechanical model for the Kinetics of Martensitic Transformation", *International Journal of Solids and Structures*, Vol. 29, No. 14-15, pp. 1723-1728, 1992.

20. Patoor, E., A. Eberhardt and M. Berveiller, "Micromechanical Modelling of Superelasticity in Shape Memory Alloys", *Pitman Research Notes in Mathematics*, Vol. 296, pp. 38-54, 1993.

21. Patoor, E., A. Eberhardt and M. Berveiller, "Micromechanical Modelling of the Shape Memory Behavior", *In Mechanics of Phase Transformations and Shape Memory Alloys*, ASME, pp. 23-37, 1994.

22. Sun, Q. P. and K. C. Hwang, "Micromechanics Modeling for the Constitutive Behavior of Polycrystalline Shape Memory Alloys-Part I: Derivation of General Relations", *Journal of the Mechanics and Physics of Solids*, Vol. 41, No. 1, pp. 1-17, 1993.

23. Sun, Q. P. and K. C. Hwang, "Micromechanics Modeling for the Constitutive Behavior of Polycrystalline Shape Memory Alloys-Part II: Study of Individual Phenomenon", *Journal of the Mechanics and Physics of Solids*, Vol. 41, No. 1, pp. 19-33, 1993b.

24. Marketz, F. and F. D. Fischer, "Micromechanical Modelling of Stress-Assisted Martensitic Transformation", *Modelling and Simulation in Materials Science and Engineering*, Vol. 2, pp. 1017-1046, 1994.

25. Comstock Jr., R. J., T. E. Buchheit, M. Somerday and J. A. Wert, "Modeling the Transformation Stress of Constrained Shape Memory Alloys Single Crystals", *ACTA Materialia*, Vol. 44, No. 9, pp. 3505-3514, 1996.

26. Levitas, V. I., A. V. Idesman, E. Stein, J. Spielfeld and E. Hornbogen, "A Simple Micromechanical Model for Pseudoelastic Behavior of CuZnAl Alloy", *Journal of Intelligent Material Systems and Structures*, No. 5, pp. 324-334, 1998.

27. Lu, Z. K. and G. J. Weng, "A Self-Consistent Model for the Stress-Strain Behavior of Shape-Memory Alloy Polycrystals", *ACTA Materialia*, Vol. 46, No. 15, pp. 5423-5433, 1998.

28. Siredey, N., E. Patoor, M. Berveiller and A. Eberhardt, "Constitutive Equations for Polycrystalline Thermoelastic Shape Memory Alloys. Part I: Intragranular Interactions and Behavior of the Grain", *International Journal of Solids and Structures*, Vol. 36, pp. 4289-4315, 1999.

29. Gall, K., H. Sehitoglu, R. Anderson, I. Karaman, Y. I. Chumlyakov, and I. V. Kireeva, "On the Mechanical Behavior of Single Crystal Ni-Ti Shape Memory Alloys and Related Polycrystalline Phenomenon", *Materials Science and Engineering A*, Vol. 317, pp. 85-92, 2001.

30. Muller I., and S. Seelecke, "Thermodynamic Aspects of Shape Memory Alloys, Mathematical and Computer Modelling", Vol. 34, No. 12-13, pp. 1307-1355, 2001.

31. Jung, Y., P. Papadopoulos and R. O. Ritchie, "Constitutive Modelling and Numerical Simulation of Multivariant Phase Transformation in Superelastic Shape-Memory Alloys", *International Journal of Numerical Methods and Engineering*, Vol. 60, pp. 429-460, 2004.

32. Stupkiewicz, S. and H. Petryk, "Finite-Strain Micromechanical Model of Stress-Induced Martensitic Transformations in Shape Memory Alloys", *Materials Science and Engineering A*, Vol. 438-440, pp. 126-130, 2006.

33. Peng, X., W. Pi and J. Fan, "A Microstructure-Based Constitutive Model for the Pseudoelastic Behavior of NiTi SMAs", *International Journal of Plasticity*, Vol. 24, pp. 966-990, 2008.

34. Wang, X., B. Xu, Z. Yue and X. Tong, "Fracture Behavior of the Compact Tension Specimens in NiTi Shape Memory Alloys", *Materials Science and Engineering A*, Vol. 485, pp. 14-19, 2008.

35. Tanaka, K., "A Thermomechanical Sketch of Shape Memory Effect: One-Dimensional Tensile Behavior", *Materials Science Research International*, Vol. 18, pp. 251, 1985.

36. Tanaka, K. and R. Iwasaki, "A Phenomenological Theory of Transformation Superplasticity", *Engineering Fracture Mechanics*, Vol. 21, pp. 709-720, 1985.

37. Tanaka, K., S. Kobayashi and Y. Sato, "Thermomechanics of Transformation Pseudoelasticity and Shape Memory Effect in Alloys", *International Journal of Plasticity*, Vol. 2, pp. 59-72, 1986.

38. Tanaka, K. and S. Nagaki, "Thermomechanical Description of Materials with Internal Variables in the Process of Phase Transitions", *Ingenieur-Archive*, Vol. 51, pp. 287-299, 1982.

39. Tanaka, K., F. Nishimura and H. Tobushi, "Phenomenological Analysis on Subloops in Shape Memory Alloys due to Incomplete Transformations", *Journal of Intelligent Material Systems and Structures*, Vol. 5, pp. 387-493, 1994.

40. Liang, C. and C. A. Rogers, "One-Dimensional Thermomechanical Constitutive Relations for Shape Memory Materials", *Journal of Intelligent Material Systems and Structures*, No. 1, pp. 207-234, 1990.

41. Liang, C. and C. A. Rogers, "A Multi-Dimensional Constitutive Model for Shape Memory Alloys", *Journal of Engineering Mathematics*, Vol. 26, pp. 429-443, 1992.

42. Brinson, L. C., "One Dimensional Constitutive Behavior of Shape Memory Alloys: Thermomechanical Derivation with Non-Constant Material Functions and Redefined Martensite Internal Variable", *Journal of Intelligent Material Systems*

and Structures, No. 4, p. 229-242, 1993.

43. Ivshin, Y. and T. J. Pence, "A Constitutive Model for Hysteretic Phase Transition Behavior", *International Journal of Engineering Science*, Vol. 32, No. 4, pp. 681-704, 1994.

44. Ivshin, Y. and T. J. Pence, "A Thermomechanical Model for a One Variant Shape Memory Material", *Journal of Intelligent Material Systems and Structures*, No. 5, pp. 455-473, 1994b.

45. Boyd, J. G. and D. C. Lagoudas, "A Thermodynamical Constitutive Model for the Shape Memory Effect due to Transformation and Reorientation", *Proceedings of the International Society for Optical Engineering*, Vol. 2189, pp. 276-288, 1994.

46. Boyd, J. G. and D. C. Lagoudas, "A Thermodynamic Constitutive Model for the Shape Memory Materials. Part I: The Monolithic Shape Memory Alloys", *International Journal of Plasticity*, Vol. 12, No. 6, pp. 805-842, 1996.

47. Kasper, E. P., "Shape Memory Materials: Constitutive Modeling and Finite Element Analysis", Ph.D. Thesis, University of California at Berkeley, 1997.

48. Qidwai, M. A. and D. C. Lagoudas, "Numerical implementation of a Shape Memory Alloy Thermomechanical Constitutive Model Using Return Mapping Algorithms", *International Journal for Numerical Methods in Engineering*, Vol. 47, pp. 1123-1168, 2000.

49. Zhu, J., N. Liang, W. Huang, K. M. Liew and Z. Liu, "A Thermodynamic Constitutive Model for Stress Induced Phase Transformation in Shape Memory Alloys", *International Journal of Solids and Structures*, Vol. 39, pp. 741-763, 2002.

50. Janetti, C. V., "Martensitic Phase Transformations in Shape Memory Alloys: Constitutive Modelling and Numerical Simulations", PHD. Thesis, University of Pennsylvania, 2005.

51. Reese S. and D. Christ, "Finite Deformation Pseudoelasticity of Shape Memory Alloys-Constitutive Modelling and Finite Element Implementation", *International Journal of Plasticity*, Vol. 24, pp. 455-482, 2008.

52. Bertram, A., "Thermo-mechanical Constitutive Equations for the Description of Shape Memory Effects in Alloys", *Nuclear Engineering and Design*, Vol. 74, pp. 173-182, 1982.

53. Lazghab, T., "Modelling of Shape Memory Alloys with Plasticity", Ph.D. Thesis, Florida International University, 2001.

54. Panoskaltsis, V. P., S. Bahuguna and D. Soldatos, "On the Thermomechanical Modeling of Shape Memory Alloys", *International Journal of Non-Linear Mechanics*, Vol. 39, pp. 709-722, 2004.

55. Auricchio, F., "Three-dimensional Modeling of Shape-Memory Materials", *Journal de Physique IV*, Vol. 11, pp. 577-582, 2001.

56. Auricchio, F. and J. Lubliner, "A Uniaxial Model for Shape-Memory Alloys", *International Journal of Solids and Structures*, Vol. 34, pp. 3601-3618, 1997.

57. Auricchio, F., S. Marfia and E. Sacco, "Modeling of SMA materials: Training and Two Way Shape Memory Effects", *Computers & Structures*, Vol. 81, pp. 2301-2317, 2003.

58. Auricchio, F. and E. Sacco, "A One-Dimensional Model for Superelastic Shape-Memory Alloys with Different Elastic Properties Between Austenite and Martensite", *International Journal of Nonlinear Mechanics*, Vol. 32, pp. 1101-1114, 1997.

59. Auricchio, F. and E. Sacco, "A Superelastic Shape-Memory-Alloy Beam Model", *Journal of Intelligent Materials and Structures*, Vol. 8, pp. 489-501, 1997.

60. Auricchio, F. and E. Sacco, "A Temperature-Dependent Beam for Shape-Memory Alloys: Constitutive Modeling, Finite-Element Implementation and Numerical

Simulations", *Computer Methods in Applied Mechanics and Engineering*, Vol. 174, pp. 171-190, 1999.

61. Auricchio, F., R. L. Taylor and J. Lubliner, "Shape-Memory Alloys: Macromodeling and Numerical Simulations of the Superelastic Behavior", *Computer Methods in Applied Mechanics and Engineering*, Vol. 146, pp. 281-312, 1997.

62. Auricchio, F. and R. L. Taylor, "Shape-Memory Alloys: Modeling and Numerical Simulations of the Finite-Strain Superelastic Behavior", *Computer Methods in Applied Mechanics and Engineering*, Vol. 143, pp. 175-194, 1997.

63. Lubliner, J. and F. Auricchio, "Generalized Plasticity and Shape-Memory Alloys", *International Journal of Solids and Structures*, Vol. 33, pp. 991-1003, 1996.

64. Masud, A., M. Panahandeh and F. Auricchio, "A Finite-Strain Finite Element Model for the Pseudoelastic Bahvior of Shape Memory Alloys", *Computer Methods in Applied Mechanics and Engineering*, Vol. 148, pp. 23-37, 1997.

65. McKelvey, A. L. and R. O. Ritchie, "Fatigue-Crack Propagation in Nitinol, a Shape-Memory and Superelastic Endovascular Stent Material", *Journal of Biomedical Materials Research Part A*, Vol. 47, No. 3, pp. 301-308, 1999.

66. McNaney, M., V. Imbeni, Y. Jung, P. Papadopoulos and R. O. Ritchie, "An Experimental Study of the Superelastic EffEct in a Shape-Memory Nitinol Alloy Under Biaxial Loading", *Mechanics of Materials*, Vol. 35, pp. 969-986, 2003.

67. Chen, J. H., W. Sun, and G. Z. Wang, "Investigation on the Fracture Behavior of Shape Memory Alloy NiTi", *Metallurgical and Materials Transactions A*, Vol. 36A, pp. 941, 2005.

68. Robertson, S. W., A. Mehta, A. R. Pelton and R. O. Ritchie, "Evolution of Crack-Tip Transformation Zones in Superelastic Nitinol Subjected to in Situ Fatigue: A Fracture Mechanics and Synchrotron X-Ray Microdiffraction Analysis", *Acta*

Materialia, Vol. 55, pp. 6198-6207, 2007.

69. Daly, S., A. Miller, G. Ravichandran and K. Bhattacharya, "An Experimental Investigation of Crack Initiation in Thin Sheets of Nitinol", *Acta Materialia*, Vol. 55, pp. 6322-6330, 2007.

70. Gollerthan, S., D. Herberg, A. Baruj and G. Eggeler, "Compact Tension Testing of Martensitic/Pseudoplastic NiTi Shape Memory Alloys", *Materials Science and Engineering A*, Vol. 481-482, pp. 156-159, 2008.

71. Gollerthan, S., M. L. Young, A. Baruj, J. Frenzel, W. W. Schmahl and G. Eggeler, "Fracture Mechanics and Microstructure in NiTi Shape Memory Alloys", *Acta Materialia*, Vol. 57, pp. 1015-1025, 2009.

72. Wang, X. M., Z. Z. Lu and Z. F. Yue, "The Effect of Notches on the Fracture Behavior in NiTi Shape Memory Alloys", *International Journal of Solids and Structures*, Vol. 46, pp. 557-571, 2009.

73. Birman, V., "On mode-I Fracture of Shape Memory Alloy Plates", *Smart Materials and Structures*, Vol. 7, pp. 433-437, 1998.

74. Stam, G. and E. Giessen, "Effect of Reversible Phase Transformations on Crack Growth", *Mechanics of Materials*, Vol. 21, pp. 51-71, 1995.

75. Sun, Q. P., K. C. Hwang and S. U. Yu, "A Micromechanics Constitutive Model of Transformation Plasticity with Shear and Dilatation Effect", *Journal of the Mechanics and Physics of Solids*, Vol. 39, No. 4, pp. 507-524, 1991.

76. Yi, S. and S. Gao, "Fracture Toughening Mechanism of Shape Memory Alloys due to Martensite Transformation", *International Journal of Solids and Structures*, Vol. 37, pp. 5315-5327, 2000.

77. Yi, S., S. Gao and L. Shen, "Fracture Toughening Mechanism of Shape Memory Alloys Under Mixed Mode Loading due to Martensite Transformation", *Interna-*

tional Journal of Solids and Structure, Vol. 38, pp. 4463-4476, 2001.

78. Yan, W., C. H. Wang, X. P. Zhang and Y. W. Mai, "Effect of Transformation Volume Contraction on the Toughness of Superelastic Shape Memory Alloys", *Smart Materials and Structures*, Vol. 11, pp. 947-955, 2002.

79. Yan, W., C. H. Wang, X. P. Zhang and Y. W. Mai, "Theoretical Modelling of the Effect of Plasticity on Reverse Transformation in Superelastic Shape Memory Alloys", *Materials Science and Engineering A*, Vol. 354, pp. 146-157, 2003.

80. Xiong, F., Y. Liu and E. Pagounis, "Fracture Mechanism of a Ni-Mn-Ga Ferromagnetic Shape Memory Alloy Single Crystal", *Journal of Magnetism and Magnetic Materials*, Vol. 285, pp. 410-416, 2005.

81. Freed, Y. and L. Banks-Sills, "Crack Growth Resistance of Shape Memory Alloys by Means of a Cohesive Zone Model", *Journal of the Mechanics and Physics of Solids*, Vol. 55, pp. 2157-2180, 2007.

82. Wang, G. Z., "A Finite Element Analysis of Evolution of Stress-Strain and Martensite Transformation in front of a Notch in Shape Memory Alloy NiTi", *Material Science and Engineering A*, Vol. 460-461, pp. 383-391, 2007.

83. Wang, G. Z., "Effect of Martensite Transformation on Fracture Behavior of Shape Memory Alloy NiTi in a Notched Specimen", *International Journal of Fracture*, Vol. 146, No. 1-2, pp. 93-104, 2007.

84. ABAQUS, "ABAQUS Theory Manual", Version 6.7, ABAQUS Inc., 2007.

85. Anderson T. L., *Fracture Mechanics: Fundamentals and Applications*, CRC Press, Boca Raton, Florida, 1991.

86. ABAQUS, "UMAT and VUMAT routines for the simulation of Nitinol", Answer ID# 1658, ABAQUS Inc., Pawtucket, RI, 2008.

87. Daly, S. H., "Deformation and Fracture of Thin Sheets of Nitinol", Ph.D. Thesis, California Institute of Technology, 2007.

88. Jina, Z. H. and R. C. Batraa, "Some basic Fracture Mechanics Concepts in Functionally Graded Materials", *Journal of the Mechanics and Physics of Solids*, Vol. 44, No. 8, pp. 1221-1235, 1996.

89. Jackson, C. M., H. J. Wagner and R. J. Wasilewski, "The Alloy with a Memory, 55-Nitinol: Its Physical Metallurgy, Properties, and Applications", *NASA Report*, SP-5110, 1972.

90. Jacobus, K., H. Sehitoglu and M. Balzer, "Effect of Stress State on the Stress-Induced Martensitic Transformation in Polycrystalline Ni-Ti Alloy", *Metallurgical And Materials Transactions A*, Vol. 27, pp. 3066-3073, 1996.

91. Holtz, R. L., K. Sadananda and M. A. Imam, "Fatigue Thresholds of Ni-Ti Alloy Near the Shape Memory Transition Temperature", *International Journal of Fatigue*, Vol. 21, pp. 137-145, 1999.

92. Gdoutos, E. E., "Fracture Mechanics: An Introduction, Solid Mechanics and Its Applications", Kluwer Academic Publishers, 1948.

93. Irwin, G. R., "Fracture, Handbuch der Physik", Vol. 6, pp. 551-590, Springer, Berlin, 1958.

94. Wang, C. H., "Introduction to fracture mechanics", Melbourne, Vic. : DSTO Aeronautical and Maritime Research Laboratory, 1996.

95. Griffith, A. A., "The Phenomena of Rupture and Flow in Solids", *Philosophical Transactions of the Royal Society of London A*, Vol. 221, pp. 163-198, 1921.

96. Griffith, A. A., "The Theory of Rupture", *Proceedings of First International Congress of Applied Machanics, Delft*, pp. 55-63, 1924.

97. Bueckner, H. F. and N. Y. Schenectady, "The Propagation of Cracks and the Energy of Elastic Deformation", *Transaction of the ASME*, Vol. 80, pp. 1225-1229, 1958.

98. Rice, J. R., "A Path Independent Integral and the Approximate Analysis of Strain Concentration by Notches and Cracks", *Journal of Applied Mechanics*, Vol. 35, pp. 379-386, 1968.